Atmospheric Correction Models for Retrievals of Calibrated Spectral Profiles from Hyperion EO-1 Data

Prashant Kawishwar

January, 2007

Atmospheric Correction Models for Retrievals of Calibrated Spectral Profiles from Hyperion EO-1 Data

by

Prashant Kawishwar

Thesis submitted to the International Institute for Geo-information Science and Earth Observation in partial fulfilment of the requirements for the degree of Master of Science in Geo-information Science and Earth Observation, Specialisation: (Geoinformatics)

Thesis Assessment Board

Chairman	:	Prof. Dr. Ir. A. (Alfred) Stein, ITC.
External Examiner	:	Dr. P. K. Garg, IIT Roorkee.
IIRS Member	:	Mr. P. L. N. Raju
IIRS Member	:	Mr. C. Jeganathan
IIRS Supervisor	:	Dr. Milap Punia

Thesis Supervisor

IIRS	:	Dr. Milap Punia
ITC	:	Dr. Norman Kerle
		Dr. H. M. A (Harald) van der Werff

INTERNATIONAL INSTITUTE FOR GEO-INFORMATION SCIENCE AND EARTH OBSERVATION
ENSCHEDE, THE NETHERLANDS
AND
INDIAN INSTITUTE OF REMOTE SENSING, NATIONAL REMOTE SENSING AGENCY (NRSA),
DEPARTMENT OF SPACE, GOVERNMENT OF INDIA, DEHRA DUN, INDIA

Disclaimer

This document describes work undertaken as part of a programme of study at the International Institute for Geo-information Science and Earth Observation. All views and opinions expressed therein remain the sole responsibility of the author, and do not necessarily represent those of the institute.

Abstract

The need for reliable spectral information possesses both challenges and opportunities for Hyperspectral remote sensing in mapping, monitoring and exploration of earth's natural resources. The Atmosphere contributes significantly to the at-sensor radiance as Hyperspectral scanners have very narrow spectral resolution. One of the requirements for extracting calibrated spectra from Hyperion EO-1 is to first compensate for atmospheric effects using the existing atmospheric correction models. The objectives of the present study was to derive apparent reflectance from radiative transfer models for Hyperion data sets and analyze absorptions along the contiguous spectra to enable effective pre-processing. The study also intended to evaluate the comparative utility of atmospheric correction models and to attempt band positioning absorption analysis and evaluate its effectiveness.

Hyperion datasets require removal of bad pixels and de-striping before they are subjected to atmospheric correction. A local balancing filter was designed to remove bad columns from the Hyperion datasets. The designed filter targets only the visually identified band columns and replaces it by the 3×3 neighbourhood mean, without taking into account the bad column values. The designed filter can be used for all Hyperion images to be taken up for further studied.

The reflectance spectra extracted from ATCOR2 and FLAASH atmospheric correction models were compared using two methods. First method involved visual comparison for known absorption features of atmospheric gases and other known materials. ATCOR2 and FLAASH retrieved reflectance spectra indicated that both the models compensated for the O_2, and CO_2 atmospheric gas absorptions for Udaipur dataset. The two models underperformed for atmospheric water vapour at 940 nm and overestimated water vapour at 1140 nm. Second method on comparison involved comparison of the spectral similarity parameters using the field measured spectra and HyMap extracted spectra. Spectral similarity measures, SAM and NED do not have any specific range or thresholds, but the quality of the spectra is expressed with respect to the variation in values as compared to the standard reference. Spectral similarity results based on average SAM for ATCOR2 is 0.20 and 0.22 which is lower than the average SAM values of FLAASH (0.29 and 0.46). Normalized Euclidean Distance (NED) is considered as the best measure to judge the similarity between the two spectra. NED shows low values for FLAASH (0.74 and 0.82) as compared to average NED value of 2.79 and 2.80 for ATCOR2 corrected spectra in both the datasets. It is therefore concluded that FLAASH has outperformed ATCOR2. Consistency in the result of similarity for both Udaipur and Spain datasets indicated better performance of FLAASH for Hyperion datasets.

To assess the spectroscopic quality of the reflectance spectra extracted from FLAASH corrected Udaipur dataset, absorption analysis technique for band positioning was attempted for absorption feature at 2200 nm in Udaipur quartzite. Absorption analysis has not shown good results due lack of spectral quality of Hyperion in SWIR region and overlapping dominant absorption due to residual atmospheric water vapour in the shadow region.

Key Words: Atmospheric correction, ATCOR2, FLAASH, Hyperion, Spectral similarity measures, band positioning and absorption analysis

Acknowledgements

I express my sincere gratitude to my supervisors Dr. Milap Punia, Dr. Norman Kerle and Dr. H. M. A (Harald) van der Werff for their joint contribution, support, invaluable guidance, great insight and encouragement throughout this research. I express my earnest gratitude to Dr. Milap Punia, for his whole hearted support and introducing me to the subject of hyperspectral remote sensing that I seriously lacked and felt as though I am embarking on an unknown terrain. My sincere thanks to Dr. Norman and Dr. Harald for their encouragement, ever enthusiastic, spirited support and valuable guidance through out this research. Their in-depth knowledge in the field, creative and valuable comments in a simplified form were available so fast that I had hardly felt him being far away. Their mails were constant source of inspiration during my research project which has greatly helped in completing this thesis.

I am also grateful to Dr. V.K. Dadhawal, Dean Indian Institute of Remote Sensing, for accepting my nomination for the course. His special interests in the research topic, strong persuasion, and constructive suggestions lead to the completion of the project. I am thankful to Mr. P.L.N Raju, Head Geoinformatics, Mr. C. Jeganathan, Scientist 'E', Ms. Vandita Shrivastava, Scientist 'D' and for their innovative teaching style, constant support and suggestions for successful conduct of the course. Also, I would like to thank ITC for granting me the fellowship for taking up the studies at The Netherlands as part of this course. I would also like to thank Dr. J.F. Stoter, course coordinator, GFM2, midterm evaluator Dr. Ing. S.R.K.B. Heuel and Dr. D.G (David) Rossiter, for their critical reviews and suggestions to the study. Thanks are also due to all the faculties and staff members of the IIRS, those who helped me directly or indirectly during this programme.

I would like to express my sincere thanks to Dr. Indira Mishra, then Addition Chief Secretary and Dr. A.V.J Prasad, Principle Secretary and Director General, Department of Science and Technology, Government of Chhattisgarh for nominating me as a candidate for the M.Sc. (Geoinformatics) course organized in joint collaboration with Indian Institute of Remote Sensing, Dehradun, India and International Institute for Geo-information Science and Earth Observation, Enschede, The Netherlands. Thanks are also due to Dr. P.K. Bhat, Executive Director, and Er. N.V Deshpande, Sr. Scientist, Chhattisgarh Council of Science and Technology for their encouragement and support extended during the entire course tenure. I am thankful to Dr. Amit Dubey, for his constant encouragement during the programme.

I wish to express my deep sense of gratitude to Dr. R.N Vayas, Professor, Head Department of Geography for providing support during field work to Udaipur and Dr. R. Pandey, incharge ionspheric laboratory, Physics Department, Mohanlal Sukadia University for providing the data from research project on aerosol optical depth and water vapour. His valuable suggestions and discussions on atmospheric science have helped me in understanding the subject better.

My sincere thanks go to all fellow participants of Geo-Informatics and Geo-Hazards course. Informal friendly gatherings with them made my stay pleasant and cheerful. I am grateful to Ashok, Rajiv, Divyani, Shivraj and Lesslie for the constructive discussions, criticism and much needed moral boosting during the course. It was of immense help for me in my research project.

To my parents, whom I also dedicate this thesis. Without their support over the years towards my education, all this would not have been possible. I have gained great strength from them.

Last but not the least no words are enough to express thanks to my wife Sangeeta, for her love, patience and sacrifice over the last eighteen months. Without her whole hearted support none of this was possible. The smiling faces of my daughter Devshree and son Siddharth always gave me hope to continue. I gained strength from their cheerful adjustments during my prolonged absence from home.

Table of contents

List of figures

List of tables

1. Introduction

Earth's atmosphere has always been a centre of curiosity especially in the field of remote sensing. Interaction between electromagnetic radiation and earth's surface change the characteristics of the radiation. This modulated radiation, reflected from the earth's surface serves as the signal that is sensed by the optical airborne or spaceborne remote sensing systems. Atmosphere, the most essential component of our very existence is often considered as impediment for remote sensing of earth's surface. Need for reliable spectral information possesses both challenges and opportunities for Hyperspectral remote sensing in mapping, monitoring and exploration of earth's natural resources. To compensate for the effect of atmosphere on the Hyperspectral imaging system various algorithms atmospheric correction are used. The present research aims at evaluating the results obtained from various atmospheric correction algorithms for Hyperspectral data and compensate for spurious effects in atmospherically corrected spectra.

1.1. Atmospheric effects

The atmospheric gases, aerosols (airborne particulate matter) and clouds scatter and absorb solar radiation and can modulate the reflected radiation from the Earth. This attenuation can affect the intensity and spectral composition of the radiation (Lillesand and Kiefer, 1999). The principal effects are caused through the mechanism of atmospheric scattering and absorption due to gas molecules, aerosols and dust particles. The net effect of atmosphere varies with the path length that the radiation has to travel from source to sensor and also varies with the magnitude of the energy signal being sensed.

Atmospheric scattering is diffusion of radiation by particles in atmosphere. Gas molecules (O_3, O_2, CO_2, NO_2, CH_4, etc.) and haze exhibit Rayleigh scattering, which is inversely proportional to the forth power of the wavelength. Mie scattering is exhibited by the atmospheric particles that are of same size as the wavelength. The most significant and variable atmospheric effect is the non-selective scattering is exhibited by aerosols (water droplets) that have particle size much larger than the wavelength energy (visible, near to mid infra red) being sensed. Scattering by atmospheric particles is the dominant mechanism that leads to radiometric distortions in the image data, in addition to possible sensor malfunction effects (Lillesand and Kiefer, 1999).

In contrast to scattering, atmospheric absorption a selective process, results in effective loss of energy to atmospheric constituents. The most effective absorption is caused by aerosols, carbon dioxide and ozone (Lillesand and Kiefer, 1999). Absorption by these atmospheric molecules affect Hyperspectral remote sensing systems operate within the absorption regions of these gases. The energy (flux) leaving the pixel element of the earth is recorded by the sensor. The At-sensor radiance is defined as the radiant flux per unit solid angle per unit of projected area of the ground viewed by the sensor at that instance. This component of energy is mainly composed of the signal from the ground element, atmospheric interference and influence of adjacent ground element.

Absolute reflectance, expressed in percent is a ratio of reflected to incident flux. Deriving absolute reflectance for space borne platforms is of interest to all geoscientists as it offers an opportunity to know the composition, spectral property of material and compare field measured reflectance values.

The energy (flux) leaving the pixel element of the earth is recorded by the sensor. The At-sensor radiance is defined as the radiant flux per unit solid angle per unit of projected area of the ground viewed by the sensor at that instance. This component of energy is mainly composed of the signal from the ground element, atmospheric interference and influence of adjacent ground element. The signals received at the satellite are an integrated spectral response of the target within the designed spectral width of the sensor; this signal is provided to the user in form of digital numbers (DN). In raw unprocessed image DN values do not quantitatively correspond to the physical units such as radiance, reflectance or temperature. Thus, remote sensing studies which intend to utilize satellite data for estimation of quantitative spectral surface characteristics need to convert the DN to target reflectance/absolute reflectance (Pandya et al., 2002).

1.2. Atmospheric correction

Earth Observation by various optical systems around the globe by various agencies have their specific missions and purposes. But the real aim is always to know the surface characteristics of the features being mapped and how do they change with time and how they vary in time scales, or with some processes. Signals recorded from the satellite or airborne platforms in the visible and near infrared region are a combination of surface, atmospheric contributions and sensor errors. Thus, to enable quantitative studies of the earth surface, atmospheric perturbations need to be removed from the observed signal. The process of removing atmospheric contributions is commonly referred as atmospheric correction or atmospheric compensation

1.3. Hyper Spectral Remote Sensing

Hyperspectral spaceborne imaging spectrometers have been developed to measure the solar reflected upwelling radiance spectrum from ≈400 to ≈2500 nm at 5 to 10 nm resolution. The objectives of these imaging spectrometers are to use the molecular absorptions and constituent scattering characteristics expressed in the spectrum (Pantazis et al., 1998) to detect and identify the surface and atmospheric constituents present, assess and measure the expressed constituent concentrations, assign proportions to constituents in mixed spatial elements, delineate spatial distribution of the constituents, monitor changes in constituents through periodic data acquisitions and to validate, constrain and improve models.

Hyperspectral imagers typically collect data in contiguous narrow bands (up to several hundred bands) in the electromagnetic spectrum. They produce vast quantities of data because of the number of bands simultaneously imaged. Hyperspectral data provide unique capabilities to discern physical and chemical properties of Earth surface features not possible using current broad-band multi-spectral satellites. High spectral resolution allows identification of materials in the scene, while high spatial resolution locates those materials (Gross and Schott, 1998). Hence, hyperspectral data have enormous potential in target detection, high quality mapping, material mapping and identification.

Hyperspectral sensors are known to have sensor calibration error know as ‘Smiling Effect’. Smile effect is wavelength calibration problem that is commonly experienced with pushbroom sensors. This problem arises due to tendency of the sensor to have a slight variation in dispersion angle along the dimension of the signal entrance slit. Thus each row of the array has a slightly different wavelength calibration, which translates into small, spectral shifts in the data that depend on the pixel location or sample number along the cross-track direction of the data cube. One method of compensating for smile is through spectral polishing. Small shifts in central wavelength of channels that are located in atmospheric absorption regions are more likely to lead to errors in the retrieved surface reflectance,

usually seen as spikes and dips in the spectra. This spectral shift changes in the across-track direction of the acquired image line, but the nominal bandwidths remain constant. This nonlinear effect in spectral calibration, common for pushbroom sensors is referred to as "Smiling Effect.

Hyperspectral imaging sensors have been used for more than a decade to aid in the detection and identification of diverse surface targets, topographical and geological features but the datasets are not immune to the effects of the intervening atmosphere. Various atmospheric constituents attenuate the incident and upwelling reflectance and finally degrade the signal corresponding to the feature being sensed. Thus, if this atmospheric attenuation could be identified and corrected for by using existing radiative transfer models, better understanding of the earth features should be possible. In absence of these models the inferences would lead to erroneous detection, identification and quantification of the features of interest. Thus atmospheric correction refers to the removal of unwanted atmospheric components of the measured radiance

1.4. Problem definition

Atmosphere contributes significantly to the at-sensor radiance as Hyperspectral scanners have very narrow spectral resolution (Van der Meer and De Jong, 2003). Earlier studies have emphasized the need for handling atmospheric correction and spectral smiling effect for Hyperspectral data sets (Datt et al., 2003). One requirement for extracting calibrated spectra from Hyperion EO-1 is to first compensate for atmospheric effects using the existing atmospheric correction method. The spectra obtained from the atmospherically corrected channels are then compared with the ground measured spectra. Existing atmospheric correction algorithms have been applied and proposed for Hyperspectral sensors, but there is little literature to help in the selection of an effective method for general use (Hadjimitsis et al., 2004). Comparative studies to assess performance of atmospheric correction models reveal a poor absolute match in SWIR region (Kruse, 2003). This could be attributed to the shifts in radiometric and spectral calibration which could result in an error of 10 % at the edges of the Hyperion dataset (Liang and Fang, 2004). In a study to compensate for atmospheric effects and spectral smiling on canopy spectra, it was found that artifacts in the reflectance spectra, primarily associated with prominent absorption features in the spectra, are minimized by linear extrapolation, this study did not make a reference to the SWIR region in the results (Ramsey and Nelson, 2005). Spectrum-matching techniques applied to at-sensor radiance for wavelength calibration of Hyperspectral data have been also proposed. This algorithm is based on spectrum-matching of atmospheric water vapour, oxygen and carbon-dioxide bands and Fraunhofer features that quantifies solar absorption by the gases at frequencies corresponding to the atomic transition (Gao et al., 2004). This technique is advantageous when the ground reflectance measurements during sensor passes are unavailable. To compensate for the smiling effect, a mathematical method for removing artifacts from reflectance spectra is carried out. The available tools (normalized optical depth derivative NODD algorithm implemented in FLAASH) for performing spectral polishing assumes a linear spectral shift for the entire scene (Matthew et al., 2003). Another method to compensate for "smiling effect" using average central wavelengths for each band and dividing the image into several regions have also been suggested in earlier studies (Liang and Fang, 2004). Recent studies propose methods to evaluate spectral shifts in AVRIS Hyperspectral sensor based on the surface reflectance instead of calculating spectral shift based on at-sensor radiances (Guanter et al., 2006).

The present study is intended to examine the capability of two MOTRAN based models (ATCOR and FLAASH) to correct for atmospheric effects associated with the acquisition of Hyperion data. The study proposes to minimize the smiling effect in the spectra. The atmospherically corrected spectra

will then be tested for spectral similarity to ground spectra using spectral similarity methods, and analyze spectra based on the unique absorption features at known bands for absorption analysis for band positioning (band positioning and absorption analysis).

1.5. Motivation

Resource monitoring and management for a state require establishing a baseline data. These kinds of databases are primarily important for national accounting of natural resources and planning at regular intervals. Minerals and ores are the economic backbone for a country like India. The Indian mining industry has targeted to increase its contribution to the Gross Domestic Product (GDP) from the existing 3.5% to over 10%.

Rajasthan is one of the largest mining states in India, producing more than 60 minerals. Application of these techniques can be useful for identification and material mapping to meet the present targets and growing future demands. This calls for systematic research to understand the hyperspectral datasets so as to enable the mineral exploratory agencies of the state to take up newer areas to ensure unhindered availability of mineral raw material for the realization of national goals. Thus, use of hyperspectral techniques coupled with analytical techniques would further enhance our understanding and contribute towards sustainable development.

Such studies require atmospheric compensation, and for this a robust algorithm is needed to retrieve the surface characteristics. Typically, physical/physics-based models are chosen for this task. Two of the more commonly used models are ATCOR-2 for spaceborne sensors and FLAASH. While ATCOR-2 and FLAASH apply same methods of atmospheric compensation, both use different techniques to account for the effects of atmospheric water vapor and influence of adjacent ground on the hyperspectral measurements. This variation results in difference in extracted spectral curve for same pixel.

1.6. Research objectives

This study is intended to test their efficiency for EO-1 Hyperion datasets in retrieving calibrated spectral profile. The atmospherically corrected spectra will then be tested by spectral similarity methods in an attempt to analyze spectra based on the unique absorption features at known bands, and by comparing them with the standard spectral curves in spectral library (absorption analysis technique for band positioning). The objectives of the present study are:

- To derive apparent reflectance from radiative transfer models for Hyperion datasets.
- To understand and analyze absorptions along the contiguous spectra so as to enable effective pre-processing.
- To evaluate the comparative utility of atmospheric correction models.
- Attempt band positioning absorption analysis and evaluate its effectiveness.

1.7. Research questions

Some of the research questions to be addressed only from the perspective of Hyperion are:

1. What is the usefulness of existing atmospheric correction models?
2. How good are the atmospheric correction models for VNIR and SWIR portion of Hyperion?
3. How can the smiling effect in the spectra be minimised?
4. How effective is the absorption analysis technique for band positioning?

1.8. Data and study area

Udaipur, Rajasthan, India and Rodalquilar, Spain have been selected for the present study. Rajasthan is one of the mineral rich states of India. This north-western state of India occupies a place of pride in production and marketing of metallic and non metallic minerals in India Figure 1-1. The Aravalli range, one of the oldest mountain ranges of the world runs along the NE–SW direction for more than 720 km, covering nearly 40,000 km^2. The study area (Longitude 73° 32′ 58″ to 73° 49′ 35″ E and Latitude 24° 08′ 18″ to 24° 59′ 53″ N) covers an area of about 750 km^2 of this main block of the Aravalli range corresponding to path and row number 146/40 corresponding to full scene of Hyperion. The available Hyperion scene covers major parts of Udaipur city, and part of the Hindustan Zinc Limited-Zawar mines area, which are geologically part of Zawar formation of Upper Arawalli Group. The region is dry for most of the year except the rainy season, and exhibits semiarid climate. Monsoon winds mainly contribute to the rainfall in this region mainly during June–September; non-monsoon rainfall is limited and irregular. Annual rainfall in this region varies from 10 cm in the north-west to 90 cm in the south east. Water resources, vegetation, agriculture and aquifer condition in this region vary mainly due to variations in physiographic, geomorphic and climatic conditions.

Rodalquilar mineral district is situated in the Sierra del Cabo de Gata volcanic field, in the south-eastern part of Spain. Epithermal deposits of precious and base metals have been reported in veins or in hydrothermal breccieas, associated with hydrothermally altered wall rocks (Cunningham et al., 1990). The Rodalquilar gold deposits are located between longitude 2° 05′ W to 2° 00′W and latitude 36° 50′N to 36° 35′N (Figure 1-2).

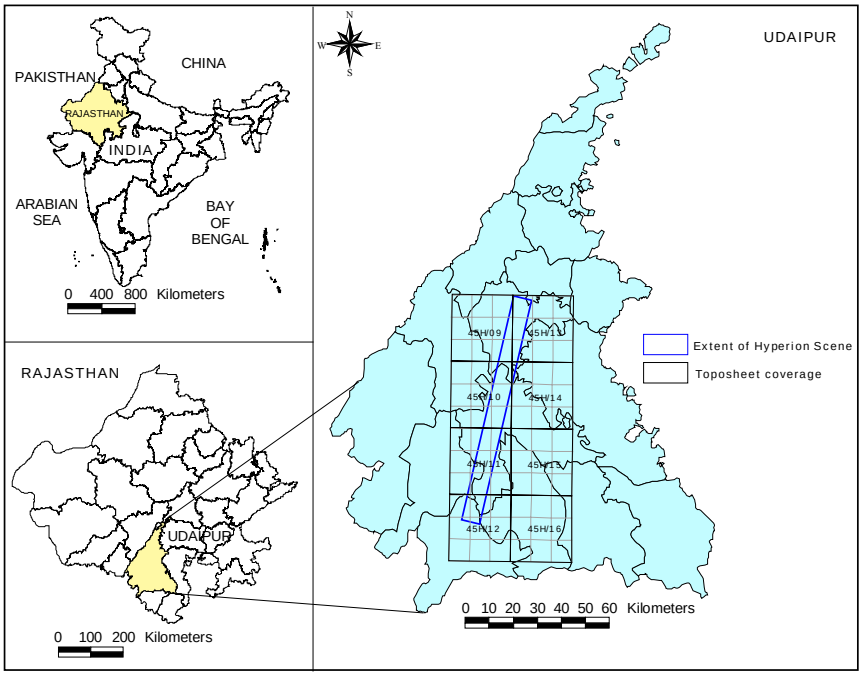

Figure 1-1India, Rajasthan State and Udaipur district, with toposheet coverage and Hyperion scene foot print

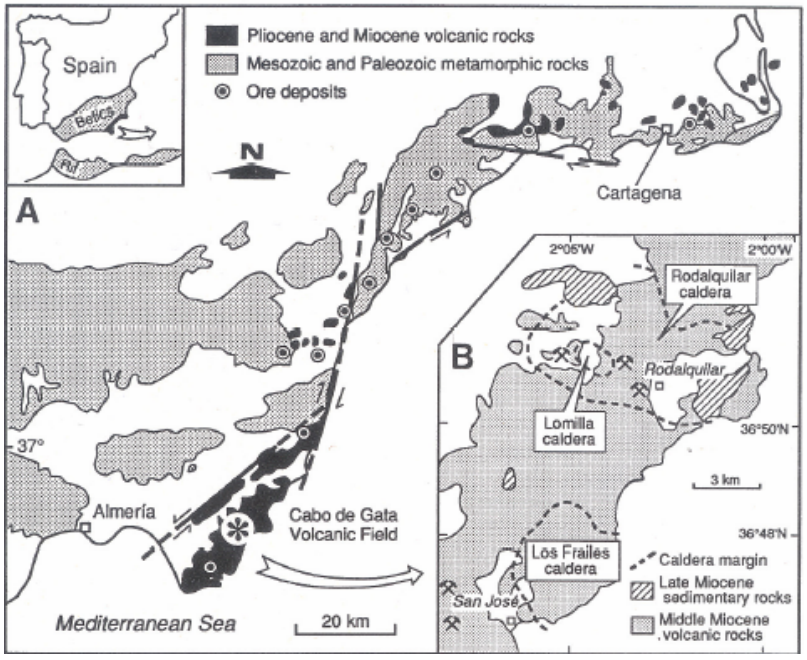

Figure 1-2 a) Geographic and gological setting of Cobo de Gata volcanic field. b) Central part of Cobo de Gata volcanic field [after (Cunningham et al., 1990)].

1.8.1. Data used

1.8.1.1. Hyperion

Hyperion images of Udaipur and Rodalquilar correspond to the January 19, 2004 and February 6th 2003. There are 220 unique bands with spectral range of 357 - 2576 nm at 10 nm band width. The Level 1 radiometric product used in the present study has 242 bands. However, only 198 bands are calibrated (band 8 to 57 for VNIR and 77 to 224 in SWIR region) (Datt et al., 2003). Because of an overlap between focal planes of VNIR and SWIR, there are only 196 unique channels. The reason for not calibrating all 242 channels is low detector responsively. The bands that are not calibrated are set to zero. The sensor has a nominal ground instantaneous field of view (GIFOV) of 30 m and 12-bit radiometric quantization (Pearlman et al., 2003). Hyperion sensor characteristics are shown in Table 1-1.

Table 1-1 Hyperion characteristics

Sensor altitude	705 kms	No. of rows	256
Spatial resolution	30 mts	No. of columns	3128
Radiometric resolution	16 Bits	VNIR range	0.45 - 1.35
Swath	7.2 kms	SWIR range	1.40 - 2.48
IFOV (mrad)	0.043		

1.8.2. Landsat-7

The Landsat programme is the oldest space-borne Earth Observation programme. Its detector records the EMR in seven bands. The Landsat 7 satellite, launched from Vandenburg Air Force launch pad on April 15, 1999. The Landsat platforms operate following a sunsynchronous, near polar orbit. A pre-processed data product, an orthorectified Landsat-7 Enhanced Thematic Mapper (ETM+) from the

Global Landcover Facility (GLCF) of the Institute for Advanced Computer Studies, a NASA-funded member of the Earth Science Information Partnership at the University of Maryland is used for the present study. (http://glcf.umiacs.umd.edu/index.shtml). ETM+ has 8 discrete bands in blue (0.45-0.52 µm), green (0.52-0.60 µm), red (0.63-0.69 µm), NIR (0.76-0.90 µm), SWIR (1.55-1.75 µm) and PAN (0.50-0.95 µm). The data pertaining to the study area were acquired on 15th October; 2000.The sensor characteristics of ETM+ are given in Table 1-2. This dataset has been used as reference image for georefrenceing the Hyperion image of Udaipur.

Table 1-2 Landsat-7 ETM+ characteristics

Sensor altitude	705 km
Swath	185 km
Spatial resolution	10 m (PAN), 30 m (bands 1-5,7), 60 m (band 7)
Radiometric resolution	8 Bits
Temporal resolution	16 days
Path	148
Row	43

1.8.3. HyMap

The HyMap is an airborne imaging platform developed by Intregraded Spectronics, Australia. The sensor payload is wing mounted typically flown at 2.5 km altitude. HyMap is a 126 channel instrument that collects data in cross-track direction with a spectral coverage of 0.45 to 2.5 µm wavelength. Spectral coverage is nearly continuous in visible-to-near-infrared (VNIR) and shortwave-infrared (SWIR) regions with small gaps at 1.4 and 1.9 µm atmospheric water absorption bands. The spatial configuration of the instrument accounts for an instantaneous-field-of-view (IFOV) of 2.5 mrad along track and 2.0 mrad across track resulting in a pixel size of the order of 5 m for the data used in the present study. The HyMap data were atmospherically and geometrically corrected at ITC, using ATCOR4 model. The HyMap image was acquired during the HyEurope 2005 campaign on 15th May. Table 1-3 shows the sensor characteristic of HyMap. Figure 1-3 shows foot print of HyMap on Rodalquilar, Spain study area.

Table 1-3 HyMap instrument characterises (Cocks et al., 1998)

Spectral module	**Wavelength range (µm)**	**Bandwidth (nm)**	**Spectral sampling (nm)**
VIS	0.45-0.89	15-16	15
NIR	0.89-1.35	15-16	15
SWIR1	1.40-1.80	15-16	13
SWIR2	1.95-2.48	18-48	17
IFOV: 2.5 m along track and 2.0 m across track		Swath: 2.3 km at 5 m IFOV: 4.6 km at IFOV	
FOV: 60 (512 pixels)			

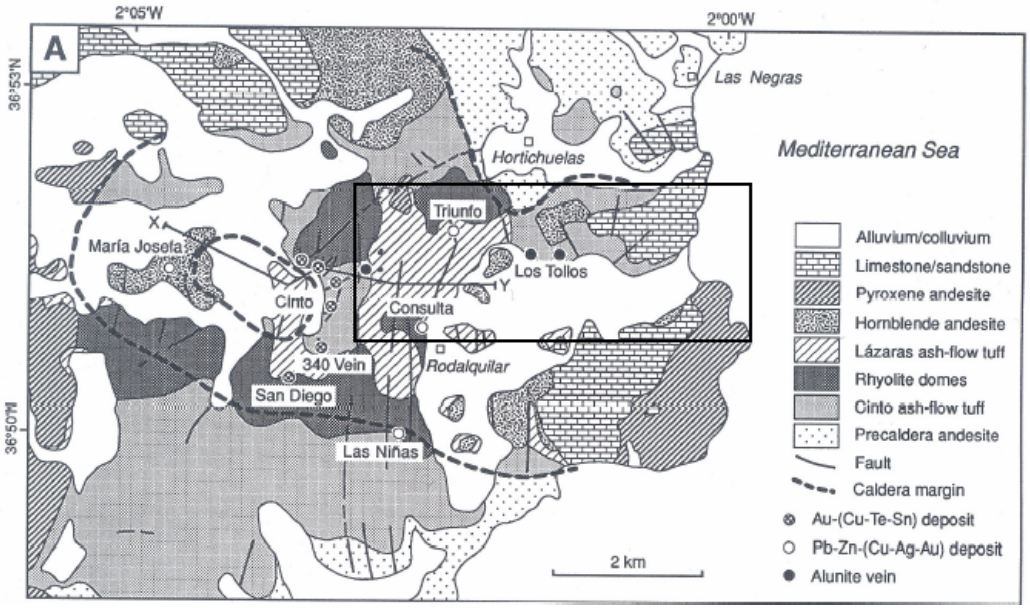

Figure 1-3 Generalized geological map of Rodalquilar caldera [after (Cunningham et al., 1990)] with approximate foot print of the HyMap scene.

1.8.4. Ancillary data

For background information about the study area 1:50,000 scale SOI toposheets (45H/9, 45H/10, 45H/11, 45H/12, 45H/13 and 45H/14), Geological maps published by Geological Survey of India, and field spectra collect using FieldSpec-Pro have been used for the present study.

1.9. Methodology adopted

The present study is intended to compare the retrieved surface reflectance from both ATCOR and FLAASH atmospheric correction models. Figure 1-4 shows outline of the methodology adopted in the present study.

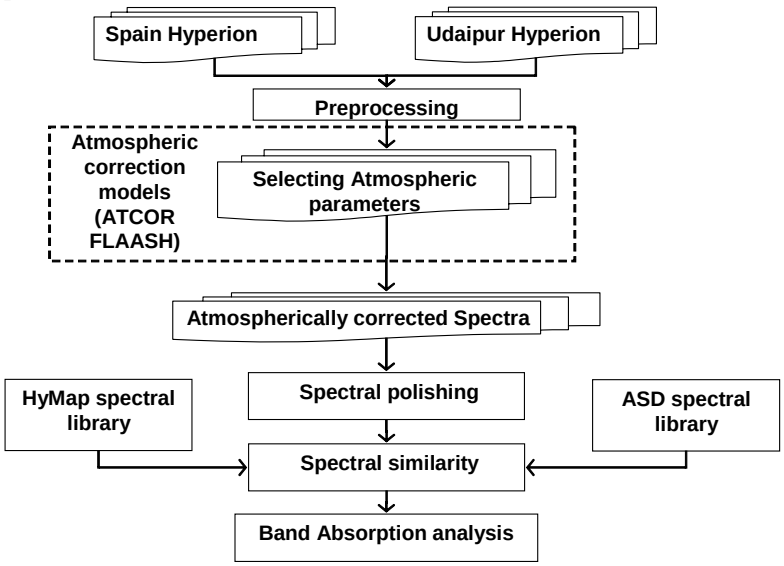

Figure 1-4 Methodology adopted for the study

The resultant image spectra for Udaipur were compared with the ASD extracted spectra. For Spain the Hymap image spectra were taken as reference. To see whether the atmospherically corrected Hyperion spectra of Udaipur behave in accordance with the spectroscopic band absorption characteristics at particular band positions, band positioning and absorption analysis was carried out.

1.10. Chapter schema

This thesis is organized in seven chapters. Chapter 1 lays the rationale for the present study with set objectives and research questions to be attempted. Chapter 2 describe the atmospheric correction models used in the present study. The processing steps adopted and description of the input parameters to the atmospheric correction models are discussed in Chapter 3. Chapter 4 describes the field investigations and data collected and processed during the present study. The effects of processing carried out in the present study are analyzed in chapter 5. This chapter also describes the comparison results obtained within and between the different selected atmospheric correction models. Chapter 6 discusses the research findings and proposes recommendations for further research. Finally the citations used in the present study are enumerated in bibliography of references in chapter 7.

2. Atmospheric Correction Models

Atmospheric correction models are available in ready to use softwares, to name a few are: Atmospheric CORrection Now (ATCOR), Fast Line-of-Sight Atmospheric Analysis of Spectral Hypercubes (FLAASH) developed on Moderate Resolution Atmospheric Radiance and Transmittance Model (MODTRAN); Atmosphere REMoval Program (ATRIM), ATCPRO and High Accuracy ATmospheric Correction for Hyperspectral data (HATCH) developed on 5S Code (Simulation of the Satellite Signal in the Solar Spectrum) and 6S code (Second Simulation of the Satellite Signal in the Solar Spectrum) respectively. The available methods of atmospheric correction give the theoretical background of the processes involved in atmospheric correction. ATCOR2 and FLAASH atmospheric correction models used in the present study are described here.

2.1. Atmospheric correction methods

The first step in the processing chain, often referred to as pre-processing, involves radiometric and geometric corrections. Atmospheric correction methods employed to remove atmospheric attenuation are grouped under radiometric corrections. EO-1 product generation system (EPGS) has an in-orbit calibration plan for the Hyperion EO-1 hyperspectral payload. The internal calibration source uses four Welch Allyn quartz tungsten halogen (QTH) lamps to illuminate the back of the telescope cover in the closed position. The cover, located at the aperture stop of the telescope, is painted with diffuse, reflecting, white, silicone, thermal control paint (Jarecke et al., 2002). The parameters recorded during in-orbit calibration procedure are used to radiometrically calibration of on board sensors.

The method to be used for atmospheric correction is a function of nature of problem, the type of remote sensing data, the amount of in situ historical atmospheric information available, and how accurate the bio-physical information is to be extracted from the remote sensing data (Jensen, 1996). To process hyperspectral image datasets, statistical based relative atmospheric correction methods and physics based absolute correction models are available.

An image comprises of a series of spectral bands, the pixels of which each have a digital number (DN). In a raw unprocessed image, pixel DN is a linearly transformed representation of at-sensor radiance for a discrete resolved area of the Earth's surface (Lillesand and Kiefer, 1999). Image spectrometric studies and atmospheric correction operations, however, need at-sensor radiance. The radiance-to-DN procedure of image acquisition for each spectral wavelength must be inverted to derive radiance from DN.

$$DN = \left(\frac{DN_{\max}}{L_{\max} - L_{\min}} \right) \times \left(L - L_{\min} \right)$$

Equation 2-1

$$L = \left(\frac{L_{\max} - L_{\min}}{DN_{\max}} \right) \times DN + L_{\min}$$

Equation 2-2

As pixel DN is a simple linear transformation of radiance, the slope and offset of this linear transformation (which is specific for each spectral band, each sensor and initial calibration) can be used to calculate radiance L (measured in $W/m^2/sr/\mu m$) using equation-2-2, and inversely used to calculate pixel DN using equation-2-1. The gain and offset values are unique for each spectral band

acquired by a particular sensor. These values change over the life span of a sensor, so the most recent values are used. For Hyperion, these values are made available to the user with the dataset.

2.1.1. Radiance to reflectance

At sensor-reflectance involves taking into account temporal changes in solar illumination due to Earth-Sun geometry, as it changes with time of the year of imaging. The solar spectral irradiance (incident energy reaching the target) of the light reaching the atmosphere is reasonably well characterized; however, the spectrum of the solar radiation reaching the ground is altered temporally and geographically because of changing atmosphere. Such atmospheric modulation effects have to be accounted for in order to recover reliable reflectance spectra of materials on the ground. The effect of scattering on remotely sensed solar radiation reflected by the ground surface is most commonly given by:

$$\rho_p = \frac{\pi . L_\lambda . d^2}{ESUN_\lambda . \cos\theta_S}$$

Equation 2-3

Where

ρ_p = Unitless planetary reflectance
L_λ = Spectral radiance at the sensor's aperture
d = Earth-Sun distance
$ESUN_\lambda$ = Mean solar Exoatmospheric irradiances
θ = Solar zenith angle in degrees

The Earth-Sun distance has been calculated from the given formula:

$$d = 1 - 0.01672 \times \cos\left(0.9856 \times \left(Jday - 4\right)\right)$$

Equation 2-4

Where
Jday = Julian day for day of satellite pass

The above formula of "Top-of-Atmosphere" (TOA) reflectance has been further simplified as:

$$L^{'} = L_p + Le^{-\tau/\cos\theta}$$

Equation 2-5

Where L′ the radiance measured at top of the atmosphere; Lp is the path radiance and Le is the monochromatic radiance reflected by the surface at ground level; τ, the optical thickness of the atmosphere; θ the zenith viewing angle. Equation 2.3 is valid if the pixel size or IFOV is relatively smaller than the scale of scattering effect, and the path radiance (L_p) includes atmospheric radiance (La) and background radiance (Lb) (Deschamps et al., 1983). Since the reflectance spectrum is independent of the illumination, the reflectance spectrum enables identification of materials in a scene by matching the scene reflectance spectra to a library of known spectra.

At-sensor reflectance still has atmospheric scattering effects present. Atmospheric effects have to be removed by deriving ratios of different spectral-bands. This can be undertaken in two ways (Figure 2-1), (i) by using reflectance as the basis of change detection over time; or (ii) by using reflectance in physics based absolute models. Several studies have been carried out in evolving methods for quantifying and compensating for the deleterious effects of the atmosphere on spectral imaging, resulting in a variety of atmospheric correction methods and models.

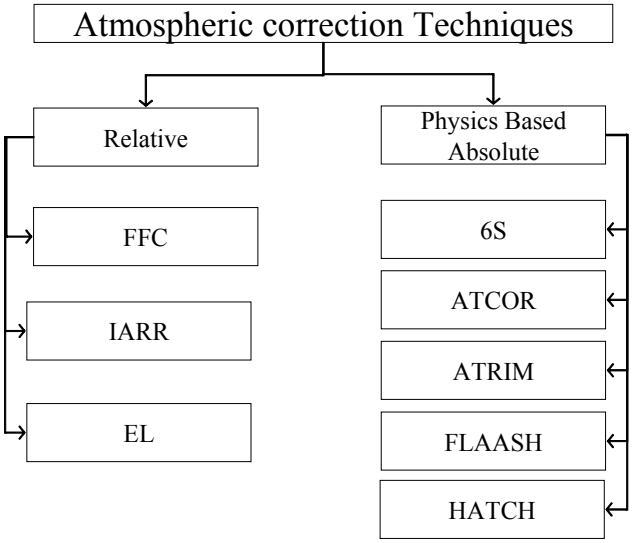

Figure 2-1 Available atmospheric correction techniques

2.1.2. Relative atmospheric correction

The statistical or empirical based atmospheric correction models provide good estimates of the surface reflectance, assuming that the spectral reflectance of reference objects are accurately known. Relative methods avoid the evaluation of atmospheric components of any kind. These methods use the input information from the image itself. They rely on the assumption that for one image band/channel the relation between the radiances at TOA and at ground level follows a linear trend for the variety of earth features present in the image. This linear relation is in fact an approximation to reality, but precise enough to solve practical applications where there are other more important source of errors (Parodi and Prakash, 2004). These methods are useful when there is very little information about the ground. These statistical techniques are used to adjust or normalize the raw radiance data. Some of the relative atmospheric correction models are briefly described in this section.

Flat Field Correction (FFC) technique is used to normalize images to an area of known uniform "flat" reflectance (Kruse et al., 2003b). The method requires locating a large, spectrally flat, spectrally uniform area in the data, usually defined as a Region of Interest (ROI). The radiance spectrum from this area is assumed to be composed of primarily atmospheric effects and the solar spectrum. The average radiance spectrum from the ROI is used as the reference spectrum, which is then divided into the spectrum at each pixel of the image. FFC normalizes the hyperspectral data to an area of known flat reflectance, and derives relative reflectance from hyperspectral data. The resultant apparent reflectance is comparable with laboratory spectra.

Internal Average Relative Reflectance (IARR) calibration technique is used to normalize images to a scene average spectrum. This is particularly effective for reducing imaging spectrometer data to relative reflectance in an area where no ground measurements exist and little is known about the scene (Kruse et al., 2003b). It works best for arid areas with no vegetation. The IARR calibration is performed by calculating an average spectrum for the entire scene and using this as the reference spectrum. Apparent reflectance is calculated for each pixel of the image by dividing the reference spectrum into the spectrum for each pixel.

Empirical Line Calibration technique is used to force image data to match selected field reflectance spectra (Kruse et al., 1990). This method requires ground measurements and/or knowledge. Two or more ground targets are identified and reflectance is measured in the field. Usually the targets consist

of at least one bright and one dark area. The same two targets are identified in images and average spectra are extracted for Regions of Interest. A linear regression is calculated between the field reflectance spectra and the image radiance spectra to determine a linear transform from radiance to reflectance for each band of the AVIRIS data set. Gains and offsets calculated in the regression are applied to the radiance spectra for each pixel to produce apparent reflectance on a pixel-by-pixel basis. This process is equivalent to removing the solar radiance and the atmospheric path radiance from the measured signal.

The relative methods are computationally fast, but the information pertaining to the intervening atmosphere is not derived in these approaches. These techniques are considered more of a calibration tool than an atmospheric correction model.

2.1.3. Absolute atmospheric correction

Absolute atmospheric correction methods require a description of the components in the atmospheric profile. The output of these methods is an image that matches the reflectance of the ground pixels with a maximum estimated error of 10 %, if atmospheric profiling is adequate enough. This image can be used for flux quantifications and parameter evolution assessments. The advantage of these methods is that ground reflectance can be evaluated under any atmospheric condition, altitude and relative geometry between sun and satellite. The disadvantage is that the atmospheric profiling required for these methods is rarely available. Regarding this inconvenience, a sub-classification of absolute atmospheric correction methods could be based on the accuracy of the method related to the effort in obtaining the required data (Parodi and Prakash, 2004). Physics based absolute atmospheric correction models derive spectral radiance at the satellite sensor (L_λ) in equation 2.1, based on satellite ephemeris parameters and atmospheric constituents. The atmospheric constituents can be in-situ measurements at the time of the satellite pass or can be derived from the satellite data. Current efforts are oriented towards the use of accurate calculation techniques to retrieve atmospheric parameters from the input hyperspectral images.

One of the earliest absolute atmospheric correction method using radiative transfer approaches to simulating the atmosphere–surface system was presented by Turner and Spencer in 1972. During the 1980s, considerable work was done on the atmospheric correction of satellite imagery and improvements in modeling and computational capabilities led to the development of the 5S atmospheric radiation model in 1990s which was used extensively for the atmospheric correction of airborne visible/infrared imaging spectrometer (AVIRIS) datasets. Since 1990 numerous radiative transfer models have been developed, the most popular amongst these is a publicly available code MODTRAN, developed by Spectral Science, Inc. and Air Force Research Laboratory.

Radiative transfer models (RTM) can be used for computing either radiances (intensities) or irradiances (fluxes) for a wide variety of atmospheric and surface conditions. They require a full description of the atmospheric components at fixed altitudes throughout the atmosphere. LOWTRAN, MODTRAN, Code 5S and 6S are all reference radiative transfer models. MODTRAN is becoming the standard for research studies in both the thermal and the visible spectrums. Code 5S has been found useful for ocean-colour sensors and land-surface analysis (Tanre et al., 1990). The code 5S forms the processing basic for development of MODTRAN. Figure 2-2 shows the general flow of processing steps employed in 5S programme.

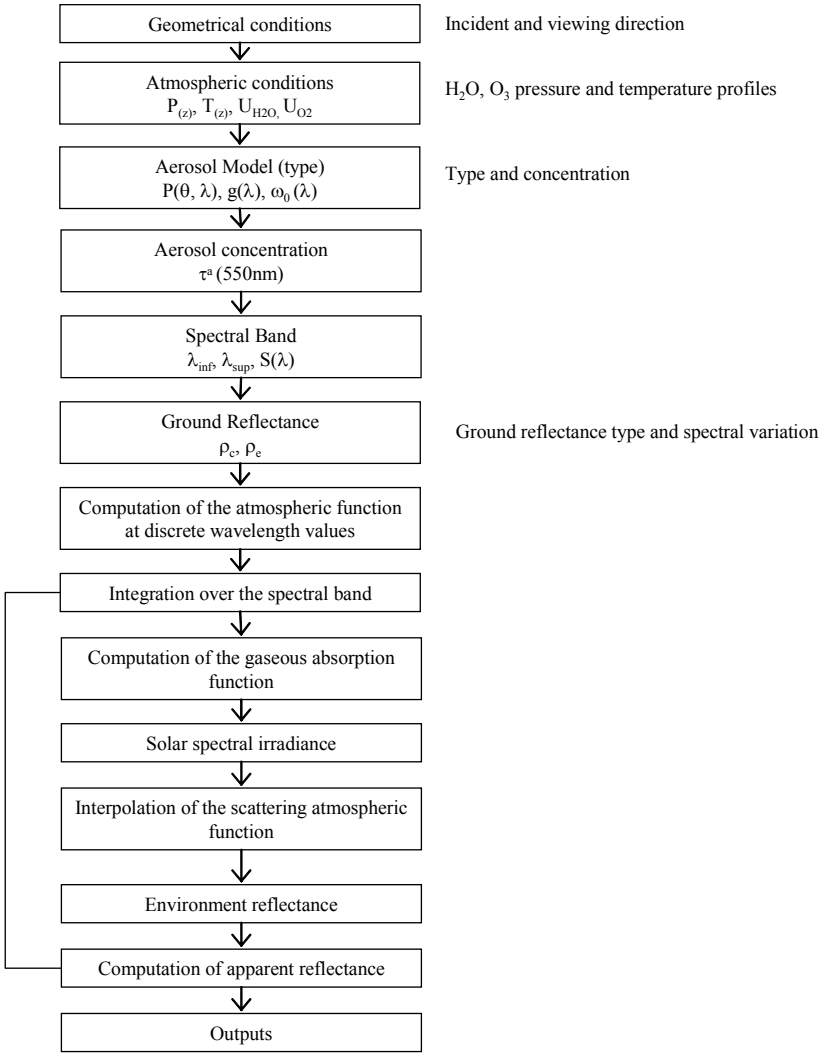

Figure 2-2 General flow chart for code 5S programme (Tanre et al., 1990)

The use of RTMs is not limited to mere calculation of reflectance and radiances at ground level. Since they operate with a wide variety of parameters, they also allow the study of optics, astrophysics, and atmospheric science (Parodi and Prakash, 2004). The actual internal physical solutions provided by these models are discussed in section 2.2.

2.2. Moderate Resolution Atmospheric Transmission (MODTRAN)

The Moderate Resolution Transmittance (MODTRAN) Code calculates atmospheric transmittance and radiance for frequencies from 0 to 200nm at moderate spectral resolution of 0.0001 μm (1 cm^{-1}). MODTRAN was developed for higher spectral resolution for molecular band parameterization, spherical refractive geometry, solar and lunar source functions, scattering (Rayleigh, Mie, single and multiple), and default profiles (gases, aerosols, clouds, fogs, and rain) (Kneizys et al., 1996). The upgraded MODTRAN4 corrects for water line parameter errors parameters led to a very small increase in the retrieved water column amount, from 1550 to 1570 atm-cm, due to a ~1% change in the 1130 nm band strength (Matthew et al., 2000).

The standard mathematical expression for spectral radiance at a sensor pixel applicable to SWIR through UV wavelengths, where thermal emission is negligible is expressed as:

$$L^* = \left[\frac{A\rho}{(1-\rho eS)}\right] + \left[\frac{B\rho e}{(1-\rho eS)}\right] + L^* a$$

Equation 2-6

Where, L^* is spectral radiance at sensor, ρ is the pixel surface reflectance, ρe is an average surface reflectance for the pixel and the surrounding region, S is the spherical albedo of the atmosphere, L*a is the radiance backscattered by the atmosphere and A and B are coefficients that depend on atmospheric and geometric conditions. The first term in the above equation corresponds to the radiance from the surface that travels directly into the sensor, while the second term corresponds to the radiance from the surface that is scattered by the atmosphere into the sensor. The distinction between ρ and ρ_e accounts for the "adjacency effect" (spatial mixing of radiance among nearby pixels) that is caused by atmospheric scattering. The adjacency effect correction can be turned off by setting $\rho_e = \rho$. For a specified model atmosphere the values of A, B, S and L*a in above equation can be determined empirically from the standard MODTRAN4 outputs of total and direct-from-the-ground spectral radiances computed at three different surface reflectance values, such as 0, 0.5 and 1. The viewing and solar angles of the measurement and nominal values for the surface elevation, aerosol type and visible range for the scene are used. To account for possible variations in column water vapor across the scene these calculations are looped over a series of varying water profiles. The water retrieval is performed rapidly with a 2-dimensional look-up table (LUT) constructed from the MODTRAN4 outputs using "Delaunay triangulation" procedure. After the water retrieval is performed, Equation 2-4 is solved for the pixel surface reflectance in all of the sensor channels. A procedure analogous to the water vapor determination can be used to retrieve a scene elevation map. Here the MODTRAN4 calculations are looped over elevation rather than water vapor concentrations and an absorption band of a uniformly mixed gas such as O_2 or CO_2 is interrogated.

MODTRAN4 options can be selected that control the tradeoff between accuracy and computational speed. These include the number of water vapor column amounts, the multiple scattering algorithm (Isaacs 2-stream or DISORT n-stream) (Matthew et al., 2000). Table 2-1 show the characteristic features of MODTRAN.

Table 2-1 Characteristics of LOWTRAN/MODTRAN and 6S Radiative transfer models (Parodi and Prakash, 2004)

Model characteristics	**LOWTRAN/ MODTRAN**
Numerical approximation method(s)	Two-stream, including atmospheric refraction; discrete ordinates also in MODTRAN-3
Spectral resolution	20 cm^{-1} (LOWTRAN); 2 cm^{-1} (MODTRAN)
Clouds	Eight cloud models; user specified optical properties
Aerosols	Four optical models
Gas absorption	Principle and trace gases
Atmospheric profiles	Standard and user-specified
Surface characteristics	Lambertian, no built-in models
Primary output parameter	Radiance

2.2.1. Aerosol retrieval

Atmospheric aerosol impacts not only the quantity of backscatter but also the attenuation of the surface-reflected radiance and the magnitude of the adjacency effect. These may be refined, as desired, through iterative comparisons of reflectance retrievals against "known" surfaces. This iterative process is tedious and time-consuming, however. Recently (Matthew et al., 2003) several methods for single-

step retrieval of the visible range, which is inversely related to the aerosol amount, extracted from the scene information. This aerosol retrieval is most conveniently performed as the first step in the atmospheric correction process (prior to the water vapor determination). This method assumes that the surface reflectance at one or a set of adjacent wavelength channels is known for one or more "reference" pixels. Best results are obtained using visible wavelengths and either a very dark surface, such as vegetation or deep calm water, or a very bright surface, such as a white calibration target that is large enough to fill at least one pixel. The sensor's absolute radiance calibration must be very accurate in the latter case, where the main aerosol effect is attenuation rather than backscattering.

2.2.2. Radiance data simulation

MODTRAN4 calculation described is performed for the desired sensing geometry and atmospheric model; the Equation (2-4) parameters are derived from the calculations; the reflectance is spatially averaged to generate ρe; and the pixel radiances are calculated directly from Equation (2-4) (Matthew et al., 2000).

2.2.3. ATCOR and FLAASH

Atmospheric and Topographic Correction model (ATCOR) and Fast Line-of-sight Atmospheric Analysis of Spectral Hypercubes (FLAASH) are the calibration programmes used to convert radiance into corresponding reflectance. They incorporate the new development of MODTRAN-based radiation transfer model (MODTRAN4) into the code for modelling radiation transfer properties, and include a correction for pixel mixing due to scattering of reflected radiance from surroundings into the pixel. The user is provided the choice of selecting the standard MODTRAN model for atmosphere and aerosol types to represent the scene, and a unique MODTRAN solution is computed for each image. FLAASH also includes a correction for the “adjacency effect” (pixel mixing due to scattering of surface reflected radiance), provides an option to compute a scene-average visibility (i.e., aerosol/haze amount), and utilizes the most advanced techniques for handling particularly stressing atmospheric conditions (such as the presence of clouds). Other features include a cirrus and opaque cloud classification map and adjustable spectral “polishing” for artifact suppression.

2.2.4. ATCOR algorithm

The ATCOR software was developed by DLR (German Aerospace Center) and the IDL version is licensed to ReSe for commercial marketing. ATCOR is useful for processing bands in the solar region from 400 - 2500 nm. The satellite versions of ATCOR are restricted to narrow/medium field-of-view instruments, because the scan angle dependence of atmospheric transmittance and radiance functions is neglected. ATCOR-2 mostly used for flat terrain, considers two geometric degrees of freedom (DOF) of the flat plane, where as ATCOR-3 takes into consideration terrain height and is useful for mountainous terrain, with three degrees of freedom. The airborne version ATCOR-4 accounts for scan angle effects with four geometric DOF’s: x, y, z and scan angle and is intended for wide field-of-view multispectral and hyperspectral imagery.

The total signal at the sensor consists of three components: path radiance, reflected radiation from the viewed pixel and radiation from the neighborhood. The atmospheric conditions (water vapor content, aerosol type, visibility) for a scene can be estimated using ATCOR. The total signal at the sensor consists of four components: path radiance, reflected radiation from the viewed pixel, scattered radiation from the neighborhood, and terrain radiation reflected to the pixel Figure 2-3. The atmospheric conditions (water vapor content, aerosol type, visibility) for a scene can be estimated with the SPECTRA module within ATCOR3. Then, the surface reflectance spectrum of a target in the scene

can be viewed as a function of the selected atmospheric parameters. It can be compared to typical library spectra.

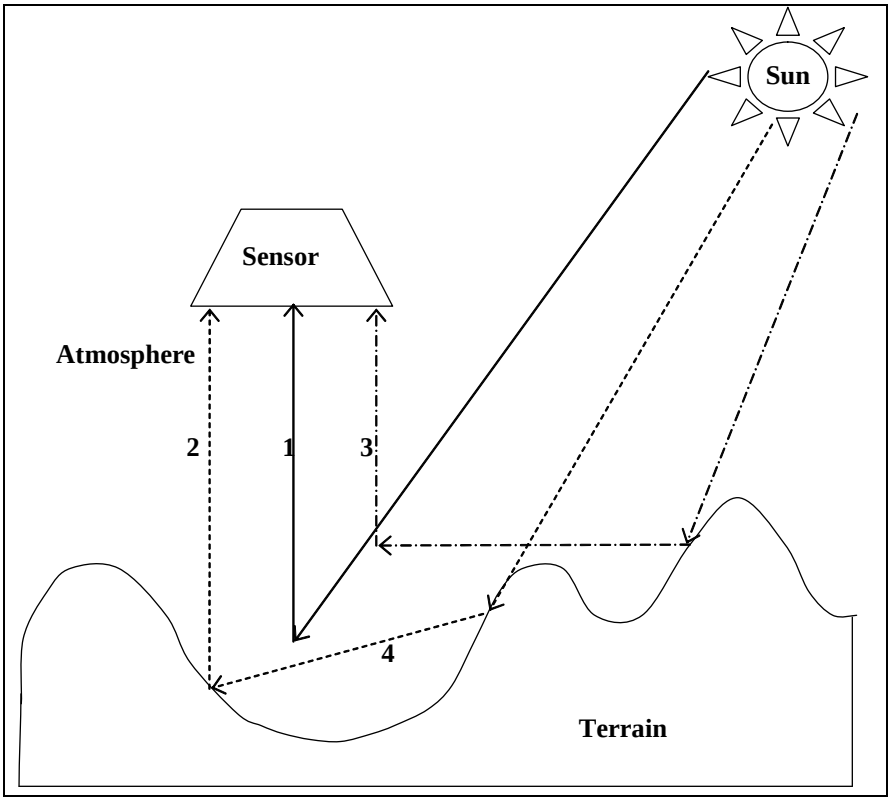

Figure 2-3 Schematic sketch of radiation components for a rugged terrain.

Component 1: path radiance: radiation scattered by the atmosphere (photons without ground contact).
Component 2: reflected radiation from the viewed pixel.
Component 3: adjacency radiation: ground reflected from the neighbourhood and scattered into the view direction.
Component 4: terrain radiation reflected to the pixel (from opposite hills, according to the terrain view factor). Only component 2 contains information from the viewed pixel.
The at sensor reflectance calculation is performed iteratively in 5 or 6 major steps:

- Step 1: the influence of the neighbourhood is neglected. A start value for the ground reflectance of the surrounding topography is employed. The path radiance component is subtracted from the signal. Shadow cast by surrounding topography is included (result of SHADOW program).
- Step 2: a low pass filtered reflectance image of step 1 is calculated. The filter size can be specified by the user (typically 1-2 km, corresponding to a range of R = 0.5 - 1 km for the adjacency effect).
- Step 3: The results of the SKYVIEW program are employed to calculate the contribution of the reflected terrain radiation (component 4) averaging over a box of size 0.5 km. The terrain view factor is 1 – skyview factor. This step is iterated three times for convergence.
- Step 4: Adjacency effect: the atmospheric crosstalk between adjacent fields of different reflectances is taken into account (see flat terrain).
- Step 5: Spherical albedo effect: the global flux on the ground depends on the large-scale (1 km) average reflectance. The global flux in the atmospheric LUT's is calculated for a fixed

reflectance=0.15. This iteration performs the update for the spatially varying average reflectance map of the current scene, if the adjacency ranges R > 0.

- Step 6: (optional) empirical BRDF correction in areas of steep slopes or low illumination.

If the adjacency range R is selected as R=0 then steps 2 to 5 are omitted (Richter, 1997). An improved version of ATCOR3 with updated to accounts for scan angle effects and four geometric degrees of freedom: x, y, and z and scan angle. ATCOR4 is intended for wide field-of-view multispectral and hyperspectral imagery.

2.2.5. FLAASH algorithm

FLAASH is a radiative transfer model for atmospheric calibration and was developed by Spectral Sciences, Inc, under the sponsorship of the US Air Force Research Laboratory. It incorporates updated MODTRAN-based radiation transfer model into the code for modelling radiation transfer properties and includes a correction for pixel mixing due to scattering of reflected radiance from surroundings into the pixel. The features that are dealt with differently from other radiative transfer models are as follow:

- FLAASH uses a more recent version of MODTRAN with a newer spectral database.
- It uses a reflectance ratio-based method for visibility retrieval.
- FLAASH performs the MODTRAN calculations on-the-fly, supporting off-nadir geometries and all MODTRAN aerosol types.
- FLAASH provides compensation for the adjacency effect and automated wavelength calibration.
- The results from FLAASH and other radiative transfer model tend to be similar in dry, clear atmospheres but significant differences can occur under moist and hazy conditions.

FLAASH retrieves visibility by assuming a characteristic reflectance ratio for dark pixels in two wavelength band-passes. FLAASH uses a standard equation (2-4) for spectral radiance at a sensor pixel, L*, that applies to the solar wavelength range (thermal emission is neglected) and flat, Lambertian materials or their equivalents. The first term in Equation (2-4) corresponds to radiance that is reflected from the surface and travels directly into the sensor, while the second term corresponds to radiance from the surface that is scattered by the atmosphere into the sensor. These corrections have been reported to induce significant reflectance errors at short wavelengths, especially under hazy conditions and when strong contrasts occur among the materials in the scene (FLAASH user manual). The values of A, B, S and La are determined from MODTRAN4 calculations that use the viewing and solar angles and the mean surface elevation of the measurement, and assume a certain model atmosphere, aerosol type, and visible range. The values of A, B, S and La are strongly dependent on the water vapor column amount, which is generally not well known and may vary across the scene. To account for unknown and variable column water vapor, the MODTRAN4 calculations are looped over a series of different column amounts, and then selected wavelength channels of the image are analyzed to retrieve an estimated amount for each pixel. Specifically, radiance averages are gathered for two sets of channels: an “absorption” set centered at a water band (typically the 1130 nm band) and a “reference” set of channels taken from just outside the band. A two-dimensional look-up table for retrieving the water vapor from these radiances is constructed.

After the water retrieval is performed, Equation (2-4) is solved for the pixel surface reflectance in all of the sensor channels. The solution method involves computing a spatially averaged radiance image Le, from which the spatially averaged reflectance ρe is estimated using the approximate equation (2-5)

$$L_e \approx \left[\frac{(A+B)\rho_e}{1-\rho_e S} \right] + L_a$$

Equation 2-7

The spatial averaging is performed using a point-spread function that describes the relative contributions to the pixel radiance from points on the ground at different distances from the direct line of sight. For accurate results, cloud-containing pixels must be removed prior to the averaging. The cloudy pixels are found using a combination of brightness, band ratio, and water vapor tests.

The FLAASH model includes a method for retrieving an estimated aerosol/haze amount from selected "dark" land pixels in the scene. The method is based on observations by (Kaufman and Sendra, 1988), of a nearly fixed ratio between the reflectance for such pixels at 660 nm and 2100 nm. The aerosol amount is retrieved by iterating the Equation (2-4) and (2-5) calculations over a series of visible ranges, e.g., 17 km to 200 km. For each visible range, the scene-average 660 nm and 2100 nm reflectance values for the dark pixels are retrieved, and the "best" estimate of the visible range is interpolated by matching the ratio to the average ratio of ~0.45 that was observed.

The FLAASH visibility retrieval and atmospheric compensation can be sensitive to the method selected for the MODTRAN multiple scattering calculations. The Isaacs two-stream method, the discrete-ordinate radiative transfer (DISORT) method with eight streams, and a method called "DISORT scaling" which uses a small number of DISORT calculations to scale two-stream multiple scattering calculations, all gave very similar results (within 1 km in visibility) with the present data. If the FLAASH visibilities are in general range of 30-80 km using different retrieval methods and aerosol method, for such clear conditions, differences among the reflectance retrievals are small. If for the lower altitude lower-than-expected visibilities are obtained we can say that these low visibilities are the result of the aerosol being closer to the ground than assumed by MODTRAN (Rochford et al., 2005). Figure 2-4 shows a schematic process flow for FLAASH; spectral polishing for smoothening is an optional process to be selected by the user.

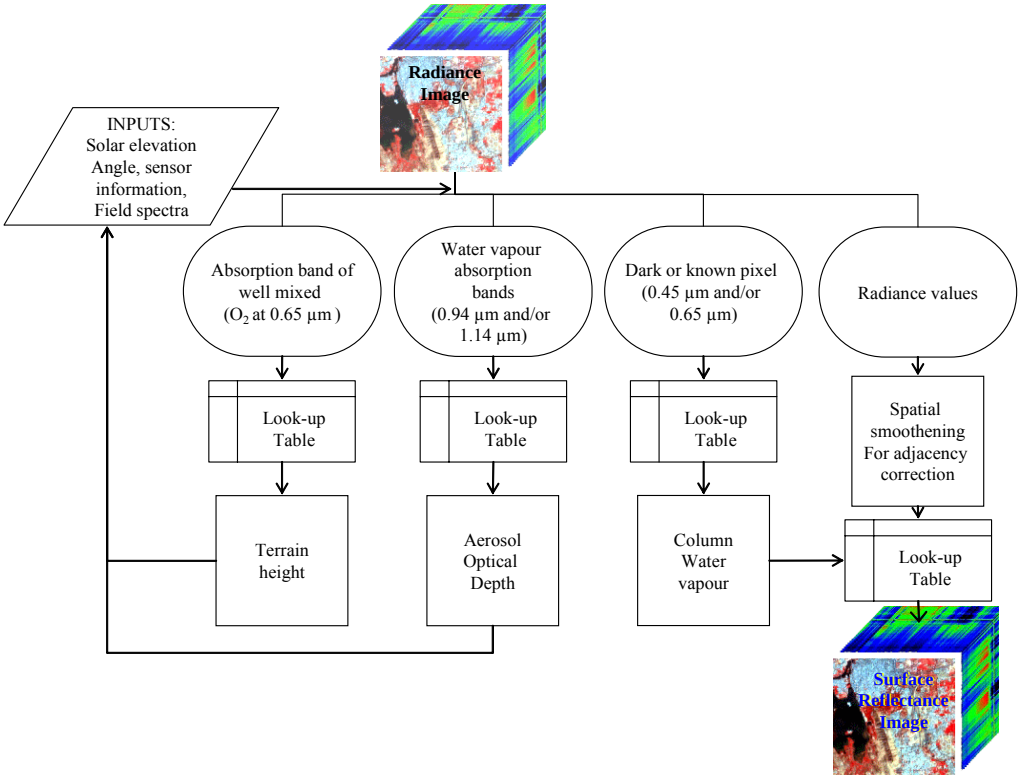

Figure 2-4 Schematic process flow for FLAASH showing basic steps involved in radiance to reflectance conversion (Griffin and Hsiao-hua, 2003)

2.2.6. Applications of atmospheric correction models

Several studies have been carried out in evolving methods for quantifying and compensating for the atmospheric perturbations on spectral imaging, resulting in a variety of atmospheric correction methods and models. Earlier studies on HyMap Hyperspectral dataset conclude that ATCOR model is suitable for the HyMap datasets, and reports 3% deviation between ground measured reflectance and HyMap retrieved reflectance values (Brunn et al., 2001). Comparative results between HATCH and ATREM program show that implementation of HATCH algorithm compensates for smile effect and performed better around strong water vapor absorption regions and overlapping regions for different gases but does not account for the adjacency effect. (Qu et al., 2003). Existing atmospheric correction models assumes variation in surface reflectance as a linear function of wavelength within gas absorption bands. This introduces residual spikes in the retrieved surface reflectance. Recent studies have proposed method for atmospheric correction using simulated annealing (ACSA) to enhance the atmospheric correction of hyperspectral images over dark surfaces (Marion et al., 2006). This proposed method smoothen the retrieved surface reflectance by adding spectral shape constraint in gas absorption bands.

Present study required understanding of atmospheric correction models and their inputs to convert Hyperion radiance image to reflectance image.

In this chapter the theory of atmospheric correction was reviewed. MODTRAN, the radiative transfer code used by ATCOR and FLAASH is also described. Next chapter describes the processing carried out on Hyperion datasets and describes the input parameters used during atmospheric correction.

3. Processing of Hyperspectral data

Processing of high dimensional hyperspectral data is a challenging task and the computational complexity is a result of vast data volume in numerous spectral bands. Since Hyperion sensor operates from a space platform with modest surface signal levels and a full column of atmosphere attenuating the signal, the data demand careful processing to manage sensor noise. The errors are said to be caused due to calibration differences in the detector array (Goodenough et al., 2003). The Hyperion dataset has to be corrected for abnormal pixels, striping and smiling prior to the atmospheric correction. Pre-processing of hyperspectral images is required not only for removing sensor errors during acquisition but also for display, band selection (to reduce the data dimensionality) and to reduce computational complexity. The following section discusses briefly about pre-processing steps carried out and atmospheric correction done on Hyperion dataset.

3.1. Pre level 1R processing

The Hyperion data is initially processed by the EO-1 product generation system (EPGS) and distributed at different processing levels. In the present study the radiometrically corrected level 1R product, which became effective from December 2001, has been used. The level 0 (raw) datasets were corrected for dark current (remove residual charge in the detectors), sensor bias effects and two specific artifacts known to affect the SWIR region to produce level1R product: (1) SWIR smearing, which is the leakage of signal from one pixel into the next readout pixel in the spectral direction, and (2) SWIR echo, which occurs when the signal from one image echos into a later pixel. The radiometric correction also involves applying sensor gain values that are based on post-launch calibration coefficients. The radiometrically corrected radiance image is then rescaled for DN output, e.g. for calibrating VNIR and SWIR bands the radiance image is multiplied by 40 and 80, respectively. A bad pixel mask is generated and is included in the header file of the level1R product. This mask is based on the bad pixel list that is defined during the pre-flight testing, with additional updates for the scene capture day. The values for bad detectors range from 0 to 4 (0 for normal data, 1 for saturated pixels, 2 for dead or zero value pixels, 3 for flat or constant value, and 4 for fill value that exceed calibration range). As the VNIR and SWIR region of Hyperion have been imaged by two sets of radiometers, the bands of VNIR and SWIR are realigned to form a single product. The alignment of SWIR with VNIR is carried out by shifting the SWIR bands cross track by -1 field-of-view (FOV) in X direction and +1 pixel down track in Y direction. This processed product is made available to the user as level1R product. The predicted signal to noise (SNR) ratio performance of Hyperion is in the range of 0-150 (Figure 3-1) (Pearlman et al., 2003).

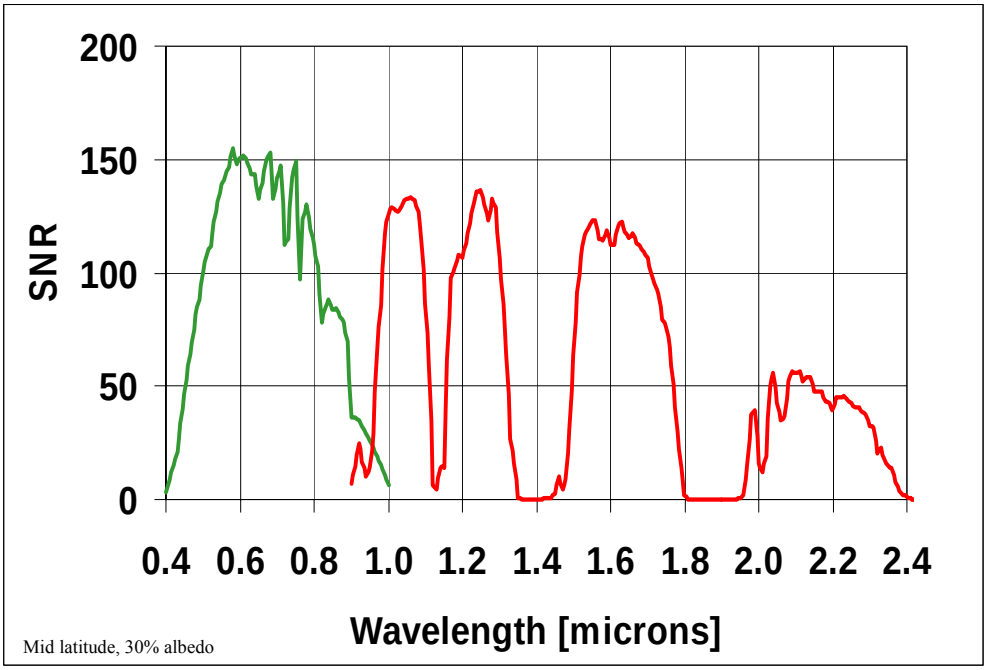

Figure 3-1 Hyperion signal to noise ratio performance prediction (Pearlman et al., 2003) (Source: http://edcsns17.cr.usgs.gov/EarthExplorer/)

3.1.1. Estimation of signal to noise ratio

To estimate signal-to-noise ratio of Hyperion datasets used in the present study homogeneous area method is used (Smith and Curran, 1998). The method is widely used and employed to make a quick estimate SNR. Based on variability of landcover small window of 2×2 and 4×4 sizes were used to estimate signal. Homogeneous areas were visually selected in vegetation, water and barren land. The signal (R_a) was estimated for each landcover by averaging the pixel responses in the window used (equation 3-1). The noise (R_{sd}) component was estimated by standard deviation of the pixel response within the window (equation 3-2).

$$R_a = \overline{X} \qquad \textbf{Equation 3-1}$$

$$R_{sd} = \sqrt{\frac{\sum_{1}^{n}(R_{ij} - R_a)^2}{n}} \qquad \textbf{Equation 3-2}$$

$$SNR = \frac{R_a}{R_{sd}} \qquad \textbf{Equation 3-3}$$

where
n = number of pixels in the homogeneous area
R_{ij} = Pixel Value (response) at ij location in the homogeneous window

A ratio of estimated signal and noise was calculated as SNR. The SNR in Udaipur image varies from 0 to 289 and for Spain dataset the SNR is estimated to be 0 to 121. SNR is highest in VNIR region for

both the datasets and range from 0 to 95 with maximum of 289 at 0.5 microns. Figure 3-2 shows the estimated SNR of Udaipur and Spain datasets. The estimated SNR for Udaipur and Spain datasets are in good agreement with the predicted SNR for Hyperion (Pearlman et al., 2003).

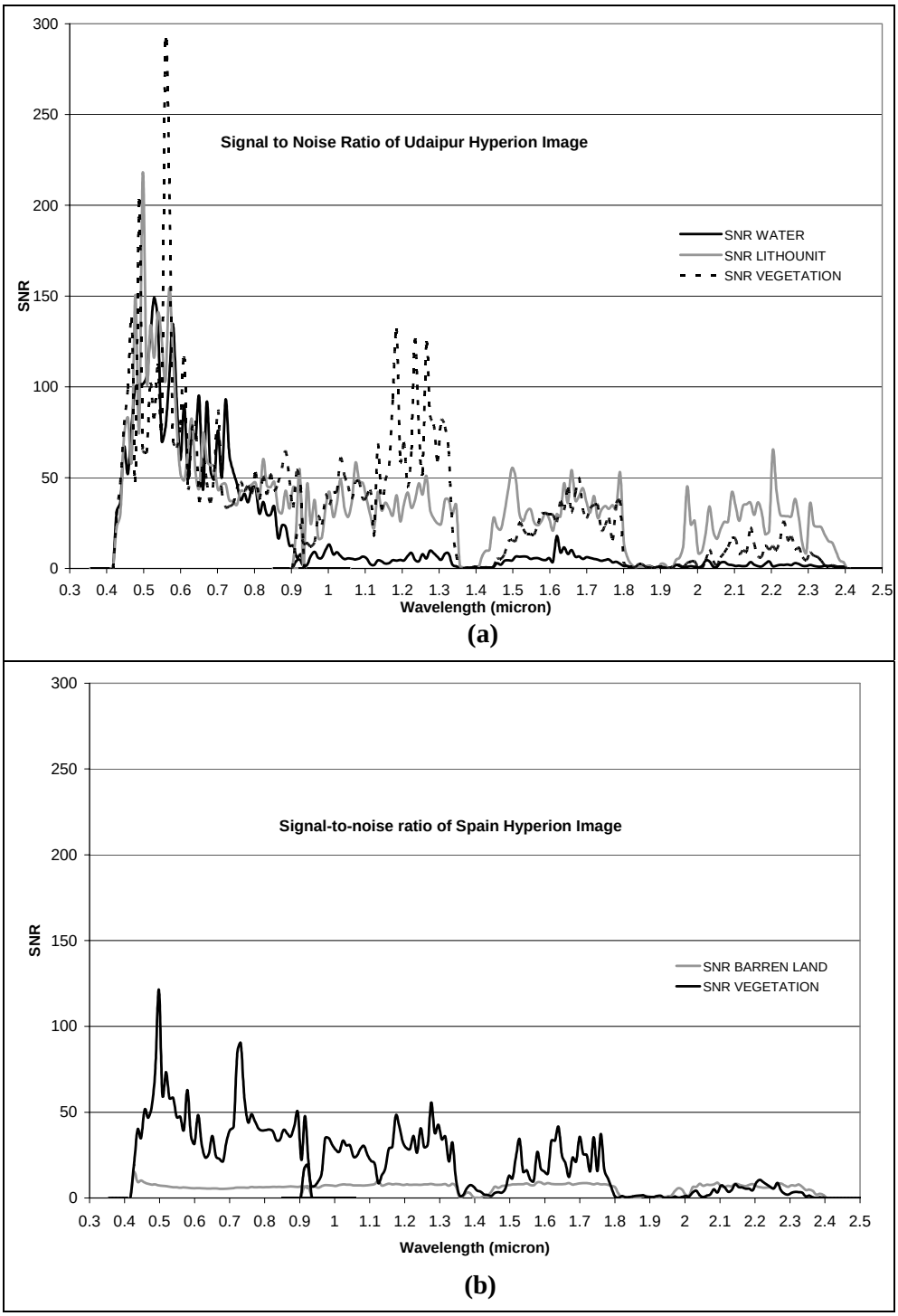

Figure 3-2 Signal-to-noise ratio in Hyperion datasets (a) Udaipur (b) Spain

3.2. Balancing vertical stripes in VNIR and SWIR region

In a pushbroom sensor, a poorly calibrated detector in either VNIR or SWIR arrays leaves high frequency errors ("vertical stripes") on the image bands. In Hyperion striping pixels have been classified in four categories: i) continuous with atypical DN values, ii) continuous with constant DN value, iii) intermittent with atypical DN values and iv) intermittent with lower DN values. The first two categories of stripes are the most extreme type as they contain very little or no valid data about the ground feature (Goodenough et al., 2003). In the level1R product these stripes are left unmodified, allowing the users to handle or replace the pixels as per the requirement. In order to facilitate extraction of calibrated spectra from Hyperion dataset it is significant to carefully balance for the striping in the dataset. In the present study a tool was developed to compensate for the striping by visually identifying bad columns and develop a filter to balancing for the bad columns.

3.2.1. Identification of bad columns

In order to compensate for striping in Hyperion datasets global and local de-striping approaches have been suggested. In the present study the bad columns were identified visually to avoid enforcing severe change in the spectra. A total of 36 bad columns were identified in 13 VNIR bands of Udaipur dataset and 48 bad columns in 16 VNIR bands of Spain dataset. SWIR bands were found devoid of visible stripes. Table 3-1 lists the detected bad columns in Udaipur and Spain datasets.

Table 3-1 Location of detected bad columns in level1R product

Band	Bad Column in Udaipur	Band	Bad columns in Spain
8	6, 68, 114	8	6, 68, 114, 125, 132, 168, 245, 246
9	6, 68, 114, 246	9	6, 68, 114, 148, 229, 246
10	6, 114, 119	10	6, 114, 199
11	6, 114, 119	11	6, 114, 119
12	114	12	114
13	114	13	114
14	114	14	114
15	114	15	114
16	114	16	114
54	13	27	47
55	13, 17, 20	28	47
56	8, 13, 17, 20, 32, 37, 39	39	117
57	8, 13, 17, 20, 33, 36, 38	54	13
		55	13, 17, 20, 32, 37, 39
		56	8, 13, 17, 20, 32, 37
		57	8, 13, 17, 20, 33, 37, 39

3.2.2. Balancing for bad columns

A bad column removal filter was developed to target the bad columns in each band. The bad columns were replaced by the 3×3 neighbourhood mean, without taking into account the bad column value. In order to implement this a 3×3 filter was designed (Figure 3-3) with positional values as (-1,1) =1, (-1,0) =1, (-1,-1) =1, (0,1) =0, (0,0) =0, (0,-1) =0, (1,1) =1, (1,0) =1 and (1,-1) =1. The filter runs on the bands identified as containing bad columns. The user interface allows the user to enter the band numbers that contain bad columns and column number of the specified band.

1	0	1
1	0	1
1	0	1

Figure 3-3 Filter design for local de-striping of Hyperion dataset

The values of the image data for sample (bad column) *i*, line *j*, and for band *k* (x_{ijk}) are modified to

$$\sum_{j=1}^{n}((x_{i-1,j,k})+(x_{i+1,j,k}))/2n \qquad \textbf{Equation 3-4}$$

where
i = identified bad column
n = total number of rows in the predefined filter

3.3. Smiling indicator and smiling correction

A low frequency error common to pushbroom sensors is reported in all Hyperion images and is referred to as the "smiling effect". Smiling refers to an across track wavelength shift from central wavelength. The wavelength shift is said to occur due to change in depression angle with the field position. The amount of shift is dependent on pixel position in the across track direction. The range of shift is reported to be varying between 2.6 and 3.5 nm. The maximum shift is recorded at pixel 256 at band 10 in VNIR region. The wavelength shift affects the diagnostic absorption features in the spectra. Thus influences the process of extraction of calibrated spectra from satellite platforms. The wavelength shift in Hyperion dataset can not be ignored and has to be compensated for (Goodenough et al., 2003).

3.3.1. Smiling indicator

The smiling effect is not obvious in individual bands. Indicators are therefore needed to identify and characterise the smiling in a given dataset. In order to observe the effect of smiling in the Hyperion datasets, two methods have been suggested. The first method was developed to take advantage of two strong Oxygen absorption regions at 752 nm and 772 nm. It is expected that, if no spectral shift has occurred in Hyperion sensor, Oxygen would be contributed equally to all the pixels in the two bands. Hence, a simple subtraction of the two bands should result in difference image with values nearing zero in across track direction. In the second method smiling becomes observable if the image is transformed into minimum noise fraction (MNF) space (Goodenough et al., 2003). The forward MNF technique responds to interaction between the spatial structure of the data and that of noise when the noise has strong spatial structure (Datt et al., 2003). Images with significant smile display a brightness gradient in the first eigenvalue image, MNF1.The two methods were applied to the Udaipur and Spain datasets and significant smiling was observed. To implement the methods the two datasets were spectrally subset in VNIR and SWIR regions.
The oxygen absorption regions at band 40 (752nm) and band 42 (772nm) were subtracted to get the difference image. Examination of across track profile of difference image indicates a rise in gradient in values from 0 to 240, indicating significant smile in the two datasets (Figure 3-4).

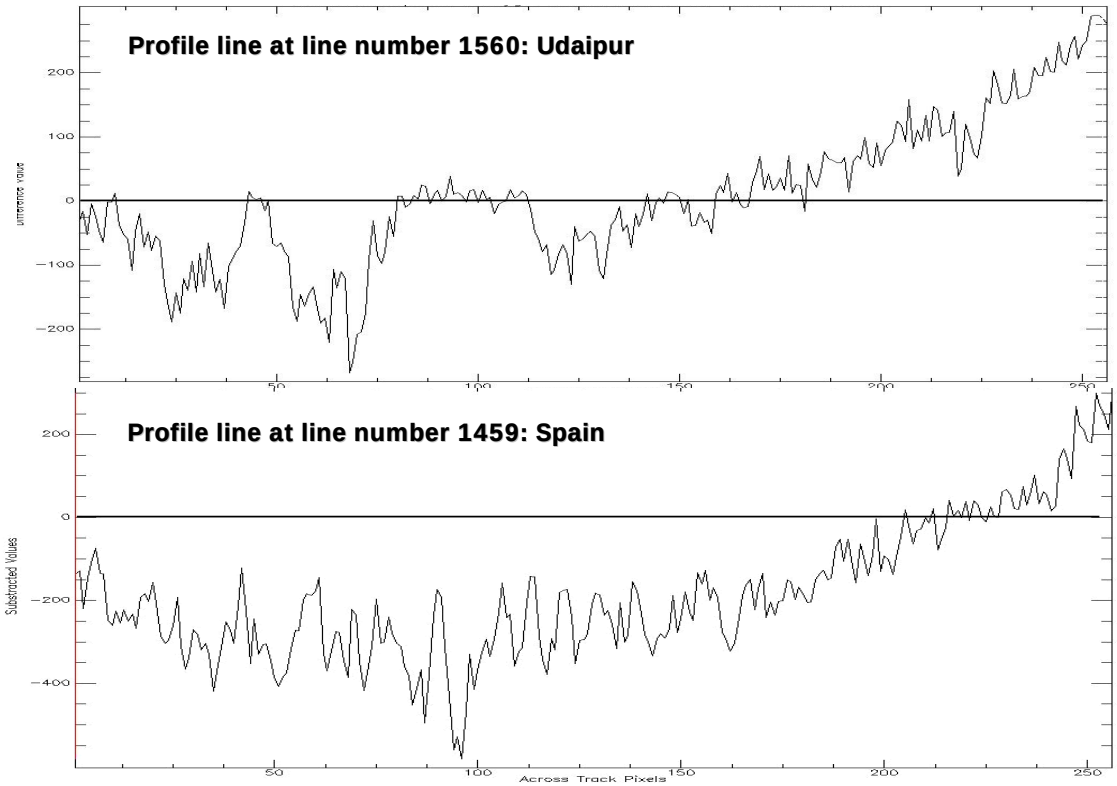

Figure 3-4 Across track profile of Oxygen absorption difference images of Level 1R product Udaipur and Spain

The spectral images of VNIR region and SWIR region were then subjected to forward MNF transformation separately. Examination of MNF 1 for VNIR exhibits a strong brightness gradient and no such brightness gradient was seen in MNF 1 for SWIR (Figure 3-5).

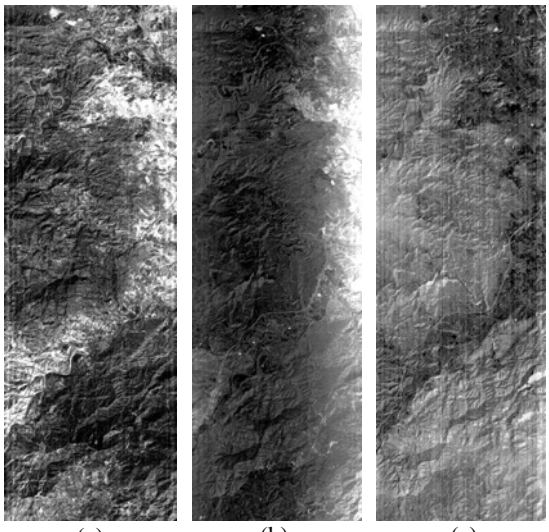

(a) (b) (c)

Figure 3-5 (a) Band 8. (b) Brightness gradient in MNF1 of VNIR. (c) Brightness gradient in MNF1 of SWIR in Spain dataset.

3.3.2. Smiling correction

Correction for smiling is still a topic of research, much effort in the removal are towards use of moving linear fitting and interpolation considering calibrated ground spectra as reference and forward MNF transformation (Goodenough et al., 2003). Forward MNF transformation is a linear transformation related to Principal Component that sorts the data according to signal-to-noise ratio. It determines the inherent data dimensionality and segregates noise in the data and reduces the computational requirements for subsequent processing. It partitions the data space into two parts: one associated with large eigenvalues and coherent eigenimages, and a second with near unity eigenvalues and noise dominated images. By using only the coherent portions in subsequent processing, the noise is separated from the data, thus improving spectral processing results. A comparison of results obtained from these techniques reveals that linear fitting performed better than the techniques based on MNF transformation. All the techniques remove smiling effect in the spectra but also create false spectra (artifacts) in Hyperion dataset (Goodenough et al., 2003). Removal of smiling would require quantifying wavelength shift, and calibration of wavelength by modelling added with accurate knowledge of atmospheric constituents and surface conditions (Felde et al., 2003). Thus the need for real time collection of ground spectra and atmospheric measurements limits the use of these methods to remove smiling for the dataset.

Recent trends in research to remove smiling have been coupled with atmospheric correction procedure. These techniques bypass the requirement of knowledge about atmosphere and are insensitive to the surface reflectance. A strong oxygen absorption feature at 760 nm is utilized to quantify the wavelength shift in the dataset. A normalized optical depth derivative (NODD) algorithm convolutes the sensor measured radiance spectrum to model the correction factor in the wavelength (Felde et al., 2003). This algorithm is implemented in the FLAASH atmospheric correction model in ENVI 4.1. This method was used in the present study to quantify spectral shift and remove smiling in the Hyperion datasets. A more recent effort to determinate the shift is made by an iterative optimization procedure that minimizes the difference between a shifted spectrum and the corresponding smoothed reference spectrum, the spectral shift being the variable of the inversion. The algorithm calculates an average spectrum from all the pixels in the same along-track line, to have a representative sampling of the sensor performance in the across-track direction (Guanter et al., 2006).

A minimum of wavelength shift of -16.71008 nm at band 155 is observed in the SWIR region and maximum of 0.81003 nm shift at bands 8-13 is estimated in the VNIR region of Spain dataset (Figure 3-6 (a) and (b)), whereas the wavelength shift varies between 0.66101 nm at band 31 in VNIR and 1.67004 nm at band 153 in SWIR region of Udiapur dataset (Figure 3-6(c) and (d)). This estimated shift for each band is applied to the respective datasets during the atmospheric correction procedure.

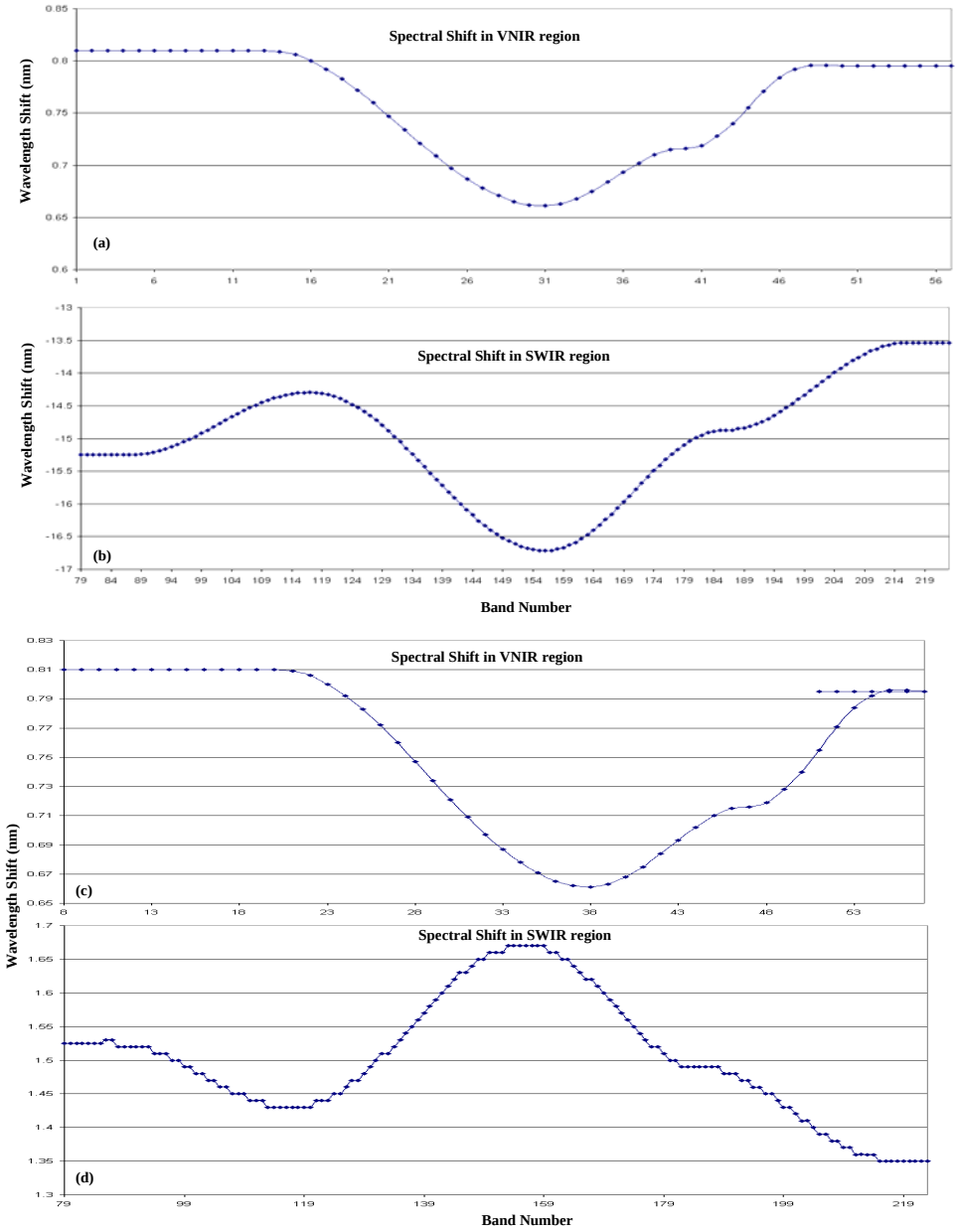

Figure 3-6 (a) Wavelength shift in VNIR region of Spain dataset. (b) Wavelength shift in SWIR region of Spain dataset. (c) Wavelength shift in VNIR region of Udaipur dataset. (d) Wavelength shift in SWIR region of Udaipur dataset.

3.4. Preparation of input data and selection criterion

The input parameters required for ATCOR2 and FLAASH are to be computed before the image is subjected to atmospheric correction. The data description of Hyperion collected during the order placed is placed at Table 3-2.

Table 3-2 Data description attributes of Hyperion – Udaipur and Spain (Source: http://edcsns17.cr.usgs.gov/EarthExplorer/)

Dataset Attribute	Udaipur dataset	Spain dataset
Entity ID	EO1H1480432004019110PZSGS01	EO1H1990342003037110PZSGS01
Acquisition Date	2004/01/19 (January)	2003/02/06 (February)
NW Corner	24'54'47'N, 73'44'13'E	37'19'56'N, 1'57'52'W
NE Corner	24'53'53'N, 73'48'39'E	37'18'59'N, 1'52'48'W
SW Corner	24'07'49'N, 73'32'52'E	36'36'50'N, 2'10'26'W
SE Corner	24'06'55'N, 73'37'16'E	36'35'53'N, 2'05'25'W
Image Cloud Cover	0 to 9% Cloud Cover	0 to 9% Cloud Cover
Receiving Station	SGS	SGS
Scene Start Time	2004:019:05:22:10.546	2003:037:10:33:42.149
Scene Stop Time	2004:019:05:22:24.546	2003:037:10:33:55.149
Date Entered	2004/01/29 January	2003/02/18 February
Target Path	148	199
Target Row	43	34
Orbit Path	148	199
Sun Azimuth	145.987318	149.028495
Sun Elevation	37.214824	31.487335
Satellite Inclination	98.24	98.23
Orbit Row	43	34
Look Angle	-0.4642	-1.6888
Browse Available	Y	Y

The parameters required from the user to run the two models successfully are sensor specific and specific to ground situation. Table 3-3 shows the list of input parameters required by the two atmospheric correction models. Selection of the input parameters has a direct bearing on the output of the atmospheric correction models. The parameters selected for atmospheric correction of the datasets is discussed here based on the user manual of the ATCOR and FLAASH.

Table 3-3 Input parameters for ATCOR2 and FLAASH

ATCOR2 parameters	FLAASH parameters
Sensor type	Sensor type
Pixel size	Pixel size
Ground elevation	Ground elevation
Solar Zenith angle	Scene centre Latitude/Longitude
Visibility	Sensor altitude
Flight date	Visibility
Atmospheric file	Flight date & flight time
Adjacency range	Atmospheric model
Zones	Aerosol model
Region for water vapour	Water vapour retrieval
Water vapour absorption	Spectral polishing
Haze removal	Wavelength calibration
Shadow removal	**Advanced parameters**

ATCOR2 parameters	FLAASH parameters
Reflectance scale factor	Output reflectance scale factor
Value added product	MODTRAN resolution
Index map	MODTRAN multi scattering model

3.4.1. Sensor type

The option of selecting sensor type is provided to the user as both ATCOR2 and FLAASH are used for wide range of sensors. Sensor type, for the present study is selected as Hyperion.

3.4.2. Pixel size

The Hyperion data ordered to EPGS was specified as nadir looking product. Therefore the pixel size selected is 30 meters, as per the data description of Hyperion.

3.4.3. Ground elevation

Ground elevation input required by ATCOR2 and FLAASH is an average elevation of the imaged terrain. For Udaipur the average elevation of the imaged terrain was taken as 0.6 km above MSL (Roy et al., 1998). For Spain dataset average elevation was calculated as 0.44 km above MSL based on the foot print of Hyperion image on ASTER digital elevation model provided by ITC.

3.4.4. Solar zenith angle/ Flight date and time

Solar zenith angle at time of the satellite pass is provided by the EPGS in the product description. For Udaipur the solar zenith angle is 37.214824 degrees and for Spain the solar zenith angle is 31.487335 degrees. Flight date and time for Udaipur and Spain dataset are selected as per the data description of Hyperion (Table 3-2).

3.4.5. Scene centre latitude and longitude

The scene centre latitude and longitude is provided in the header file of the dataset.

3.4.6. Sensor altitude

Tracking information for EO-1 is collected by NASA, but the ephemeris parameters are not published. During atmospheric correction of Hyperion datasets knowledge of the EO-1 satellite heading and view angles are essential in order to establish the sun-sensor geometry at the location of scene capture. To compute the nominal parameters related to the sensor geometry on the surface, the orbital inclination of the satellite, its angular velocity and the radius of the orbit and some earth surface parameters are required. The calculation method is simply a function of the latitude. The satellite information is computed assuming the orbit is circular but that the earth is a spheroid. The results are approximate but are useful to provide starting choices in atmospheric correction models (Jupp et al., 2004). Some of the known parameters for Hyperion and earth parameters required to compute satellite height are displayed in Table 3-4.

Table 3-4 Satellite, Earth and sensor parameters (Jupp et al., 2004).

Parameter	Symbol	Value
Geodetic latitude	Φ_0	Various
Spheroid semi-major axis	a (m)	6378137
Spheroid eccentricity	e^2	0.00669438
Earth rotation at equator	ω_0 (rad sec^{-1})	7.2722052E-05

Parameter	Symbol	Value
Radius of orbit	R (m)	7.077773536E+06
Orbital inclination	*oi* (degrees)	98.225
Satellite angular velocity	V_0 (rad sec^{-1})	0.001059
Sensor Field of View (degrees)	FOV (degrees)	0.624
Pixels/Line	PL	256
Frame Rate	FR (Hz)	223.4
Fixed Roll (degrees)	r (degrees)	5
Slit angle along track	Ifovy (degrees)	0.002438

The altitude of the satellite above ground at a location is given by:

$$Alt = R - X_n \qquad \textbf{Equation 3-5}$$

$$Xn = N(1 - e^2(2 - e^2)\sin^2 \Phi_0)^{1/2} \qquad \textbf{Equation 3-6}$$

$$N = a/(1 - e^2)\sin^2 \Phi_0) \qquad \textbf{Equation 3-7}$$

Where
Alt = Altitude of the satellite
R= Radius of orbit
Xn = Distance from the surface to the centre of the spheroid
e = Spheroid eccentricity
Φ_0 = Scene centre latitude
a = Spheroid semi-major axis
Using the equations 3-1, 3-2 and 3-3 (Jupp et al., 2004) Hyperion height over Udaipur and Spain was found to be 703.3166 and 707.3276 km respectively. The calculated heights were used as input to the FLAASH and ATCOR2 atmospheric correction models.

3.4.7. Visibility

Visibility input for the atmospheric correction models was inferred from the aerosol optical thickness (AOT) and water vapour measurements made during January 2004. The study indicates January 2004 month low values of water vapour (cm) and AOT (unit less quantity) that directly influence the visibility. The observations made until 2002 were validated by TOMS satellite data (Pandey and Vyas, 2004). The data pertaining to January 2004 provided by the author show a range of AOT values between 0.097 to 0.704 (Figure 3-7) and water vapour values between 0.3 to 1.1 cms (Dasora et al., 2005).

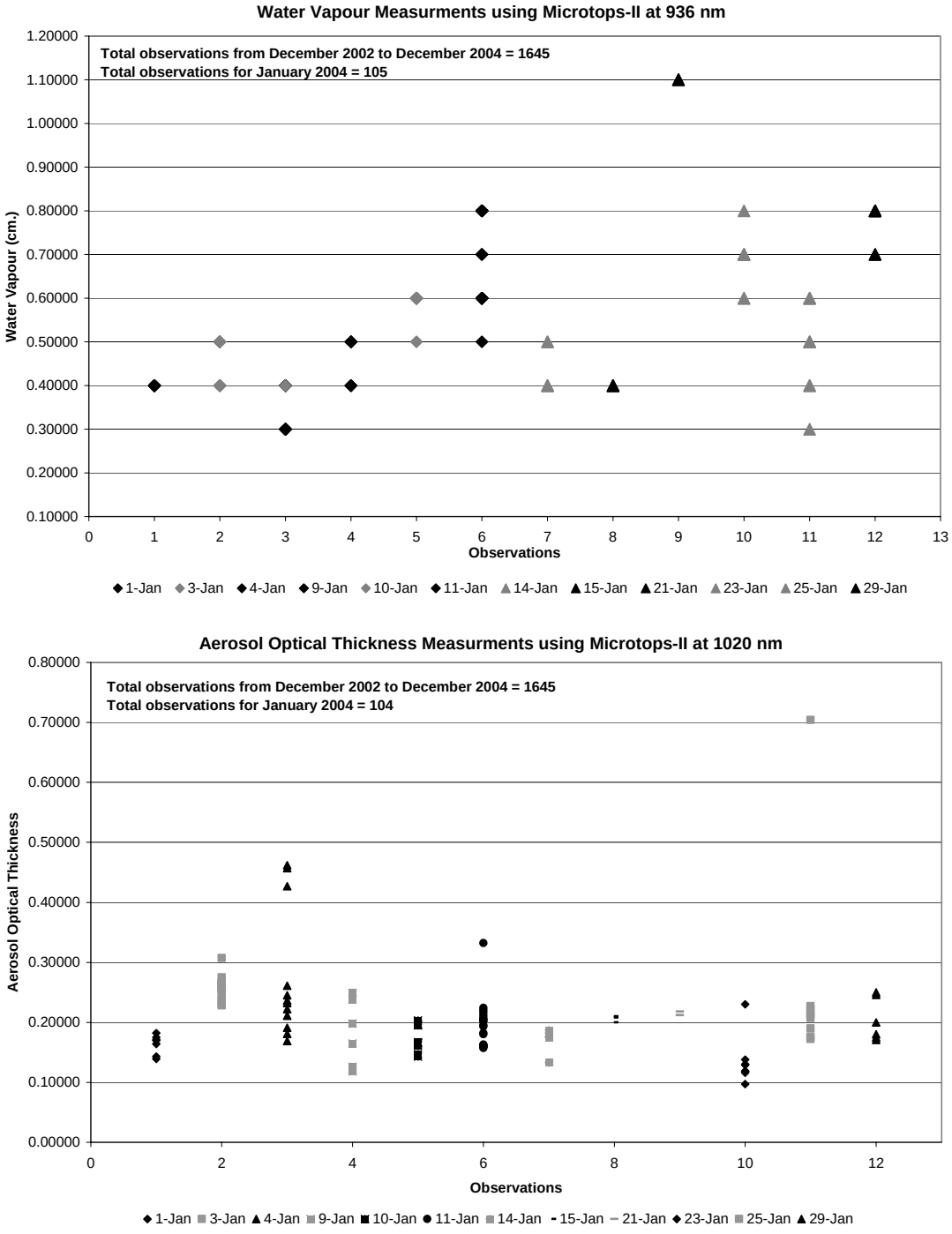

Figure 3-7 Observation of Water Vapour and Aerosol Optical Thickness over Udaipur

The visibility selected for Udaipur was inferred as "clear" in the range of 40 km.

3.4.8. Flight date and Flight time

Flight date and time is provided with the description of Hyperion (Table 3-2).

3.4.9. Atmospheric model

The user has to make a choice, based on the geographic location of the scene to atmospherically correct the image. FLAASH supports six atmosphere types based on a seasonal-latitude surface temperature MODTRAN modelled atmospheres (Table 3-5).

Table 3-5 Column water vapor amounts and surface temperatures for the MODTRAN model atmospheres (Source: FLAASH user guide).

Model Atmosphere	Water Vapour (std atm-cm)	Water Vapour (g/cm2)	Surface Air Temperature
Sub-Arctic Winter (SAW)	518	0.42	-16 °C or 3 °F
Mid-Latitude Winter (MLW)	1060	0.85	-1 °C or 30 °F
U.S. Standard (US)	1762	1.42	15 °C or 59 °F
Sub-Arctic Summer (SAS)	2589	2.08	14 °C or 57 °F
Mid-Latitude Summer (MLS)	3636	2.92	21 °C or 70 °F
Tropical (T)	5119	4.11	27 °C or 80 °F

Selection of MODTRAN model atmospheres is based on latitudinal/seasonal dependence of surface temperature of the study area. To help the user to select a model latitudinal ranges (0 to 80ºN and 0 to -80º S) and month of scene capture FLAASH recommends the use of a specific model for use. Based on the location of Udaipur 24º36′ N latitude for a January scene "Tropical" model was selected. For Spain Rodalquiar location is at 52.9″ N latitude for February "Mid-latitude Summer" was selected.

3.4.10. Aerosol model/ atmospheric file

ATCOR supports four basic aerosol types: rural, urban, maritime, and desert. The user has to make a choice, based on the geographic location. Rural is recommended for areas with visibility greater 40 km. For FLAASH the Rural model represents the aerosol found in areas not strongly affected by urban or industrial sources. For both Udaipur and Spain datasets "Rural" aerosol model was selected.

3.4.11. Water vapor retrieval

ATCOR and FLAASH include a method for retrieving the water amount for each pixel. The selection of wavelength at which the water retrieval is to be carried out is based on the availability of bands in the dataset to be atmospherically corrected. As Hyperion has bands in 356–2577 nm range the recommended 1135 nm is used for water retrieval for both Udaipur and Spain datasets.

3.4.12. Adjacency range and zone

In order to accommodate for the adjacency effect, due to which radiances of adjacent fields of different reflectance. ATCOR allows adjacency range of 0.5 to 1 km. As the two dataset in use belong to a heterogeneous area an adjacency range of 0.5 km is selected with weight factor of 1. This same effect is treated as "adjacency correction" toggled to yes in advanced setting parameters of FLAASH. Three multiscatter models are available in FLAASH Isaacs, Scaled DISORT, and DISORT. The recommended Scaled DISORT with 8 streams (signifying 8 directional adjacency) is selected for the present study.

3.4.13. Reflectance scale factor

In order to scale the output reflectance image from floating-point into 2-byte integer data space the recommended scale factor of 10,000 is used for Udaipur and Spain datasets in ATCOR and FLAASH.

3.4.14. Additional optional parameters

More additional parameters available in ATCOR are Haze removal, Shadow removal, Value added product, and Index map. The scene of the study area is not seen to be affected by haze or shadows, these options were not utilized during atmospheric correction.

3.4.15. Wavelength calibration

The wavelength re-calibration was applied as in FLAASH, where as no such option is available in ATCOR2.

3.5. Band positioning and absorbtion

When light interacts with a mineral or rock, light of certain wavelengths is preferentially absorbed while at other wavelengths it is transmitted or reflected from the substance. Reflectance is defined as the ratio of the intensity of light reflected from a sample to the intensity of the light incident on it. Electronic and charge transfer processes e.g., changes in energy states of electrons bound to atoms or molecules associated with transition metal ions such as Fe, Ti, Cr, etc., determine largely the position of diagnostic absorption features in the visible- and near-infrared wavelength region of the spectra of minerals (Van der Meer and De Jong, 2003). Band positioning and absorption analysis have been successfully attempted in Airborne Visible and Infrared Imaging Spectrometer (AVIRIS) data for surface mineralogical information extraction (Van der Meer, 2004). This technique has been adopted in the present study for Udaipur Hyperion dataset.

The absorption in a spectrum has two components, continuum and the absorption feature itself. The continuum is defined as a piecewise-linear envelope enclosing the radiance spectra.The continuum or background is the over all albedo of the reflectance curve. Removing the continuum effectively normalizes the spectra (Van der Meer, 2004). The modified spectra exhibit a flat background, but absorption features are retained. The flat background means no absorption feature (Figure 3-8).

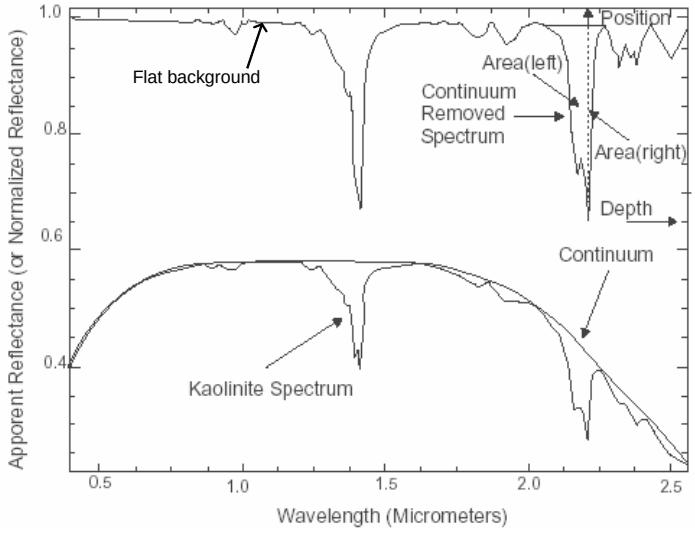

Figure 3-8 Continuum and absorption parameters (Van der Meer, 2004)

To carry out band absorption analysis three parameters (i) absorption band position, (ii) absorption depth and (iii) absorption band asymmetry have been proposed (Van der Meer, 2004). Figure 3-9 shows a schematic view of parameters used in the derivation of absorption characteristics. These parameters are derived from continuum removed spectra. Absorption band position is defined as the

minimum reflectance value over the wavelength range. Absorption band depth is calculated relative to the continuum as

$$D = 1 - \frac{R_b}{R_c}$$ **Equation 3-8**

Where Rb is the reflectance at the band bottom and Rc is the reflectance of the continuum at the same wavelength. Estimation of absorption depth position provides useful information about the absorption feature that could be attribute to a mineral of interest. Absorption band asymmetry describes the shape of the absorption feature. The asymmetry factor is defined as

$$S = \frac{A_{left}}{A_{right}}$$ **Equation 3-9**

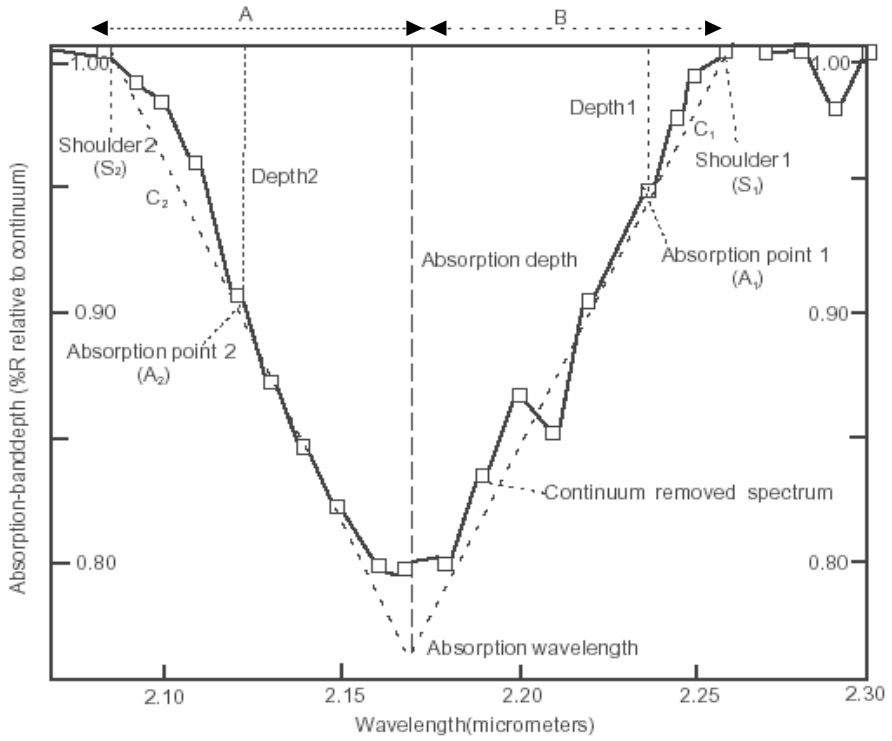

Figure 3-9 Schematic representation of parameters used derive absorption characteristics (Van der Meer, 2004)

The values of asymmetry range from 0 to infinity. Asymmetry value of 1 for symmetrical shape, value range greater than 1 for skewed shape towards longer wavelength and value range between 0 and 1 for skew towards shorter wavelength.

The absorption parameter definitions assume spectra to be continuous. To mathematically implement the derivation of these parameters (equation 3-8 and 3-9) a linear interpolation is suggested for hyperspectral discrete spectral bands. The inputs required are identification of short wavelength shoulder (S2), longer wavelength shoulder (S1), Short wavelength absorption band location (A2) and long wavelength absorption location (A1). A linear relationship is established using four points to calculate coefficients C1 and C2 (equation 3-8 and 3-9) (Van der Meer, 2004).

$$C_1 = \sqrt{\left[(depth)^2 + (S_1 - A_1)^2\right]} \qquad \textbf{Equation 3-10}$$

and

$$C_2 = \sqrt{\left[(depth_2)^2 + (S_2 - A_2)^2\right]} \qquad \textbf{Equation 3-11}$$

The absorption wavelength was mathematically be expressed as equation 3-12 (Van der Meer, 2004).

$$Absorption\_wavelength = -\left[\frac{C_1}{C_1 + C_2} \times (A_1 - A_2)\right] + A_1 \qquad \textbf{Equation 3-12}$$

The associated absorption-band depth was then derived using equation 3-14(Van der Meer, 2004).

$$absorption\_depth = \left[\frac{S_s - absorption\_wavelength}{S_s - A_s}\right] \times depth_1 \qquad \textbf{Equation 3-13}$$

The asymmetry factor of the absorption feature was calculated using equation 3-16 (Van der Meer, 2004).

Asymmetry = (absorption_wavelength-S_2) – (S1 – absorption_wavelength) **Equation 3-14**

The derivation of the band positioning and absorption for Udaipur dataset were performed using ENVI-IDL script developed during the study. The parameters S_1, S_2, A_1, and A_2 required for the band positioning and absorption analysis were derived from the Udaipur dataset for quartzite rock. The criteria for considering quartzite rock as well as the derivation of the asymmetry and absorption depth parameters are discussed in section 5.6.

The two datasets of Udaipur and Spain were processed as discussed in this chapter and used as inputs to two atmospheric correction model ATCOR2 and FLAASH to derive scaled reflectance image. The chapter also describes the processing required before the image is subjected to atmospheric correction. Chapter 4 cover the pre-field and data collected during the field work for Udaipur. The outputs of the two atmospheric correction models are discussed in Chapter 5 analysis and results.

4. Field Investigations

Hyperspectral remote sensing data allow interpretation of land cover types like soil, geology, vegetation and water, etc. without significant field verification. Ground truth data collection becomes necessary so as to be deterministic in vegetative health, specific rock type or mineral. The purpose of the present study is to gain knowledge about atmospheric conditions and target calibration (rock types). In order to address one of the objectives to compare the atmospherically corrected image spectra to that of field spectra, field work was necessary. A field visit was carried out from November 21st to 24th 2006. This chapter discusses the procedure followed for data collection and sampling plan adopted.

4.1. Pre-field

Pre-fieldwork preparation is an important component of a field campaign. The following section discusses the steps adopted before the field visit.

4.1.1. Rectification of image

Georefrencing of Udaipur Hyperion image was carried out using the orthorectified ETM+ dataset in UTM/WGS84 datum, zone 43N. The RMS error achieved during georeferencing was 0.421 pixels. In order to avoid spectral interpolation, nearest neighbourhood resampling method was used (Janssen et al., 2004).

4.1.2. Preparation of database

In order to facilitate selection of sample points in the study area and field navigation, vector data sets of Geological map, road network and village locations were generated.

4.1.3. Sampling plan

The spectral signature within a pixel of the image consists of an average of the reflectances of all materials within that pixel. At Hyperion's spatial resolution (15 x 15 meter) the spectral response for a geological sample will consist of a combination of spectra of all vegetation types and the soil, ground litter, etc., within the picture element.

Prior to field work a random stratified sampling strategy was employed to decide on the location of sample points. Comparatively large and homogenous lithological outcrops in the study area were selected on the basis of existing geological map prepared by Geological survey of India and updated by (Roy et al., 1998). The other factors taken into consideration are the local terrain elevation the slope (to avoid shadow areas on the image), and accessibility to the area keeping in mind the fact that the data collection would have to be done in a limited period of time. For the present study the main lithological classes taken into consideration are the exposures of Debri and Delwara group of rocks, know to be widely exposed.

Based on the criteria mentioned above 32 sampling points were selected in the study area. The locations of all the selected sampling points, georefrenced Hyperion Image, road network, and village locations were ported on ArcPad to facilitate Arc Pad 6.0.3 based Mobile GPS mounted on palm top

for field use. Figure 4-1 shows the distribution of field sampling points on geological map of the study area.

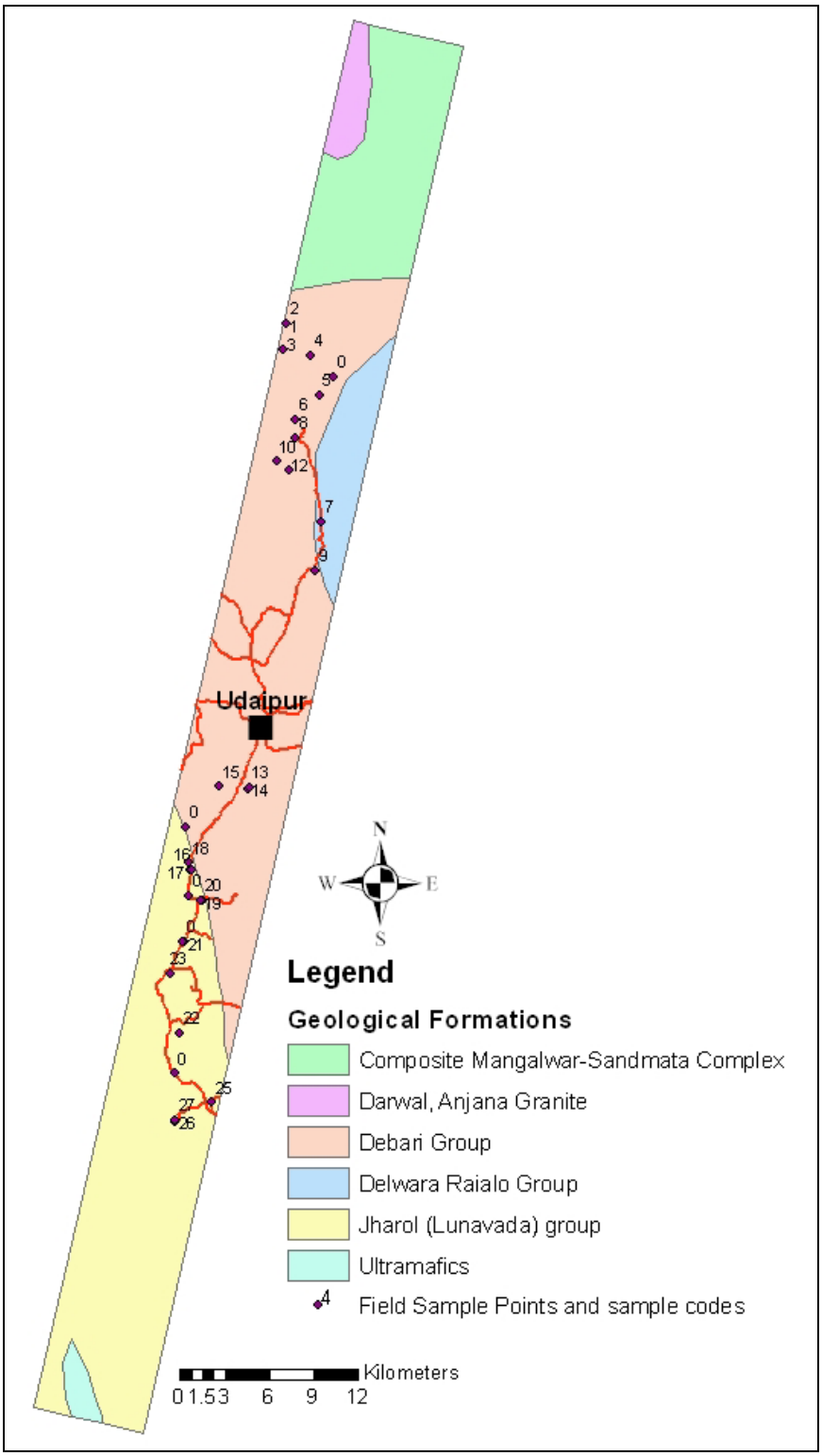

Figure 4-1 Distribution of sample points on published Geological map of Geological Survey of India (Roy et al., 1998) showing field sampling points with sample codes (0 sample code were not accessible points)

The rock samples were identified in the field and the image locations were recorded in the field on ArcPad. Table 4-1 shows a brief description of the samples collected in the field.

Table 4-1 Brief description of Rock sample collected with corresponding field locations.

Sample code	Field location in UTM coordinates		Rock type
	Easting	Northing	
1	369700.33	2744947.16	Chlorite Schist
2	369656.95	2744965.19	Biotite Chlorite Schist
3	369484.09	2743138.45	Chlorite Schists with carbonate bands
4	371323.84	2742768.33	Quartzite
6	371871.04	2740153.14	Quartzite
7	370295.41	2738487.48	Quartzite
8	370293.09	2737232.19	Chlorite Schist
9	372026.28	2731618.40	Quartzite
12	369001.19	2735653.65	Quartzite
13	369818.04	2735084.92	Quartzite

4.2. General field Observations

In order to relate the ground feature to the Hyperion image, some background about the area was drawn from the field observation and available literature.

4.2.1. Physiography

Physiographically, Udaipur has undulating and rocky topography with high and low hills. The city is surrounded by the hills of Aravalli ranges of various heights. The important hills within the area are:
Northern hills: Nimach Mata Hill (767.3 m), Bhuwana Hill (708.7 m).
Southern hills: Balicha Hill (636.2 m), Odi Hill (688.45 m).
Eastern hills: Eklingpura Hill (683.4 m), Chorbavari Hill (769 m).
Western hills: Thoria Hill (756.42 m), Machhala Magra (753 .55m), Sajjangarh Hill (936.82 m).
Besides these, the area also has depressions in form of lakes like Pichola, Fatehsagar, Rangsagar, Swaroopsagar and Goverdhanvilas-ka-Talab etc. The River Ayar flows in northwest to southeast direction.

4.2.2. Climatic Condition

Udaipur has a semi-arid climate, which prevails over most of the year. It has a hot dry summer and bracing cold winter. The cold season is generally from November to February and is followed by the summer season from March to June. The southwest monsoon follows from last week of June to the mid September. In the area, 90% of the total rainfall occurs during June to September period. July and August are the wettest months of monsoon. The average annual rainfall for the area is 640 mm and average number of rainy days is 42. The annual rainfall for the last 100 years ranges between 300 mm (1936) to 1133 mm (1973). January month in Udaipur has generally been a non-rainy month. Figure 4-2 shows rainfall pattern of last 30 years for the month of January. The annual potential evapo-transpiration values in the area ranges from 1300 mm to 1400 mm.

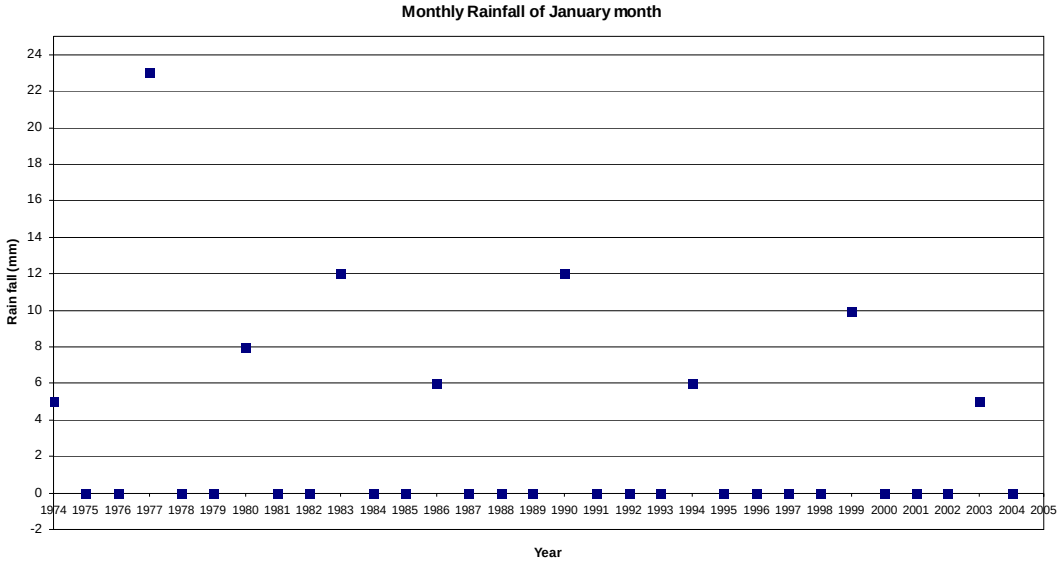

Figure 4-2 Rainfall pattern for the month of January from 1974 to 2005 (source: District administrative office, Udaipur)

4.2.3. Drainage pattern and drainage geometry

The drainage pattern in the area shows an angular type of drainage wherein the streams developed as per the structure and joint pattern of the rock type and alteration of hard and soft beds. However, on average the area is characterized by low to moderate level runoff conditions.

4.2.4. Existing land use

An estimated distribution of existing land use categories is as follows:

1. Forest land use including land under trees.
2. Agricultural land use including cropland, orchards.
3. Wasteland, uncultivable land.
4. Surface water bodies including lakes, streams.

4.2.5. Slope

The average slope data analysis reveals that in Udaipur area the average slope angle varies between 00 to as high as 17°. The slope Uniform slope is noted in N-E direction near Bari and Nimachmata area. Concave slopes are observed near Sajjangarh, in western side of area. Convex slope occurs at the Machhla Magra and Bhuwana Hills sites. In the rest of the elevated area i.e. to the southwest sites and northwest sites the slope are undulated type.

4.2.6. Geological Set-up

The geological setting of Udaipur area is not only unique in the state but also shows wide complexity. It is considered as one of the “type area” of the Aravalli Supergroup of rock. The study area broadly has two main stratigraphic units i.e. rocks of Aravalli Supergroup and pre-Aravalli Formations. Aravalli Supergroup of rocks around Udaipur city shows a high degree of structural complexity and polyphase deformation history. Table 4-2 shows general geological succession of the Rajasthan state. The major lithounits in the study area are composed of Quartzites, Chlorite schists, Arkose and Dolomite. Based on the homogeneity of the lithounits observed on the field, the pre-selected sample points had to be moved and the new locations were recorded.

Table 4-2 General Geological Succession of Precambrian Formation of Rajasthan (after Heron, 1953) (source: Department of Geology, MLS University, Udaipur)

	Recent & Sub recent	Alluvium and blown sand	
	Vindhyan System	Sandstone, limestone & boulders	Dolerite and basalt (age uncertain)
	Malani Rhyolites	Rhyolite, tuffs	Granite, ultrabasic rock Erinpura granite, pergmatite, aplite Epidiorite and hornblende schist
Delhi System	Ajabgarh Series	Upper phyllite Limestone Biotitic limestone and calc-schist Phyllites, biotite schist and composite gneiss	
	Alwar Series	Quartzites Arkose, grit and conglomerates	
	Raialo Series	Garnetiferous biotite schist Limestone (marble) Local basal grit	Aploganite, epidiorites and hornblende schists, ultrabasics
Aravali System		Impure limestone, quartzites, phyllites, biotite-schist, composite gneiss	
		Quartzites, grits and local soda-syenites, conglomerate	
		Local amygdaloids and tuffs	
	Banded Gneissic Complex (BGC)	Schists, gneisses and composite gneiss	Pegmatites, granite, aplites and basic rocks
		Quartzites	

4.3. Field Spectra collection

The field spec data are used as one of the inputs to correct the hyperspectral image for conditions in the atmosphere that intercept incoming solar radiation, thereby affecting the intensity or frequency of reflected energy signals. It is ideal to collect those data on the date of the collection of the image. As the dataset used in the present study is of 2004, atmospheric data collected close to the date of collection by ionosphere laboratory under similar atmospheric conditions and at approximately the same solar time has been used here and discussed in the section 3.4.7. The instrument and procedure for collection of field spectra is discussed here.

4.3.1. Instrument

In order to make measurements of surface reflectance of geological samples, an analytical spectral device, a FieldSpec®-Pro spectroradiometer, was used. The ASD radiometer is a portable array-based spectrometer consisting of a spectrometer unit, computer interface, and fiber optic probe. The instrument has two integrated radiometers covering 350 to 2500 nm. The radiometer consists of one

silicon photodiode array and two fast scanning thermoelectrically (TE) cooled spectrometers with a spectral resolution 10 nm. The instrument was operated with 5° full-field-of-view (FFOV) foreoptics. A laptop interface with the instrument allows real time viewing of the spectrum recorded. The ASD instrument records the spectra in 2151 continuous bands. The spectral range and spectral resolution of the ASD instrument meet the present study requirement on Hyperion datasets. Table 4-3 shows the characteristics of the instrument used.

Table 4-3 Analytical Spectral Device FieldSpec-FR specifications (source: FieldSpec® Pro User Guide)

Spectral Range	350 - 2500 nm
Spectral Resolution	FWHM 3 nm for 350-1000 nm FWHM 10 nm for 1400 -2100 nm
Sampling Interval	1.4 nm for 350 - 1050 nm 2 nm for 1000 - 2500 nm
Scanning Time	100 milliseconds
Detector	One 512 element (Si photodiode array 350 - 1000 nms) Two separate, TE cooled, InGaAs (Indium-Gallenium-Arsenide) photodiodes 1000 - 2500 nm
Input device	Foreoptics gun

4.3.2. Instrument calibration

A certain amount of electrical current is generated by thermal electrons within the ASD and always added to the incoming photons of light during spectra collection. This adversely affects the spectra collection and has to be removed. This process is known as “Dark Current Correction”. Spectral data collection requires instrument calibration using a reference panel (“Spectralon” white reference) provided along with the instrument. During the white reference collection, a reference 100% line is available to the user to check the status of the instrument performance. White reference collection includes dark current correction and was repeated every 20 minutes during the collection of sample spectra. This minimises the effects of the changing lighting conditions on the recorded spectra. This calibration was repeated several times during the sampling period to establish changing light conditions or instrument drift.

Before the field spectra collection, to test the performance of the instrument a comparison for vegetation spectra was done. Figure 4-3 shows an example of tree foliage spectra (Dhoke variety of tree found abundantly in Udaipur environs) taken in IIRS campus compared with atmospherically corrected image spectra extracted from Udaipur image. The vegetation spectra from ASD and image exhibit similar trends, indicating precision of the instrument.

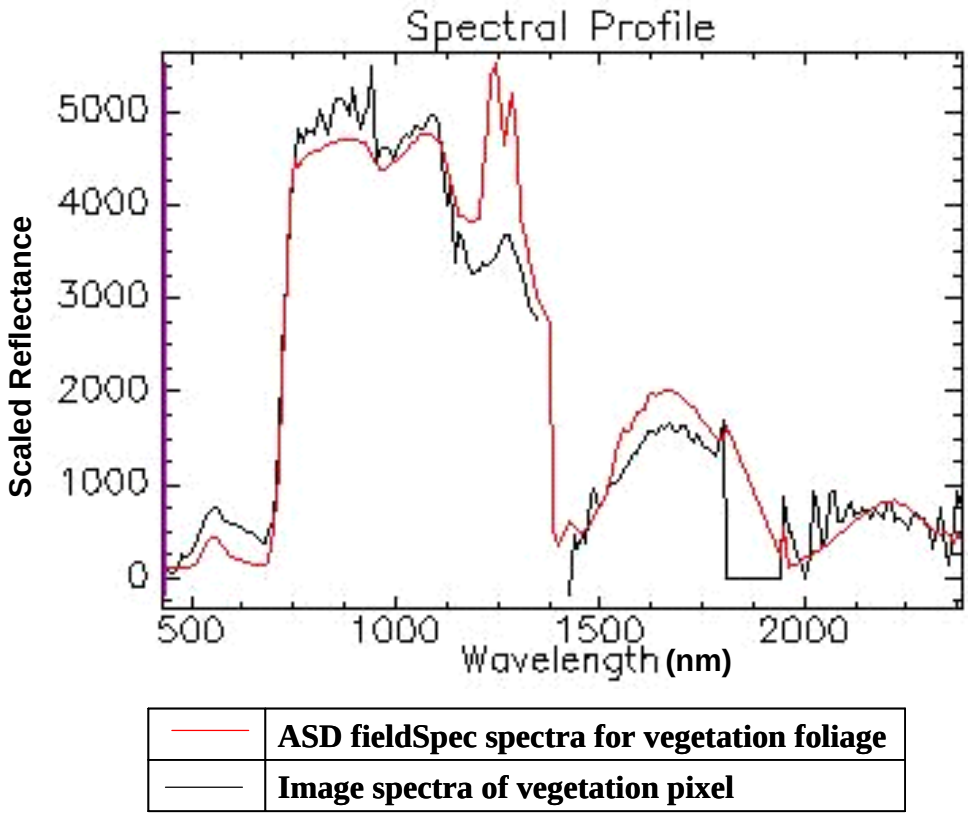

Figure 4-3 Vegetation spectra extracted from ASD and Image pixel. ASD spectra (red) re-sampled to Hyperion band width.

4.3.3. Spectral data collection

The northern part of the study area has been under survey by various National organizations for the last few years, and is considered a potential mineralization zone. Out of 32 spectra collected from ASD spectro-radiometer, 13 samples of the northern part of the study area were taken up for further processing. The field spectra collections was undertaken within 2 hours before and after solar noon to simulate the similar illumination conditions as during the satellite pass. The rock types were identified as Grey Quartzite and Chlortite schist

4.3.4. Creation of ASD spectral library

The ASD records spectra in 1251 bands at 2 nm band width (discussed in section 4.3.1). To compare the ground-measured spectra collected from ASD with that of atmospherically corrected image spectra, the ASD spectra were re-sampled to the Hyperion FWHM and bandwidth. A spectral library of re-sampled ASD spectra was created. The spectra from the ASD library were used as standard to compare image reflectance spectra extracted using the two atmospheric correction models ATCOR and FLAASH. Figure 4-4(a) shows the ASD extracted spectral, that was re-sampled to Hyperion band width (Figure 4-4(b)) to create a library created used in the present study.

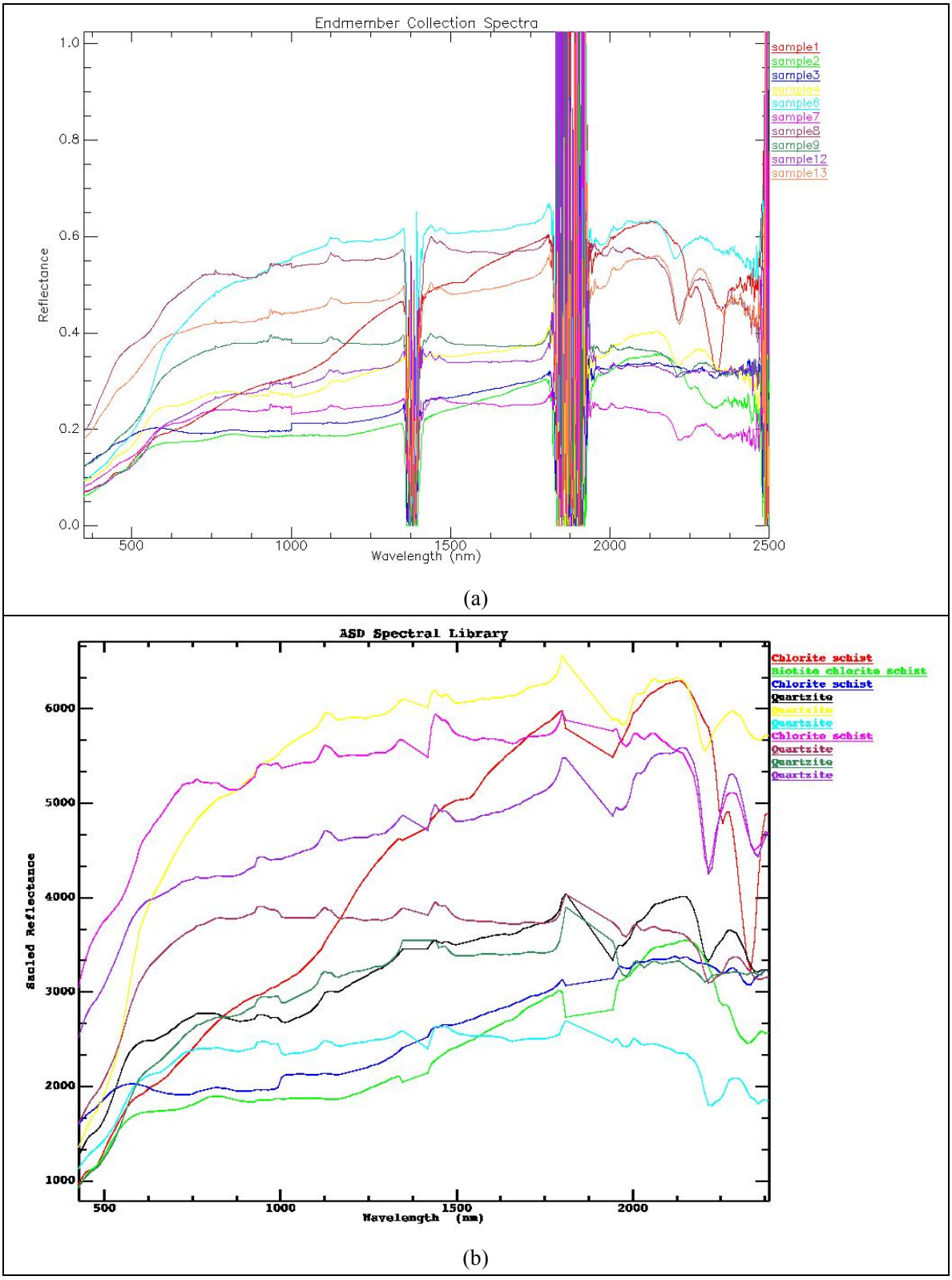

Figure 4-4 (a) ASD spectra of rock samples recorded using FieldSpec instrument. Noisy spikes centred at 1400 and 1800 nm signify atmospheric water vapour absorption during spectra collection. (b) Scaled reflectance ASD spectra re-sampled to Hyperion band width.

4.4. Image spectra collection

HyMap Rodalquilar, Spain dataset was used in the present study as a source of standard spectra extraction. This dataset was atmospherically corrected using ATCOR4 and field validated (Parvesh, 2006). A random stratified sampling strategy was adopted to decide on the location of sample points on HyMap image. Comparatively large and homogenous image signatures on HyMap image were selected on the basis of landuse interpreted from the image and published geological map. In order to take into account the difference in spatial resolution of HyMap (5 mts.) and Hyperion (30 mts.) 6x6 homogeneous pixels were interpreted on the HyMap image for extraction of sample points.

Based on the criteria mentioned above 13 pixel locations were selected for the extraction of HyMap image spectra, which corresponds to 4 homogenous classes (Alluvial deposits, Vegetation, Lazaras ash-flow tuff and Rhyolite ring dome). The Hyperion dataset of Rodalquilar, Spain were atmospherically corrected using FLAASH and ATCOR. The two images were georeferenced with the Hymap image as reference. These Hyperion datasets were used to extract reflectance spectra from the corresponding image location of Hymap. Table 4-4 shows the location and description and Figure 4-5 & Figure 4-6 shows spatial distribution of the sample points collected for HyMap and Hyperion images.

Table 4-4 Brief description of sample collected on HyMap image.

Sample no	HyMap location		Hyperion image location		Landuse description
	Easting	Northing	Easting	Northing	
1	589791	4098039	589881.71	4098033.23	Orchards
2	585303	4098627	585441.65	4098063.23	Agricultural land
3	587091	4098219	587091.67	4098213.24	Alluvial deposits
4	588177	4098759	588171.68	4098783.24	Lazaras ash-flow tuff
5	586215	4097709	586191.66	4097733.23	Lazaras ash-flow tuff
6	585423	4100319	585411.65	4100343.26	Rhyolite ring dome
7	587007	4099551	587001.67	4099563.25	Lazaras ash-flow tuff
8	589605	4096905	589731.70	4098033.23	Agriculture land
9	591051	4098039	591051.72	4098033.23	Alluvial deposits
10	590589	4097175	590571.72	4097193.22	Lazaras ash-flow tuff
11	591405	4098459	591381.73	4098483.24	Alluvial deposits
12	590079	4098987	590061.71	4098993.25	Lazaras ash-flow tuff
13	588405	4098897	590061.71	4098993.25	Lazaras ash-flow tuff

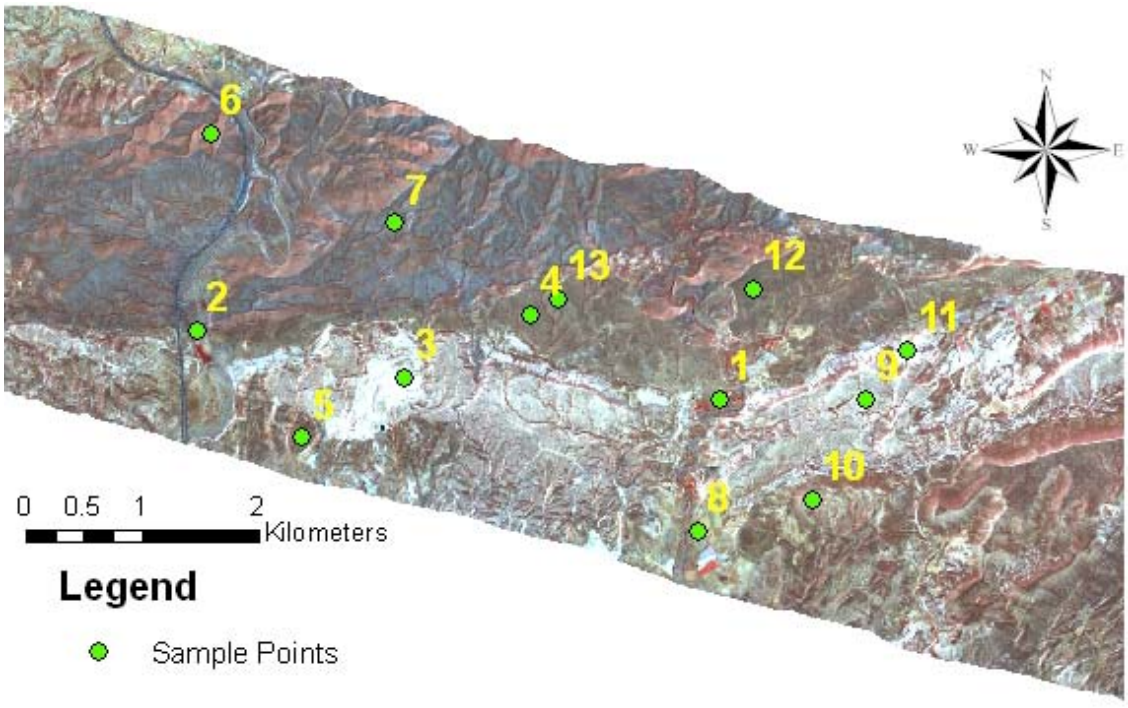

Figure 4-5 HyMap image of Rodalquilar, Spain showing location of sample points collected for creation of spectral library

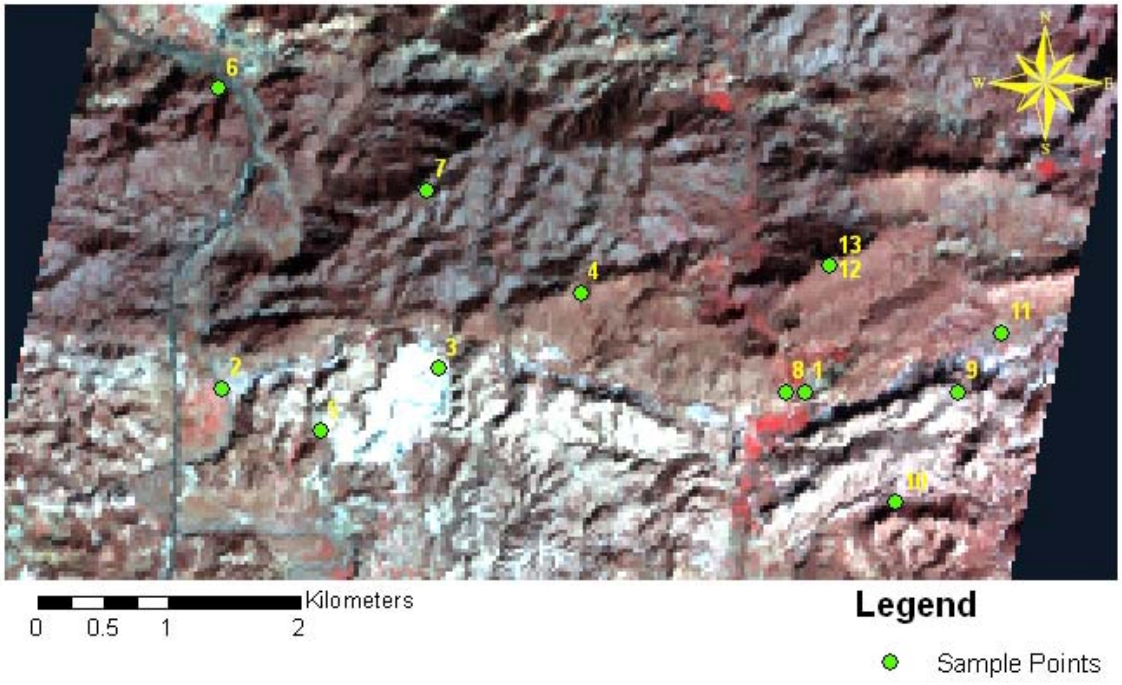

Figure 4-6 Spatial subset of Hyperion Image with sample locations

4.4.1. Creation of HyMap spectral Library

HyMap operates in 450 to 2480 nm wavelength range with 126 bands. The spectra extracted for HyMap image for 13 locations was re-sampled to Hyperion wavelength (356 to 2577 nm with 242 bands) and were taken as standard spectra. Figure 4-7 shows the re-sampled HyMap spectral library sample point.

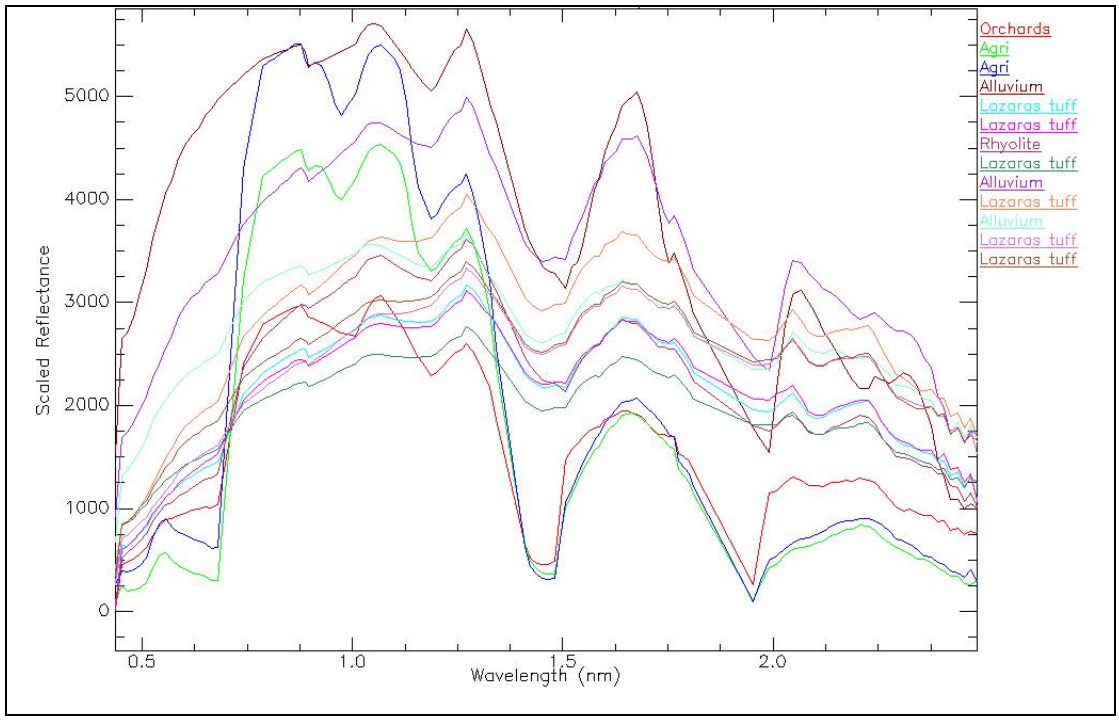

Figure 4-7 HyMap Image spectra of re-sampled to Hyperion wavelength.

This chapter gives an overview of the study area environs and the field investigation carried out. Pre-field preparation along with the sampling strategy adopted is also discussed here. This chapter also describes creation of spectral library to be used as standard spectra for comparison. The next chapter analyses the effect of processing steps adopted for atmospheric correction of Hyperion datasets and comparison of the out puts of the ATCOR and FLAASH with the standard spectra will be discussed.

5. Analysis and Results

The atmospheric gases, aerosols (airborne particulate matter) and clouds scatter and absorb solar radiation and can modulate the reflected radiation from the Earth. This attenuation affects the intensity and spectral composition of the radiation, and masks the useful spectral characteristic properties of the earth surface material. Therefore, applications involving quantitative studies to discern the spectral and chemical characteristics of the earth surface, atmospheric correction become essential.

In order to consider any atmospheric correction algorithm to be successful, it must provide good comparison between the image spectra and field spectra. The atmospheric correction algorithms are carefully implemented to model the atmospheric conditions that existed during the scene capture. This chapter analyses and highlights the results obtained from implementation of processing and atmospheric corrections preformed (discussed in chapter 3 and chapter 4) on Hyperion datasets of Udaipur and Rodalquilar.

5.1. Effect of de striping filter

The existing methods to identify the stripes use cumulative mean, variance, minimum and maximum of each pixel in each column. Detection of bad columns is carried out using set thresholds based on median values from its neighbourhood. The bad pixel is then replaced with the median value of its neighbourhood (Datt et al., 2003). The value of threshold is scene dependent and different for each band containing stripes. Setting up of the threshold is at the cost of changing the spectra.

The missing line filter designed in the present study only targets the visually identified bad columns (section 3-1), other pixel values remain unchanged. Hence the filter has a local balancing effect on the image. Examination of difference between the level 1R product and de-striped image indicates that the stripes in VNIR are removed and the image appears smooth. Figure 5-1 shows the effect of de-striping on the image and the corresponding DN values of one stripe on the image using the designed filter on the Hyperion datasets (as discussed in section 3.2.1). Form the visual inspection of the two images there is an over all contrast difference between the two. This difference is mainly due to the change in image statistics resulting from the de-striping of bad columns.

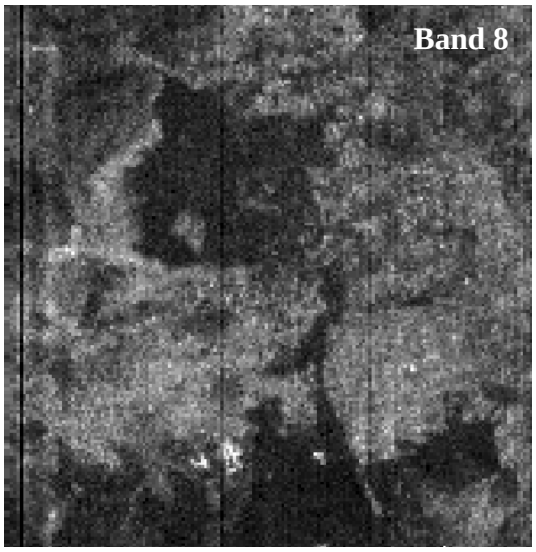

1075	1063	805	1213	1222
1163	1063	850	1037	1308
987	1063	895	1213	1308

(a)

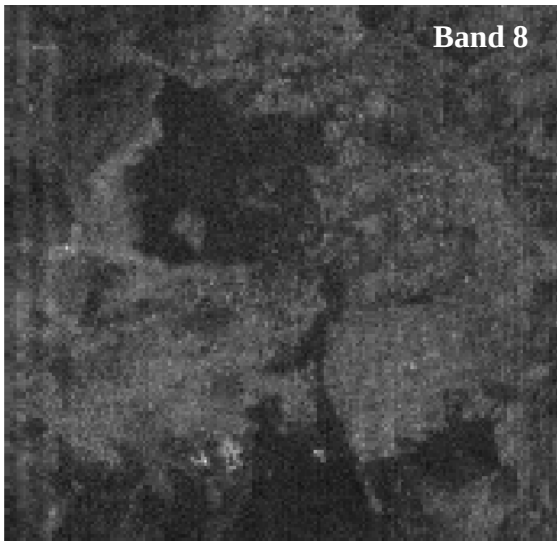

1075	1063	1109	1213	1222
1163	1063	1123	1037	1308
987	1063	1145	1213	1308

(b)

Figure 5-1 Hyperion level 1 R band 8 of Udaipur dataset (a) band with stripes with low DN values in grey column (b) de-striped band with changed DN values after applying local filter. (Min -max linear stretch applied based on image statistics)

The local balancing effect can also be seen on the image spectra. The image spectra improves after performing de-striping and spurious spikes in the VNIR region (300 to 700 nm) are reduced, while no change in the spectra is seen in SWIR region. Figure 5-2(a), (b) illustrates spectra taken at bad column in level 1 R product and post de-striping processing (pixel 6, 1148).

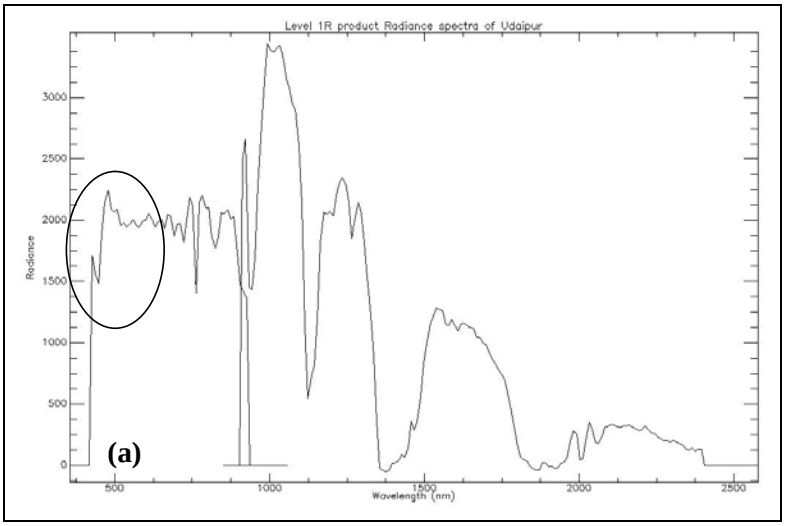

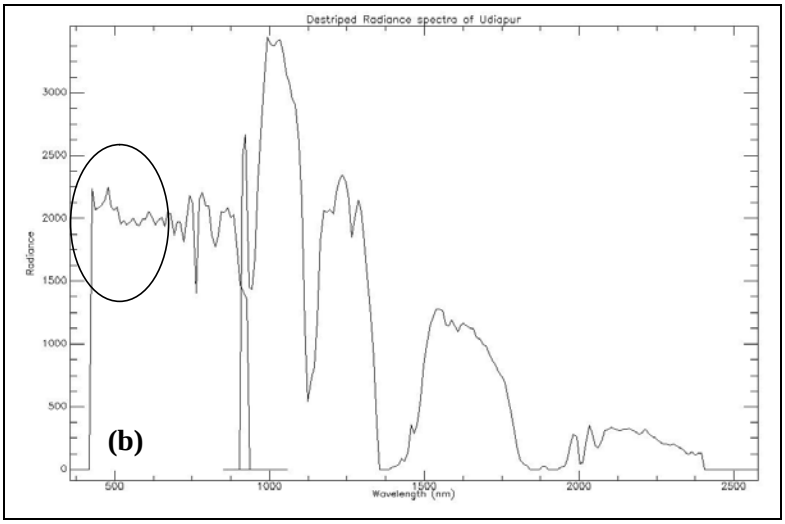

Figure 5-2 Local balancing effect of de-striping on the image spectra taken over know bad column. The encircled region shows the region of improvement. (a) spectra of Lavel 1 R product (b) spectra after de-striping.

5.2. Correction of wavelength shift

The estimated wavelength shift (as discussed in section 3.3.2) in the Udaipur and Spain datasets were applied during the atmospheric correction. Examination of the across-track profile of difference image of bands 40 and 42 at the same location as discussed in earlier section 3.3.1 indicates that the Normalized Optical Depth Derivative NODD algorithm has marginally reduced smiling in the datasets. Figure 5-3 show across track profile before wavelength calibration, where by strong brightness gradient towards the column 255 can be seen. This indicates presence of smiling in the Hyperion dataset. Figure 5-4 shows across track profile of at the same location, where the brightness gradient has reduced and more number of pixels exhibit difference values below zero. The difference image after wavelength recalibration still displays a brightness gradient. This indicates the NODD algorithm has marginally reduced smiling in the dataset.

The range of wavelength shift in Hyperion dataset is reported to be varying between 2.6 and 3.5 nm (Goodenough et al., 2003). The NODD algorithm calculates the spectral shift on the basis of the oxygen absorption at 760 nm in VNIR region. The reason for under performance of NODD algorithm could be attributed to consideration of only one reference point (oxygen) in VNIR region for correcting non linear nature of the spectral shift for the entire spectrum.

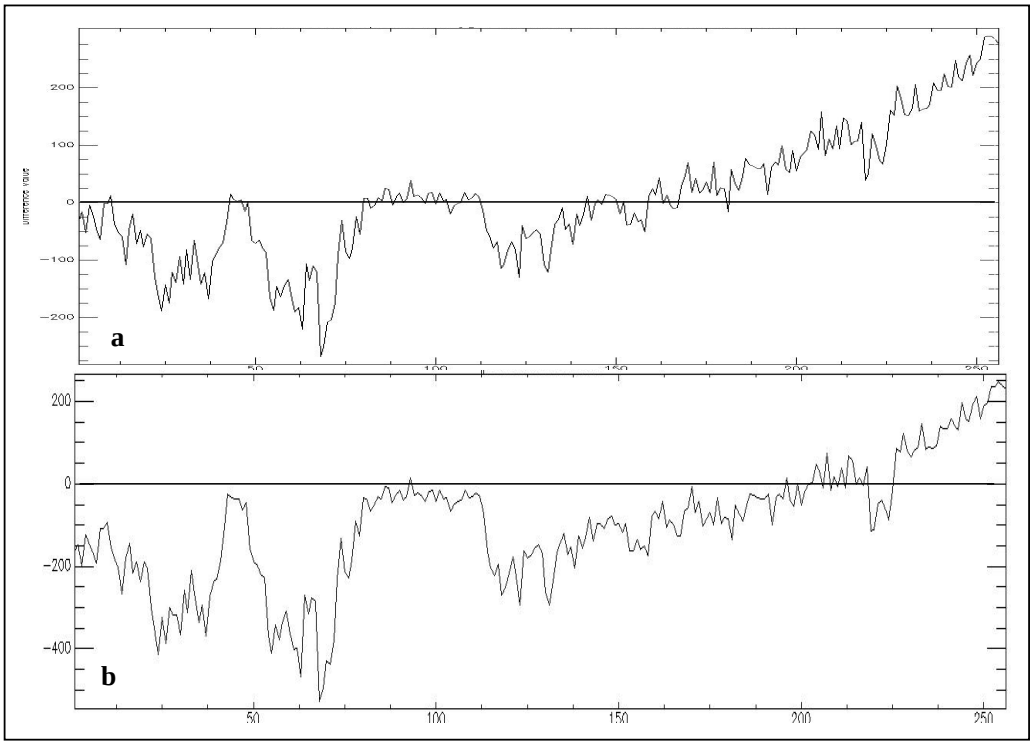

Figure 5-3 Across track profile of Oxygen absorption difference images (a) before wavelength calibration (b) after wavelength recalibration performed using NODD algorithm on Udaipur dataset.

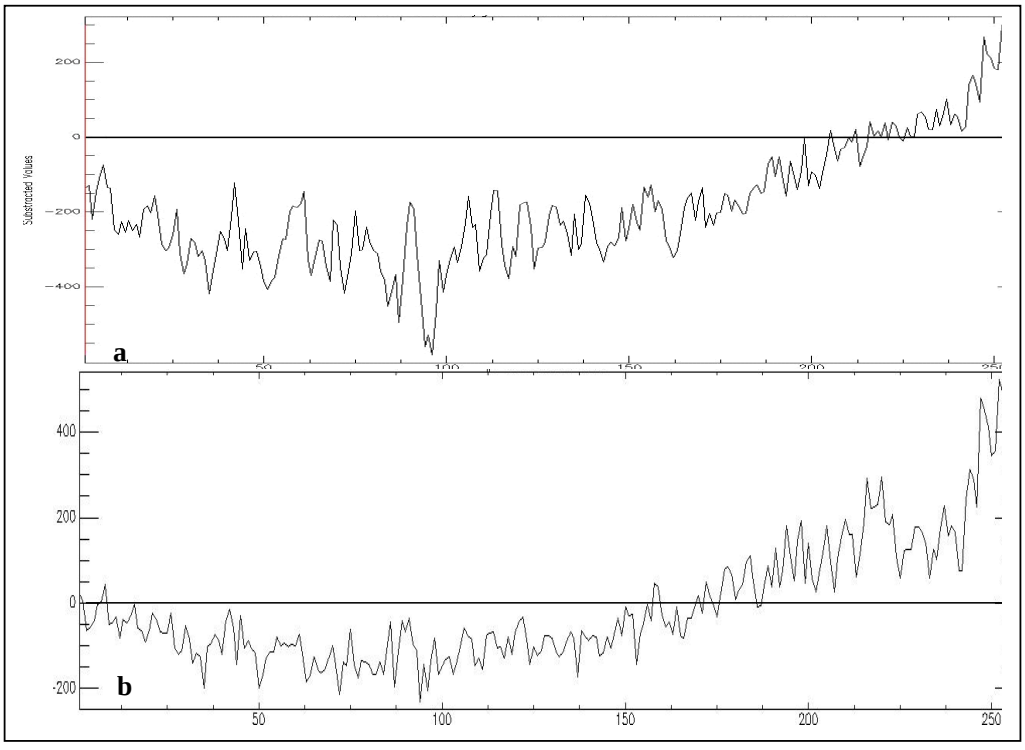

Figure 5-4 Across track profile of Oxygen absorption difference images (a) before wavelength calibration (b) after wavelength recalibration performed using NODD algorithm on Spain dataset.

5.3. Radiance spectra

The spectra extracted from Hyperion L1R dataset exhibits atmospheric gaseous absorption features. These absorptions can be observed in the spectral region from 400 to 2500 nm. The known absorption regions of the atmosphere are used here to identify the effects on image spectra (Figure 5-5).

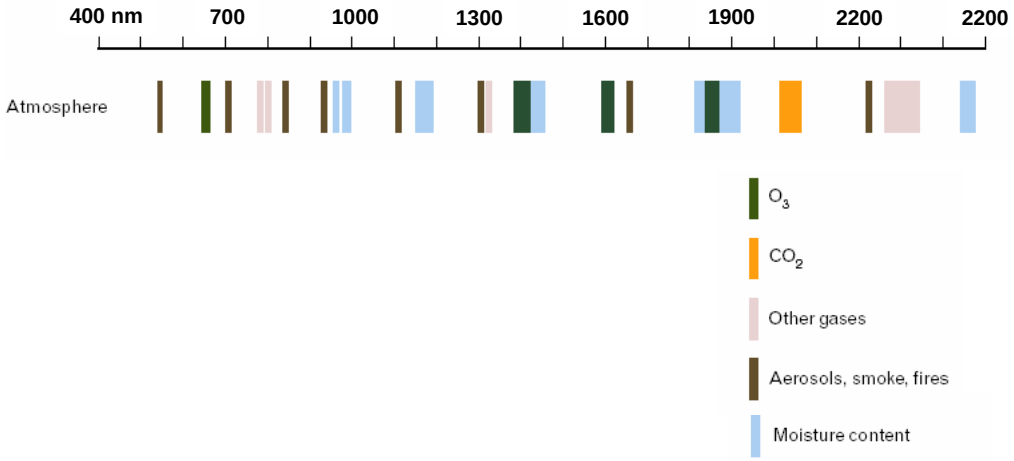

Figure 5-5 Known absorption regions of atmospheric constituents (Griffin and Hsiao-hua, 2003).

To understand the absorption regions in the radiance spectra radiance dataset of Udaipur was taken. A spectrum over vegetation was extracted to visually analyze the effects of the intervening atmosphere before the radiance image was subjected to atmospheric correction (Figure 5-6).

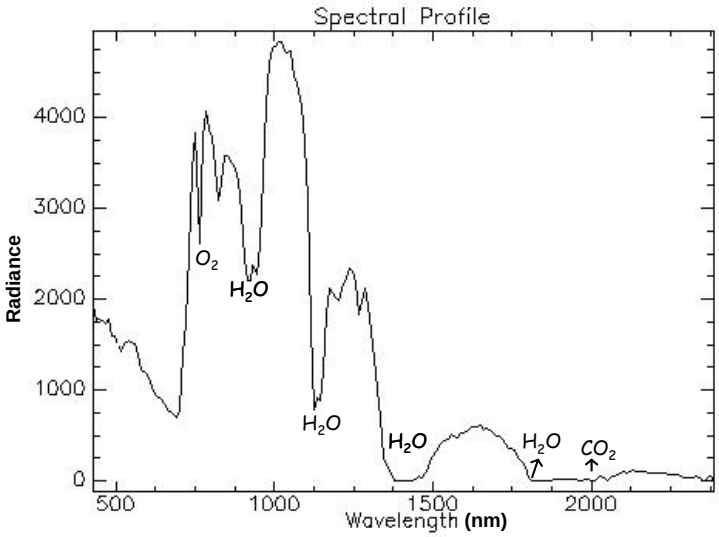

Figure 5-6 Radiance spectra of vegetation over Udaipur showing absorption features of oxygen, carbon di oxide.

At 760 nm, a strong, narrow oxygen absorption line is present. CO_2 is absorbed strongly from 1900 to 2055 nm. CO_2 also exhibits a weak absorption line at 1430 nm. At 940 and 1140 nm, water vapor absorption is strong and is used to derive the total column water vapor. Water vapor absorption near 1375 and 1900 nm is strong enough and makes retrieval of the surface reflectance difficult from the image.

The water vapor has the largest effect on the radiance. Oxygen and other gases along with aerosols in the atmosphere also affect the radiance spectra. The atmospheric correction models include modeled

atmosphere, aerosol models, water vapor retrieval and CO_2 concentration as input parameters. These input parameters along with image ratio methods adopted by the ATCOR and FLAASH to retrieve water vapor, CO_2 for the image itself should compensate for these absorption regions. ATCOR and FLAASH both use MODRTAN and has out performed other radiative transfer code especially in the water region 940 and 1130 nm and CO_2 at 2055nm (Staenz et al., 2002).

5.4. Surface reflectance RT models

ATCOR2 and FLAASH both use MODTRAN4 based radiation transfer models to assess radiation transfer properties of the atmosphere, and include a correction for "adjacency effect" (scattering of reflected radiance from surroundings into the pixel). The user is provided the choice of selecting the standard MODTRAN model for atmosphere and aerosol types to represent the scene, and a unique MODTRAN solution is computed for each image. The radiance images of Udiapur and Rodalquilar were processed as per input parameters summarized in Table 5-1 (discussed in section 3.4)

Table 5-1 ATCOR and FLAASH input parameters applied on radiance images of Udaipur and Rodalquilar, Spain datasets

ATCOR2			**FLAASH**		
Parameters	**Udaipur**	**Spain**	**Parameters**	**Udaipur**	**Spain**
Sensor type	Hyperion	Hyperion	Sensor type	Hyperion	Hyperion
Pixel size	30	30	Pixel size	30	30
Ground elevation	0.6 km	0.44 km	Ground elevation	0.6 km	0.44 km
Solar Zenith angle	37.214824º	31.487335º	Scene centre Lat/Long	24.6º N, 73.7º E	36.96º N, 2.026º W
Visibility	40 km	40 km	Visibility	40 km	40 km
Sensor altitude	un-editable	un-editable	Sensor altitude	703.3166 km	707.3276 km
Flight date	19/01/2004	06/02/2003	Flight date & flight time	19/01/2004 5:22:17	06/02/2003 10:33:49
Atmospheric file	hyperion.cal	hyperion.cal	-	-	-
Atmospheric model	h99000_ wv10_rura	h99000_ wv10_rura	Atmospheric model	Tropical	Mid-latitude summer
Adjacency range	1 km	1 km	-	-	-
Zones	0.5	0.5	Aerosol model	Urban	Urban
Region for water vapour	940 to1130	940 to1130	Water vapour retrieval	1135 nm	1135 nm
-	-	-	Spectral polishing	No	No
Water vapour absorption	Yes	Yes	Wavelength calibration	Yes	Yes
Haze removal	Yes	Yes	Advanced parameters		
Reflectance	100	100	Output	10000	10000

ATCOR2			**FLAASH**		
Parameters	**Udaipur**	**Spain**	**Parameters**	**Udaipur**	**Spain**
scale factor			reflectance scale factor		
-	-	-	MODTRAN resolution	15 cms-1	15 cms-1
-	-	-	MODTRAN multi scattering model	Scaled DISORT 8 Stream	Scaled DISORT 8 Stream
Reality spectra booster	Yes	Yes	-	-	-
CO_2 (un-editable)	360 ppm	360 ppm	CO_2 (user defined)	390 ppm	390 ppm

FLAASH model provides user with more options to control atmospheric correction process. To establish nominal sun-sensor geometry during image acquisition, user input parameters such as scene centre latitude, ground elevation, sensor height, flight time and date are used. The option of user defined sensor height is an addition in FLAASH. ATCOR2 establishes sun-sensor geometry on the basis on solar zenith angle and un-editable sensor height (defined as 705 km in hyperion.cal file). To accommodate for adjacency effect FLAASH allows selection of MODTRAN resolution and MODTRAN multiple scattering model. These settings can objectively be selected based on the variability in terrain conditions (uniformity or varying landuse). User defined CO_2 concentration level is also a useful input variable to be defined by the user in FLAASH, as the CO_2 levels varies with the presence of dense urban and industrial area in the scene. In ATCOR model CO_2 level is set at default 360 ppm and is un-editable. This difference in treating the input parameters by ATCOR and FLAASH models has a direct bearing on the reflectance simulation.

5.5. Comparative utility

The reflectance spectra extracted from the image using ATCOR and FLAASH were spectrally compared taking into account the atmospheric absorption and diagnostic absorption feature exhibited by the chemical and elemental composition. Conventionally, visual inspection and band depth mapping techniques are applied. These techniques provide useful information and visualizations of the data (Van der Meer and De Jong, 2003).

5.5.1. Vegetation spectra

Reflectance properties of vegetation in the VNIR and SWIR part of the spectrum are dominated by the strong atmospheric absorption regions and absorption properties of the chlorophyll a and b pigments. The image spectra extracted from ATCOR and FLAASH exhibit no significant absorption at wavelengths 1900 and 2100 nm, indicating that, CO_2 input of 390 ppm (default being 320) was sufficient to compensate for CO_2. Narrow absorption at 760 nm corresponding to O_2 is compensated by both the models, as no significant dip is seen in the spectra. Pigments in vegetation show absorption at 640 and 660 nm. The shape of the absorption feature is clearly seen in the FLAASH extracted spectra Figure 5-7(a), (b). Similar observation have also been reported on HYDICE image corrected using FLAASH (Griffin and Hsiao-hua, 2003) (Datt et al., 2003). Spurious peaks in both the spectra at 940 nm indicated the strong water absorption is under estimated by both models, this signifies that

stronger water absorption region at 1140 nm is over estimated and is seen as sharp dip at 1124 nm and 1146 nm in ATCOR and FLAASH, respectively. Earlier studies have shown similar results using FLAASH (Griffin and Hsiao-hua, 2003). The difference in the positions of the water vapour absorption could be attributed to the process of treating the water vapour in the two models. The approach by ATCOR is based on the differential absorption method, using the water absorption bands from the image; whereas in FLAASH water vapour is extracted using three image band ratio methods in combination with a spectral weighted average.

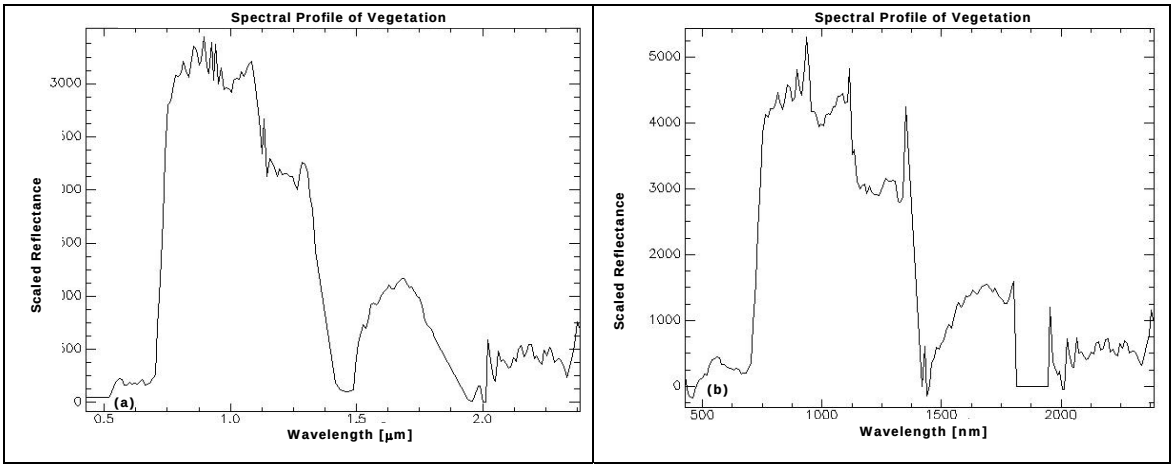

Figure 5-7 Atmospherically corrected vegetation Spectra of Udaipur (a) ATCOR corrected (b) FLAASH corrected

Reflectance from vegetation is dominated by the green leaf interaction with the EMR. ATCOR and FLAASH exhibit clear diagnostic dips at 660 and 668 nm which corresponds to the presence of chlorophyll-b in the healthy leaves (Van der Meer and De Jong, 2003). Shape of the red absorption in ATCOR extracted spectra indicate over estimation it is correctly estimated by FLAASH. Similar results were reported in FLAASH corrected Hyperion datasets (Griffin and Hsiao-hua, 2003). Cellulose causes absorption at 2280 nm in spectra derived from both the models. A diagnostic absorption dip is also seen at 2062 and 2064 nm, which corresponds to the presence of protein and nitrogen in the leaves in ATCOR and FLAASH, respectively.

5.5.2. Water body spectra

Water bodies have a different response to EMR than water bound-up in molecules in that they do not exhibit discrete absorption features. Water has a high transmittance for all visible wavelengths, but the transmittance increases with decreasing wavelength. However, suspended material and pigments cause increased reflectance in the visible region (Van der Meer and De Jong, 2003). In the near infra red and in SWIR all EMR is absorbed by water. FLAASH and ATCOR corrected spectra exhibits spurious spikes in 1900 to 2500 nm wavelengths indication over estimation of water vapour absorption (Figure 5-8(a) and (b)). Similar observations have been reported in SWIR region (Kruse, 2003).

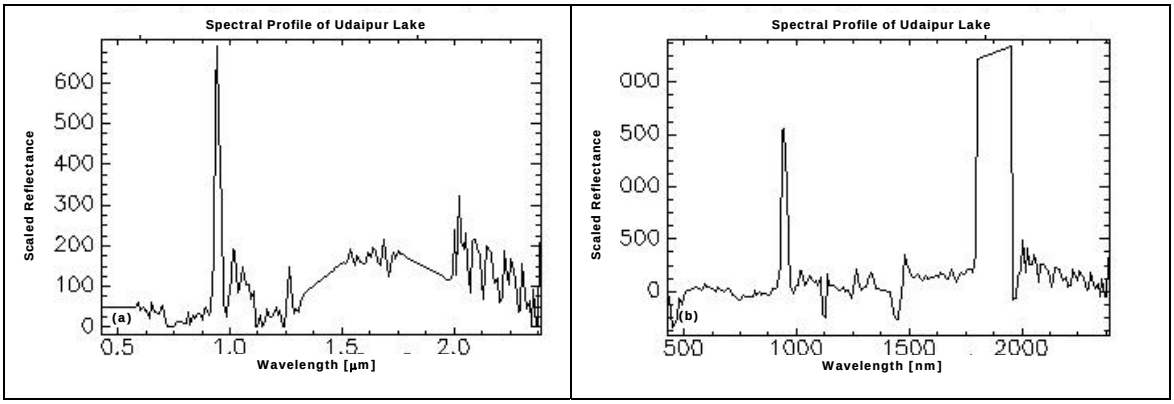

Figure 5-8 Atmospherically corrected waterbody spectra of Udaipur (a) ATCOR corrected (b) FLAASH corrected

5.5.3. Lithological spectra

Quartzite exposures in and around Udaipur are being explored for mineralization by various national exploration agencies. Quartzites of Udaipur primarily comprises of quartz, feldspars, muscovite and other trace minerals like rutile, zircon and heavy metals. The Udaipur quartzites sample taken for this analysis is exceptionally hard and compact exhibiting concoidal fractures when broken with a rock hammer. A megascopic examination of the rock sample shows quartz as the major mineral in the sample associate with minerals biotite and zircon.

Quartz does not exhibit any significant absorption feature and is considered as featureless spectrum, while minerals such as muscovite and trace mineral zircon exhibit absorption feature at 2200 nm. This absorption feature is seen in the ATCOR and FLAASH extracted spectra at the same wavelength (Figure 5-9(b), (c). The presence of this absorption feature is further confirmed by the ASD field spectra of quartzite taken from the study area, and is seen in Figure 5-9(a).

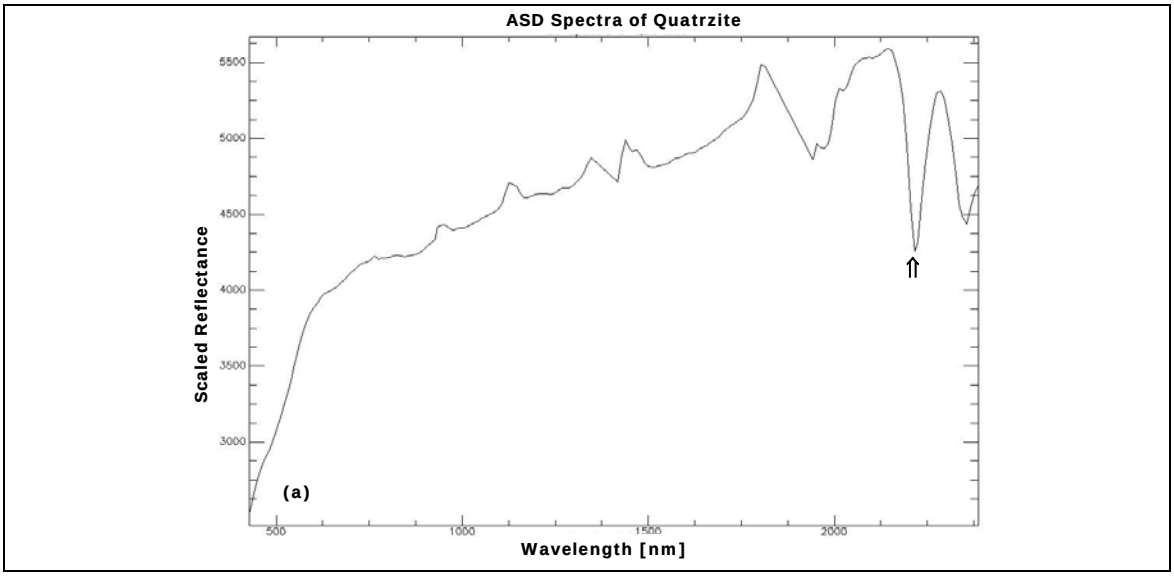

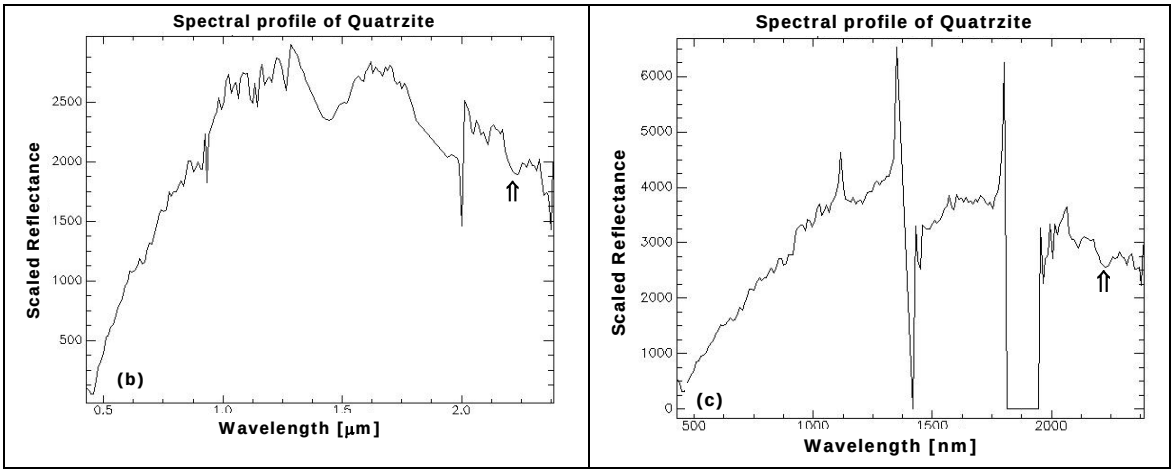

Figure 5-9 Udaipur Quartzite spectra, arrow mark indicating the Hydroxyl band absorption feature. (a) ASD Spectra, (b) ATCOR spectra and (c) FLAASH spectra.

This visual analysis of the atmospherically corrected spectra extracted from ATCOR and FLAASH indicate that the over all shapes of the vegetation, water and quartzite considered here, match with the ASD spectra. However the spectra still has spurious spikes in SWIR region that can not be attributed to any specific feature on ground.

5.5.4. Matching parameters

Techniques based on image ratio and difference such as Spectral Angle Mapper (SAM), Euclidean Distance (ED), Normalized Euclidian Distance (NED) provide useful information on spectral similarity between reference and test spectra.

The spectral angle mapper (SAM) has been widely used as a spectral similarity measure. It calculates spectral similarity between the reference reflectance spectrum (ASD spectrum) and the test spectrum (image spectrum). The angle between two spectra is used as a measure of discrimination (equation 5-1). The spectral similarity between the image spectrum (t) and reference spectrum (r) can be expressed as an average angle (θ) between the two spectra for each channel (i) (Van der Meer and De Jong, 2003).

$$\theta = \cos^{-1}\left[\frac{\sum_{i=1}^{n} t_i r_i}{\sqrt{\sum_{i=1}^{n} t_i^2 \sum_{i=1}^{n} r_i^2}}\right] \qquad \textbf{Equation 5-1}$$

The result of SAM is an angular difference measured in radian ranging from zero to π/2 which gives a qualitative estimate of similarity between image spectrum and ASD spectrum (Van der Meer and De Jong, 2003). Small spectral angle values correspond to high similarity between image spectra and ASD spectra. Larger angle values correspond to less similarity.

Another popular spectral similarity measure is Normalized Euclidean distance (NED), which is also being used to calculate the distance between two spectra as a spectral similarity measure. The Euclidean distance between n-dimension spectra (x) and (y) is given as equation 5-2:

$$e(x,y) = \sqrt{\sum_{i=1}^{n} (x_i - y_i)^2} \qquad \textbf{Equation 5-2}$$

The values of ED are positively defined and do not lie within a set range. As Normalized eucledian distance values are invariant to scalar multiplication, NED gives a better scaled measure for comparison (Robila and Gershman, 2005). The ED vector is first normalized (equation 5-3) and NED is calculated with equation 5-4.

$$N_x = x / \bar{x} \qquad \textbf{Equation 5-3}$$

$$NED_{x,y} = e\left(N_x, N_y\right) \qquad \textbf{Equation 5-4}$$

The standard range of SAM calculated for the equation 5-1 is 0 to 90. Lower the angle more is the similarity. The SAM values are rescaled between 0 and 1 in ENVI. The expected NED value ranges from 0 to 1 and is rescaled to 0 to 10, as the equation 5-3 returns a very low value. ED values are positively defined and do not fall within as set interval. The larger number of bands leads to larger value for the distance (Robila and Gershman, 2005). The spectral angle is relatively insensitive to changes in brightness, whereas the normalized values of ED that is NED takes into account the brightness difference between the two vectors, thus giving a better estimate of spectral similarity. The Normalized Euclidean Distance (NED) derived from the Euclidean distance between the reference spectra and image spectra, outperforms most of the measures currently in used.(Robila and Gershman, 2005). SAM and NED values are not specified in value range, value of 0 indicates a perfect match and higher values indicate greater dissimilarity.

5.5.5. Spectra matching results

Use of NED as spectral similarity measure has been strongly proposed for target detection and has been observed to out perform existing similarity measures. Owing to its computational simplicity and accuracy of results based on target detection experiments using HYDICE (Robila and Gershman, 2005) this measure is chosen for comparing ATCOR and FLAASH extracted spectra with the standard reference spectra. The ASD field spectra of 10 samples from Udaipur were re-sampled to Hyperion band width and were taken as input reference spectra for the calculation of the spectral similarity measures that is SAM and NED. Table 5-2 shows the SAM and NED for each of the corresponding pixels of the 10 field samples for both the ATCOR as well as FLAASH processed images. Although the average SAM value (0.2015) for ATCOR processed image is smaller than the average SAM value (0.2919) for the FLAASH processed image, it is can not be decisively stated that the ATCOR model performs better than FLAASH model. The reason for this is that the spectral angle is relatively insensitive to changes in brightness (Robila and Gershman, 2005). Also much spectral class confusion have been reported while considering SAM as a similarity measure (Van der Meer, 2006). On comparing the average NED values for ATCOR and FLAASH processed images, it is seen that FLAASH performs better than the ATCOR because the average NED value for FLAASH is 0.7446 which is less that the average NED value for ATCOR (2.79). Since NED values takes into account the brightness difference between the two vectors, thus giving a better estimate of spectral similarity (Robila and Gershman, 2005) it can be inferred from this analysis that FLAASH out performs ATCOR.

Table 5-2 Values of spectral measures calculated for ACTOR and FLAASH corrected images. Expected ranges of values for SAM are 0 to 1 and for NED 0 to 10. Lower the value more is the similarity to the ASD reference spectra.

Sample code	SAM ATCOR	SAM FLAASH	NED ATCOR	NED FLAASH
1	0.2086	0.2625	4.1537	1.1014
2	0.2601	0.3308	1.6669	0.4109
3	0.2007	0.2853	1.1567	0.4242
4	0.3302	0.5111	3.7595	1.1763
6	0.0902	0.2095	3.7743	0.7764
7	0.1801	0.2763	1.57	0.3679
8	0.1934	0.2581	3.9349	0.9057
9	0.1803	0.2519	3.2694	0.8549
12	0.1338	0.2322	0.8805	0.4836
13	0.2385	0.3019	3.7696	0.945
Average	0.2015	0.2919	2.79	0.7446

Spectral similarity plot (Figure 5-10 (a), (b)) of SAM show similar trend for all 10 field samples sample, with SAM values of ATCOR extracted spectra is closer to the ASD extracted spectra.

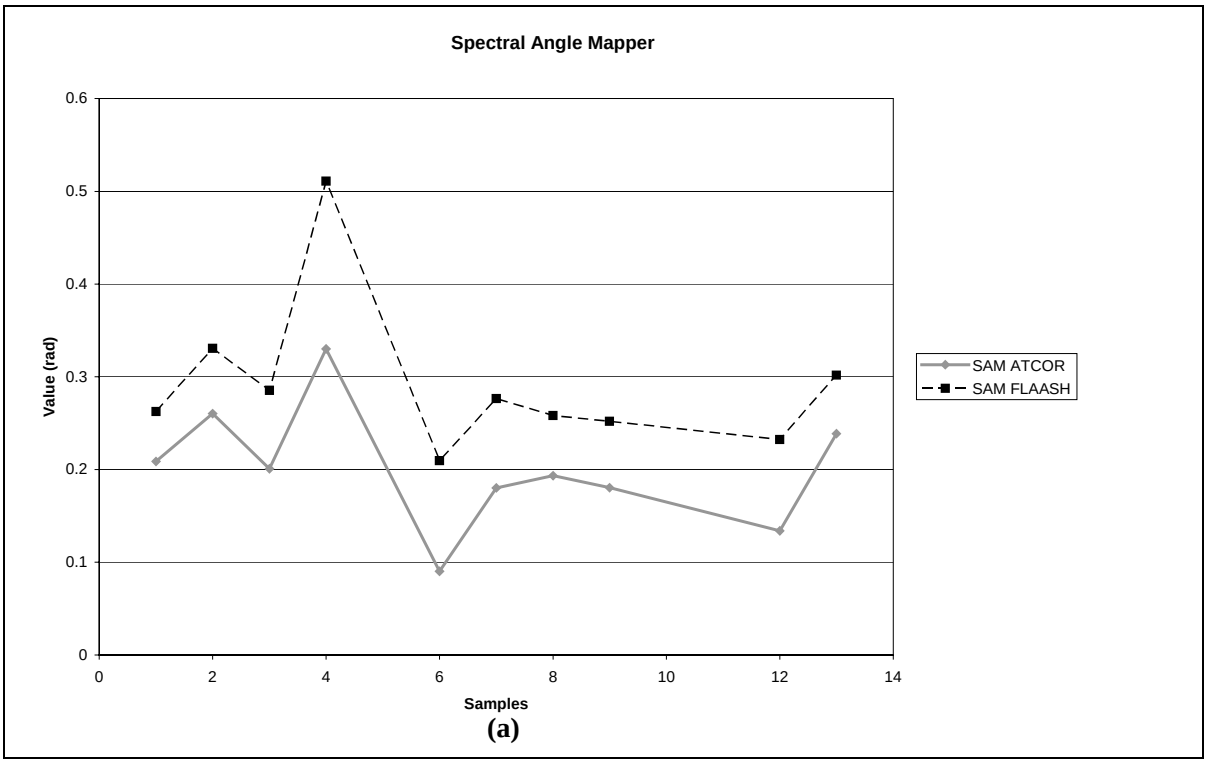

(a)

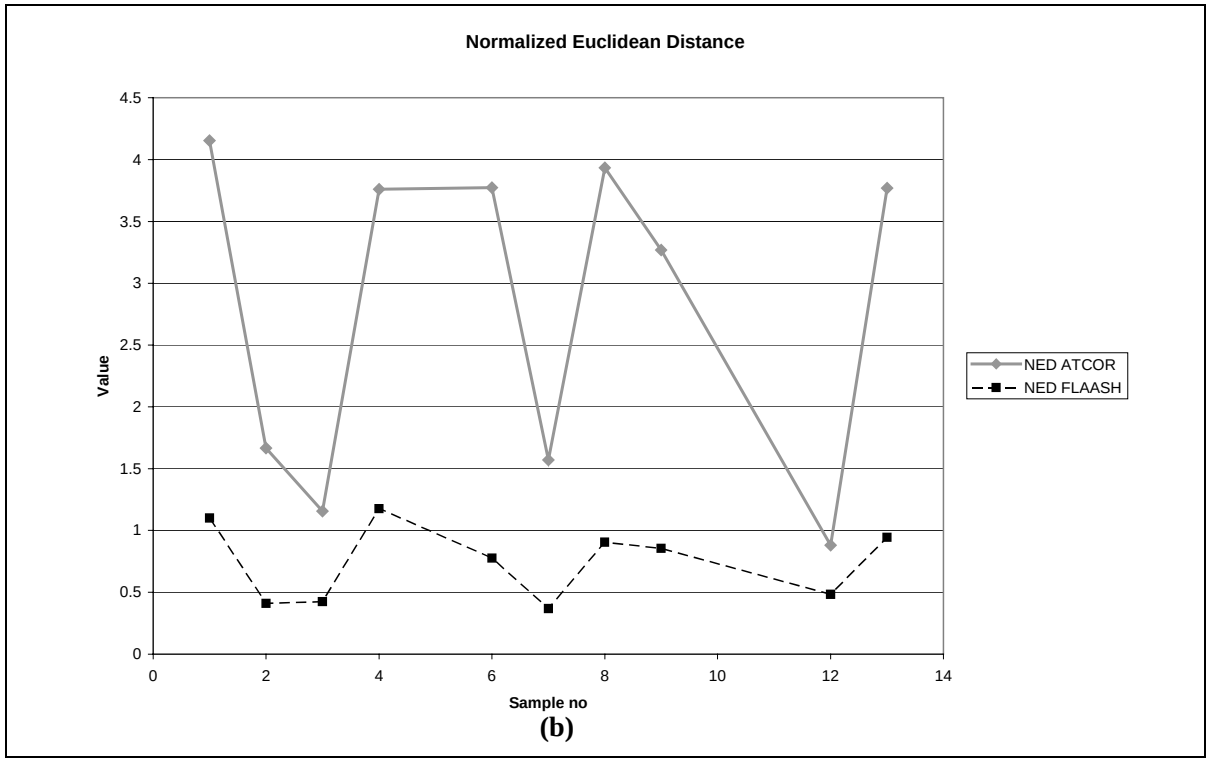

Figure 5-10 Comparative performance of ATCOR and FLAASH for Udiapur dataset.

Reference spectra from 13 locations on the HyMap image of Rodalquilar, Spain were re-sampled to Hyperion band width and compared with the Hyperion image spectra of the corresponding location. The two image spectra were tested for spectral similarity using SAM and NED. The extracted values are shown in (Table 5-3) In case of Rodalquilar, Spain Dataset the analyses of the spectral similarity measures give similar results. SAM for ATCOR corrected image is less (0.2205) as compared to FLAASH (0.4584), where NED value (2.8036) for ATCOR is more than FLAASH (0.8205) indicating the consistency of better performance of FLAASH as compared to ATCOR atmospheric correction model.

Table 5-3 Spectral similarity values of comparison between HyMap image spectra and FLAASH corrected spectra of Rodalquilar, Spain Expected ranges of values for SAM are 0 to 1 and for NED 0 to 10. Lower the value more is the similarity to the ASD reference spectra.

Sample no.	SAM ATCOR	SAM FLAASH	NED ATCOR	NED FLAASH
1	0.1965	0.3536	1.206	0.5648
2	0.1701	0.4856	2.4908	0.7334
3	0.1363	0.6063	5.3358	0.92
4	0.1202	0.4168	2.1912	0.5697
5	0.1124	0.4117	1.5153	0.6888
6	0.1674	0.4418	3.6556	0.7018
7	0.1826	0.4097	1.8947	0.5406
8	0.4937	0.5136	5.7916	1.1378
9	0.1977	0.3664	1.7988	1.0264
10	0.1623	0.4062	2.0371	0.8605
11	0.2579	0.4544	1.6573	1.1513

Sample no.	SAM ATCOR	SAM FLAASH	NED ATCOR	NED FLAASH
12	0.1376	0.4094	2.3896	0.6342
13	0.532	0.6837	4.4831	1.1372
Average	0.22051	0.4584	2.8036	0.8205

Similarity measure plot of SAM for 13 samples show that the ATCOR extracted spectra are more similar to the HyMap spectra. This could be attributed to the fact that the HyMap image was also corrected using ATCOR4. ATCOR extracted spectra exhibit higher values of NED for all 13 samples than FLAASH extracted spectra (Figure 5-11). As NED values are invariant to scalar multiplication the lower values of FLAASH extracted spectra indicate more similarity to the Hymap extracted spectra.

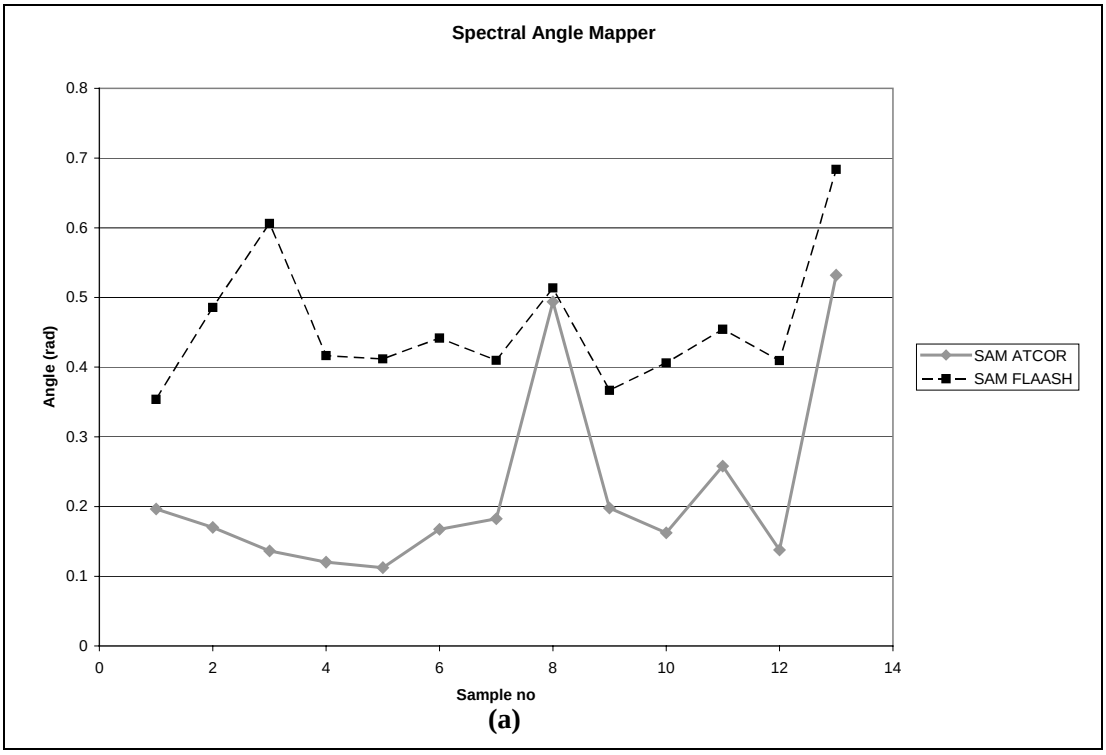

(a)

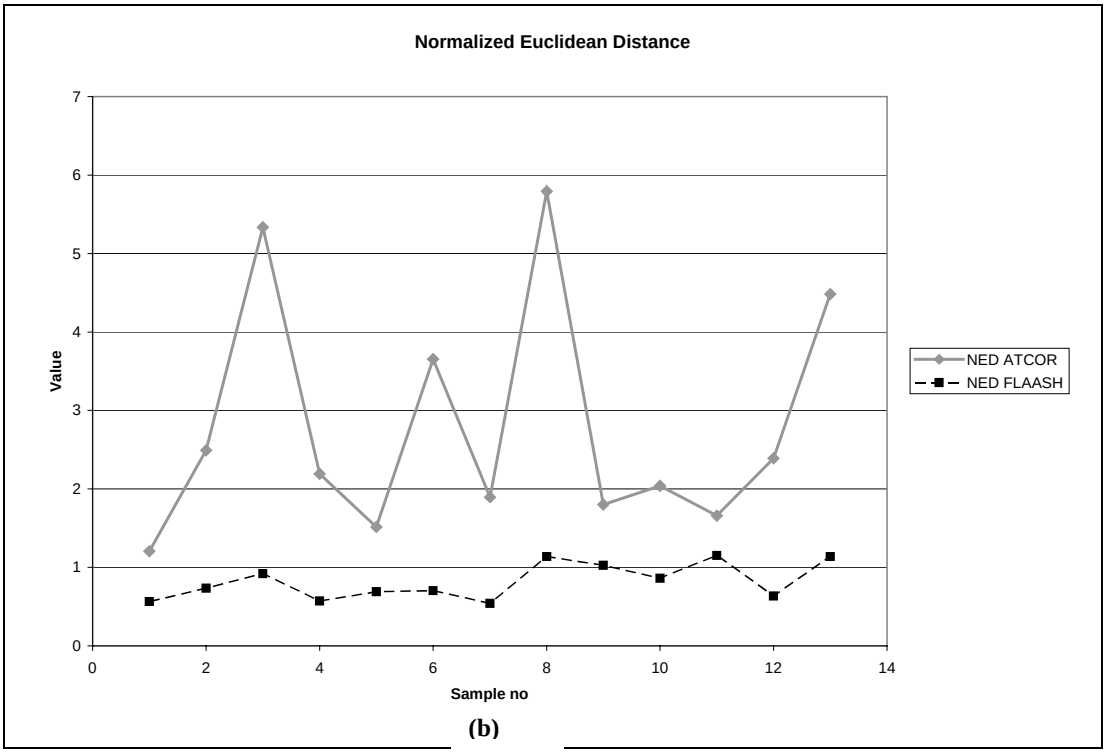

Figure 5-11 Comparative performance of ATCOR and FLAASH for Rodalquilar, Spain dataset.

5.6. Band positioning and absorption analysis

The atmospherically corrected reflectance spectra contain compositional information of minerals, mineral mixtures, rocks and vegetation, exhibited as characteristic absorption at specific wavelength. As discussed in section 3.5, spectral reflectance in the visible and near-infrared wavelengths provides a rapid and inexpensive means for determining the mineralogy of samples and obtaining information on chemical composition. The significance of performing band positioning and absorption analysis is to see whether the spectra for a sample feature extracted from the atmospherically corrected Hyperion dataset of Udaipur behave in accordance with the USGS standard spectroscopic band absorption characteristics of that sample feature.

In order to attempt band position absorption, the atmospherically corrected spectra were examined at 2200 nm to 2300 nm for Udaipur quartzite. Quartz does not exhibit any significant absorption feature and is considered as featureless spectrum. Aventurine Quartz found in India has scales of Biotite / Muscovite, Zircon or Hematite distributed within it. Samples of ultra mafic origin that have Biotite / Muscovite and Zircon inclusions exhibit characteristic absorption feature at hydroxyl bands of 1400 nm and between 2200 and 2600 nm indicating presence of Fe-Mg-OH and Fe_2O_3. Figure 5-12 shows this characteristic absorption feature for the Aventurine quartz sample from India as published by USGS Denver spectroscopy laboratory (source: http://speclab.cr.usgs.gov/spectral.lib456.descript/DESCRIPT/quartz.avent.hs117.html). A similar absorption feature is also exhibited in the ASD field spectra of Udaipur quartzite and the spectra extracted from the atmospherically corrected Hyperion dataset of Udaipur, as seen in Figure 5-9(a).

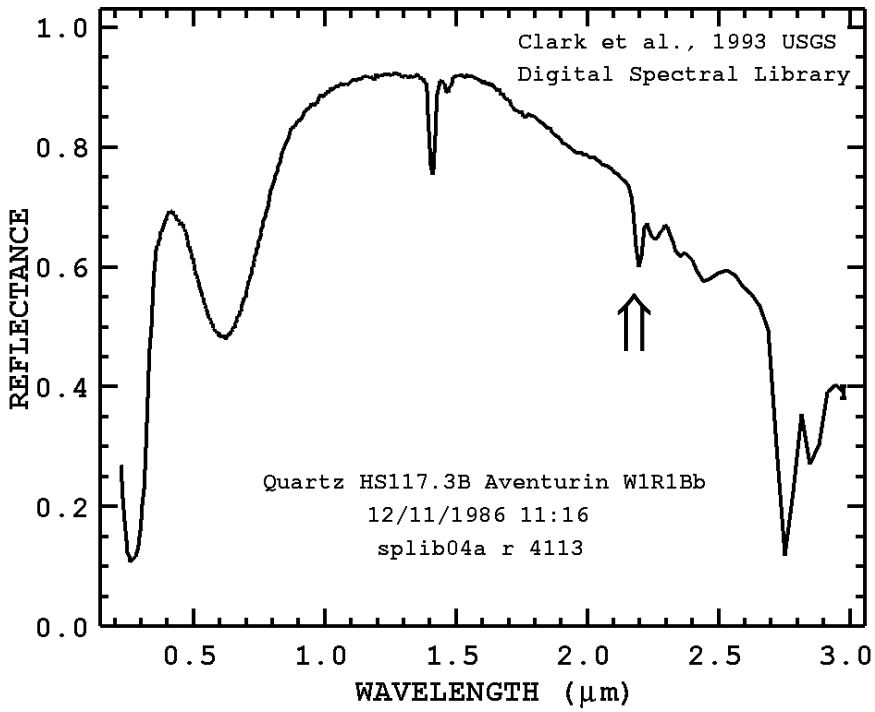

Figure 5-12 Aventurine Quartz reference spectra. Arrow mark shows the Hydroxyl band absorption feature in SWIR region.

As discussed in section 3-6, for the derivation of asymmetry and band depth parameters (i.e. S_1, S_2, A_1, A_2) required for the band position absorption analysis, continuum removed bands between 2280 to 2340 nm were used. Two shoulders S1 at 2337.04 and S2 at 2286.55 were selected for the diagnostic absorption at 2316.84 nm. Two absorption points for interpolating the depth A1 at 2326.94 and A2 at 2296.64 were used (Figure 5-13).

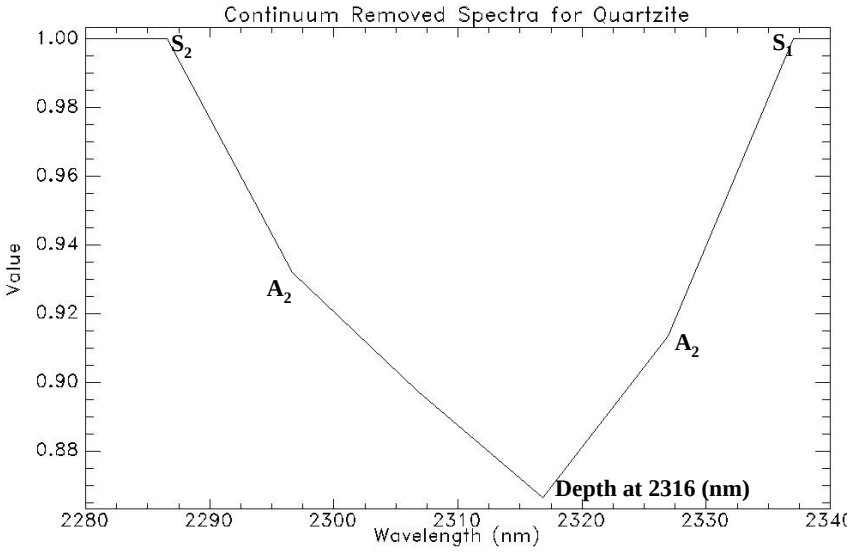

Figure 5-13 Continuum removed absorption position of Udaipur Quartzite

The derived band asymmetry and depth images enhance the analysis of Hyperion dataset for surface compositional mapping. The resulting asymmetry image shows pixel values ranging between 0.0035 – 0.0113 and can be interpreted as weakly skewed towards the shorter wavelength (Figure 5-14). The

asymmetry image displays pixels that have the same asymmetry as that of the quartzite spectra at 2316 nm.

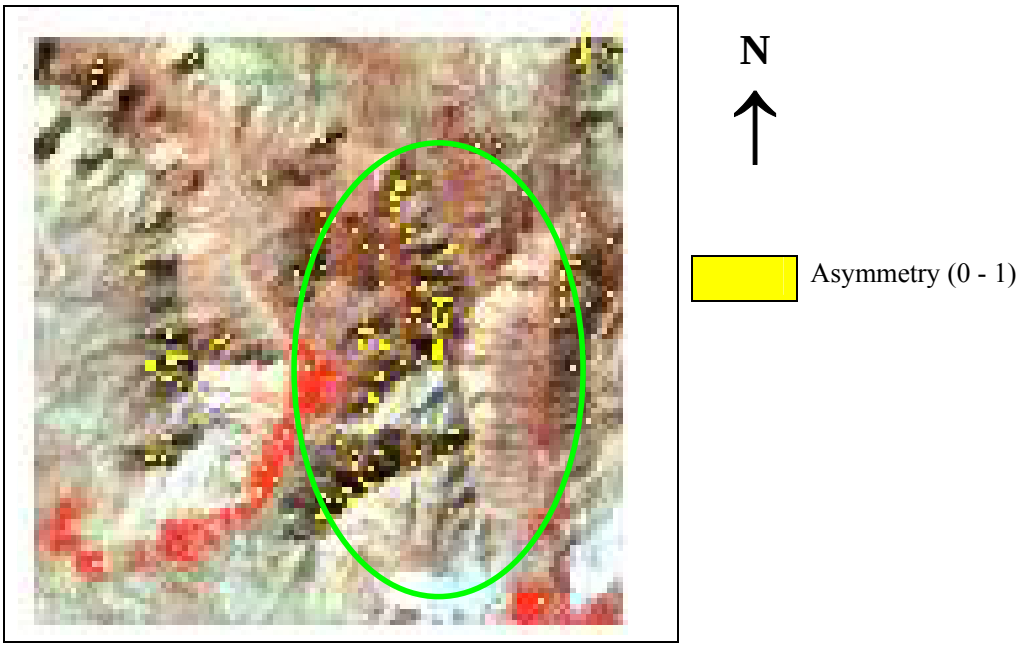

Figure 5-14 Asymmetry image for Udaipur Quartizes. Yellow pixels have asymmetry value range between 0 and 1 are weakly skewed towards shorter wavelength.

The depth of absorption feature in quartzite is higher in relation to the continuum. Higher depth values indicate a greater possibility of the occurrence of mineral that is displaying the absorption feature in the spectra (Figure 5-15).

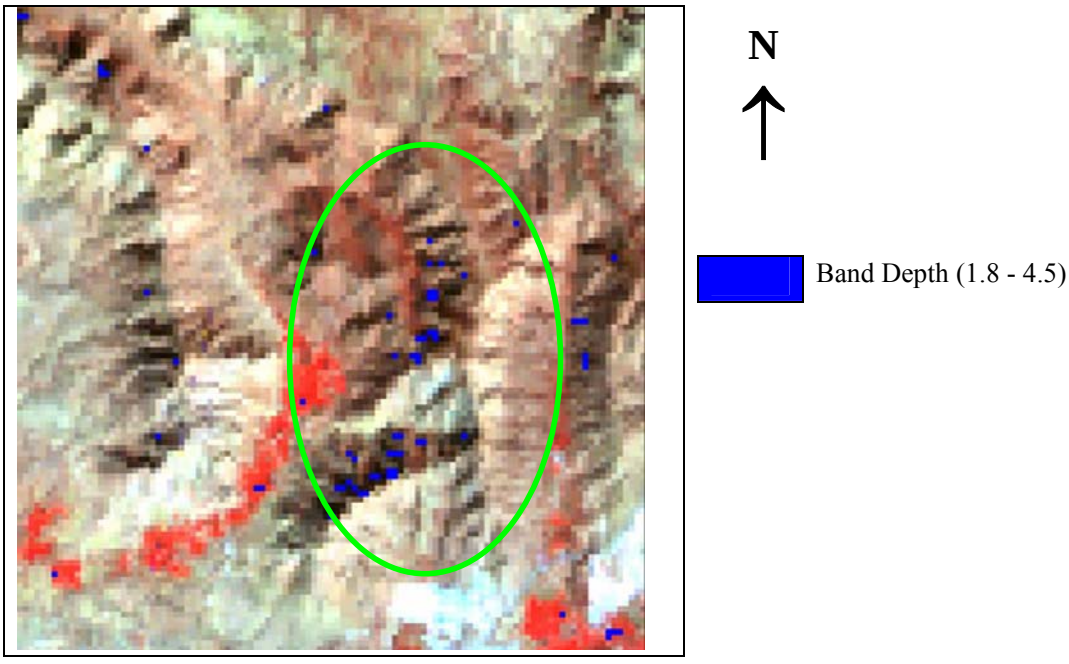

Figure 5-15 Depth image of Udaipur Quartzites. Blue pixels have depth range of 1.8280 to 4.57.

Band absorption analysis has not shown good results for Udaipur Hyperion dataset. On the contrary good results were observed on AVIRIS dataset for hydrothermal mineral assemblage in Cuprite mining site for Al-OH absorption (Van der Meer, 2004). In case of Udaipur Quartzite, the absorption

range is covered by 6 bands. The result of band position and absorption analysis shows a very low number of pixels (2206) qualifying for the hydroxyl band depth and asymmetry, most of which fall in the shadow region. This indicates that identification of absorption feature depends not only on the spectral quality of the dataset but also on absorption width (number of bands that constitutes the absorption range). As discussed in section 3-1, Udaipur dataset taken for the present study has SNR 0 to 55 in SWIR region, which could be one of the reasons why the absorption technique has not shown good results. Earlier studies have reported Hyperion SNR in the range of 1 to 60 in SWIR region resulting in less information extraction from Hyperion for mineralogical targets (Kruse et al., 2003a). Other reason of underperformance of this technique for Hyperion could be attributed to very strong superimposed hydroxyl absorption due to atmospheric moisture accumulation in the shadowed region of the study area. This dominant absorption interfered with the characteristic hydroxyl absorption of Udaipur quartzites. Hence the areas in shadow region show similar band depth and asymmetry in the study area.

This chapter discussed and analyzed the results obtained from the processing of the Hyperion datasets. The performances of the two atmospheric correction model used in the present study were also discussed. An emphasis was also laid on comparison of output reflectance spectra with the ASD field spectra and HyMap image spectra as standard. To check the spectroscopic quality of the Hyperion reflectance spectra was also attempted. In the succeeding chapter conclusions drawn from the analysis of the processing carried out in the present study with future recommendations are discussed.

6. Conclusions and recommendations

This chapter gives the conclusions arrived at, after a detailed analysis on the utility of two atmospheric correction models namely ATCOR2 and FLAASH in retrieving calibrated spectral profile form EO-1 Hyperion datasets of Udaipur, India and Rodalquilar, Spain. The objectives of the present study were to derive apparent reflectance from radiative transfer models for Hyperion data sets and analyze absorptions along the contiguous spectra to enable effective pre-processing. The study also intended to evaluate the comparative utility of atmospheric correction models and to attempt band positioning absorption analysis and evaluate its effectiveness. The following sections states the conclusion arrived at during the study.

6.1. Conclusions

Hyperion datasets require de-striping before it is subjected to atmospheric correction. A local balancing filter was designed to remove bad columns from the Hyperion datasets. The designed filter targets only the visually identified band columns and replaces it by the 3×3 neighbourhood mean, without taking into account the bad column values. This filter only replaces the bad column values without changing the other DN values in the entire image. It was found that the local balancing effect improved the radiance spectra, which is seen in the output (reflectance spectra) of the atmospheric correction model. Unavailability of ready to uses tools to carry out de-striping; the designed filter can be useful for all Hyperion images to be taken up for further studied.

Uncertainty in the wavelength calibration of the sensor results in smiling effect in Hyperion dataset. The spectral shift was calculated on Udaipur and Spain datasets. To compensate for smiling effect, oxygen absorption band based NODD algorithm is implemented in FLAASH. The atmospherically corrected reflectance spectra after wavelength recalibration continue to exhibit smiling, as two oxygen band subtraction image show moderate brightness gradient in across track direction. The NODD algorithm adopted for wavelength recalibration has only marginally improved the image. This indicates that smiling effect still exist in the corrected dataset. Thus NODD algorithm under performs to compensate for smiling in Hyperion dataset.

Visual comparison of ATCOR2 and FLAASH retrieved reflectance spectra indicated that both the models compensated for the O_2, and CO_2 atmospheric gas absorptions. The two models underperformed for atmospheric water vapour at 940 nm and overestimated water vapour at 1140 nm. The absorptions due to lignin, chlorophyll b, protein in vegetation were identifiable on reflectance spectra extracted for the models. Also both the models exhibited spurious spikes in SWIR region that cannot be attributed to any specific feature on ground. Thus visual comparison did not conclusively indicate any relative performance of the models used.

Visual comparison of reflectance spectra retrieved for ATCOR2 and FLAASH reveals descriptive assessment without quantitative assessment of the quality of the spectra. To enable us to express the qualitative similarity in terms of quantities, spectral similarity parameters SAM and NED have been

used considering ASD field spectra and HyMap spectra as standard. Lower SAM values of ATCOR extracted spectra indicate its better performance over FLAASH, where as low NED values of FLAASH extracted spectra show its better performance over ATCOR2. NED being a better similarity measure it is concluded that FLAASH performs better than ATCOR2. The results of spectral similarity measures were found to be identical for both Udaipur and Spain datasets. Therefore, it can be concluded that FLAASH consistently performs better than ATCOR2 for Hyperion datasets.

To assess the spectroscopic quality of the reflectance spectra extracted from FLAASH corrected image, absorption analysis technique for band positioning was attempted for quartzite absorption feature at 2200 nm. Absorption analysis has not shown good results due to low signal-to-noise ratio in the selected wavelength region and strong superimposed hydroxyl absorption due to residual atmospheric moisture in the same wavelength region. Nevertheless, this technique can be attempted on other absorption features in VNIR region, where SNR was observed to be higher in Hyperion dataset and further be substantiated with linear un-mixing classification techniques.

Although the ATCOR and FLAASH algorithms are robust, they have not compensated for atmospheric contributions. Reflectance spectra extracted from both ATCOR2 and FLAASH merely show similar trends when compared with the ASD extracted spectra or HyMap spectra. Owing to the inherent low signal to noise ratio in Hyperion it seems difficult to extract calibrated spectra from atmospherically corrected Hyperion datasets.

The following research questions were answered to meet the objectives of the present study:

6.1.1. What is the usefulness of existing atmospheric correction models?

Atmospheric corrections can be taken up using relative and physics based absolute methods. The relative methods are computationally fast but are only statistical image normalization tools. The physics based methods use the atmospheric profile, terrain altitude and sun-sensor geometry to remove the contribution of atmospheric constituents for the image. The atmospheric correction models are used to derive reflectance from the image datasets. Physics based, ATCOR2 and FLAASH both use MODTRAN4 code radiative transfer code. The radiative transfer codes simulate the reflectance image by taking into account sun-sensor geometry at the time of imaging, temperature water vapour and gases concentrations profiles, aerosol type and concentration, spectral variation of ground reflectance and band availability of bands in absorption regions. The reflectance extracted for the atmospheric correction models allow direct comparison between spectra extracted from image and field measured spectra.

As discussed in 5.4, based on an initial analysis of option available for input parameters required to run the two atmospheric correction models, it can be concluded FLAASH model provides user with more options to control sun-sensor geometry, accommodate for adjacency effect and CO_2 concentration levels. The quality of simulated reflectance depends on the input provided during the atmospheric corrections. Even so this observation does not actually give any idea of better performance of one model over the other.

Spectral similarity measures, SAM and NED do not have any specific range or thresholds, but the quality of the spectra is expressed with respect to the variation in values as compared to the standard reference. Higher values of SAM and NED indicate greater dissimilarity and values tending to zero

indicate greater similarity. Spectral similarity results based on average SAM for ATCOR2 is 0.20 and 0.22 which is lower than the average SAM values of FLAASH (0.29 and 0.46). Normalized Euclidean Distance (NED) is considered as the best measure to judge the similarity between the two spectra. NED shows low values for FLAASH (0.74 and 0.82) as compared to average NED value of 2.79 and 2.80 for ATCOR2 corrected spectra in both the datasets. It is therefore concluded that FLAASH has outperformed ATCOR2. Consistency in the result of similarity for both Udaipur and Spain datasets indicated better performance of FLAASH for Hyperion datasets.

6.1.2. How good are the atmospheric correction models for VNIR and SWIR portion of Hyperion?

Reflectance images were derived from the ATCOR2 and FLAASH atmospheric correction models. The reflectance spectra extracted from the two atmospheric correction models were compared by two methods. The first method involved visual comparison for known absorption features of atmospheric gases and other known materials. The second involved a comparison of the spectral similarity parameters using the field measured spectra and HyMap extracted spectra as standards in Udaipur and Rodalquilar datasets respectively.

From a visual comparison of the reflectance spectra from the two atmospheric correction models used in the present study it is conclude that for VNIR region, absorption due to gases are effectively compensated for, where as atmospheric water vapour is overestimated at 940 nm and underestimated at 1140 nm. A visual analysis of vegetation spectra show characteristic absorption features of chlorophyll b (660 and 668 nm), protein and nitrogen (2062 and 2064 nm) are visible in vegetation spectra. In FLAASH extracted spectra, visible and infrared region performed well and is in concurrence with chlorophyll absorption vegetation spectra, where as in ATCOR extracted spectra chlorophyll red absorption is over estimated.

SWIR region of the spectrum was analysed for Udaipur quartzite. The characteristic absorption due to hydroxyls in quartzite is seen in spectra extracted from both the models. However, the out puts of both the models exhibit sporadic spurious spikes in SWIR region of the spectrum which could not be attributed to low SNR in the SWIR region and inability of atmospheric correction model to adequately compensate for atmospheric contributions from Hyperion dataset.

6.1.3. How can the smiling effect in the spectra be minimised?

Attempts to minimise smiling have been made using moving linear fitting and interpolation technique taking ground spectra as reference and forward MNF transformation. But these techniques create false spectra (artifacts) in Hyperion dataset. Removal of smiling also requires quantifying the wavelength shift and calibration of wavelength by modelling in addition to accurate knowledge of atmospheric constituents and surface conditions. Normalized Optical Depth Derivative (NODD) algorithm implemented in FLAASH bypass the requirement of knowledge about atmosphere. A strong oxygen absorption feature at 760 nm is utilized to quantify the wavelength shift in the dataset. NODD algorithm convolutes the sensor measured radiance spectrum to model the correction factor in the wavelength.

The spectral shift was calculated for the two datasets using NODD algorithm implemented in FLAASH. The results show that the NODD algorithm marginally reduces the smiling in Hyperion datasets. This underperformance of NODD algorithm may be because of consideration of only one

reference point (oxygen absorption feature) in VNIR region to correct the non-linear spectral shift. As CO_2 also registers a significant absorption in SWIR region, its combination with O_2 may result in minimizing the smiling effect in Hyperion dataset.

6.1.4. How effective is the absorption analysis technique for band positioning?

Band absorption analysis technique has been shown to be very effective for mineral targeting on AVIRIS dataset. An attempt was made in the present study to see its effectiveness with regards to Hyperion dataset. Udaipur quartzites of ultramafic origin are known to be host rock for mineralization. It exhibits featureless spectra, but presence of biotite/muscovite and other heavy minerals characteristic Fe-OH hydroxyl absorption feature is registered in SWIR region. The band position and absorption analysis for this hydroxyl absorption did not give good results, which is attributed to the reason that the Hyperion dataset exhibits lack of spectral quality in SWIR region and overlapping dominant absorption due to residual atmospheric water vapour in the shadow region.

6.2. Recommendations

- Further studies considering oxygen in VNIR region and carbon-di-oxide in SWIR region together to correct for spectral shift needs to be carried out, to address the non-linearity in the spectral shift, which may result in better performance of existing atmospheric correction models.
- Improvement in SNR of Hyperion sensor should be worked out for future space borne Hyperspectral sensors to allow the same level of mineral mapping capability as airborne sensors.
- Further studies on band position and absorption analysis considering broader absorption features in VNIR region could be carried out to verify for the spectral quality of Hyperion dataset.
- Possibility for selection of bands specific to an application requirement based on band depth analysis needs to be explored further.

7. References

Brunn, A., Dittmann, C., Fischer, C. and Richter, R., 2001. Atmospheric correction of 2000 HyMap Data in framework of the EU-Project Mineo. Society of Photo-Optical Instrumentation Engineers, September 2001.

Cocks, T., Jenson, R., Stewart, I., Wilson and Shield, T., 1998. The HyMap airborne hyperspectral sensor: the system, caliberation and performance, 1st EARSEL Workshop on Imaging Spectroscopy, , Zurich,.

Cunningham, C.G., Arribas, A.J., Rythba, J.J. and Arribas, A., 1990. Mineralized and unmineralized calderas in Spain; Part I, evolution of Los Frailes Caldera. Mineral Deposita, 25: 21-28.

Dasora, N., Dave, R. and Pandey, R., 2005. Study of aerosol optical depth at 1020 nm and precipitable water content at Udaipur. In: S. Gunthe and V. Singh (Editors), First Prof. R. Ananthakrishnan Memorial Conference on Atmospheric Science, Climate Change and Environment Studies, Pune, India, pp. 141.

Datt, B., McVicar, T.R., Van Niel, T.G., Jupp, D.L.B. and Pearlman, J.S., 2003. Preprocessing EO-1 Hyperion hyperspectral data to support the application of agricultural indexes. IEEE Transactions on Geoscience and Remote Sensing, 41(6 Part 1): 1246-1259.

Deschamps, P.Y., Herman, M. and Tanre, D., 1983. Definitions of atmospheric radiance and transmittances in remote sensing. Remote Sensing of Environment, 13(1): 89-92.

Felde, W.G. et al., 2003. Analysis of Hyperion data with FLAASH atmospheric correction algorithm, Algorithms and Technologies for Multispectral, Hyperspectral, and Ultraspectral Imagery IX. SPIE Aerosense Conference, Orlando, pp. 90-92.

Gao, B.C., Montes, M.J. and Davis, C.O., 2004. Refinement of wavelength calibrations of hyperspectral imaging data using a spectrum-matching technique. Remote Sensing of Environment, 90(4): 424-433.

Goodenough, G.D., Dyk, A., Niemann, O.K. and Pearlman, J.S., 2003. Preprocessing Hyperion and ALI for forest classification. IEEE Transactions on Geoscience and Remote Sensing, 41(6 Part 1): 1321-1331.

Griffin, M.K. and Hsiao-hua, K.B., 2003. Compensation of Hyperspectral data for atmospheric effects. Lincoln Laboratory Journal, 14(1): 29-53.

Gross, H.N. and Schott, J.R., 1998. Application of Spectral Mixture Analysis and Image Fusion Techniques for Image Sharpening. Remote Sensing of Environment, 63(2): 85-94.

Guanter, L., Richter, R. and Moreno, J., 2006. Spectral calibration of hyperspectral imagery using atmospheric absorption features. Applied Optics, 45(10): 2360-2370.

Hadjimitsis, D.G., Clayton, C.R.I. and Hope, V.S., 2004. An assessment of the effectiveness of atmospheric correction algorithms through the remote sensing of some reservoirs. International Journal of Remote Sensing, 25(18): 3651-3674.

Janssen, L.L.F., Weir, M.J.C., Grabmaier, K.A. and Kerle, N., 2004. Geometric aspects. In: N. Kerle, L.F.L. Janssen and G.C. Huurneman (Editors), Principles of remote sensing. ITC education text book series. The international institute for geo-information science and earth observation (ITC), Enschede, pp. 317-345.

Jarecke, P., Yokoyama, K. and Barry, P., 2002. On-orbit solar radiometric calibration of the Hyperion instrument, Imaging Spectrometry VII. SPIE, pp. 225-230.

Jensen, J.R., 1996. Introductory Digital Image Processing. Prentice Hall Series in geographic information science. Prentice, New Jersey, 316 pp.

Jupp, D.L.B., Datt, B., Lovell, J., Campbell, S. and King, E., 2004. Backgroung notes for Hyperion data user workshop, CSIRO office of space science and applications, Earth Observation Centre.

Kaufman, Y.J. and Sendra, C., 1988. Algorithm for Automatic Atmospheric Corrections to Visible and near-IR Satellite Imagery. International Journal of Remote Sensing, 9(8): 1357-1381.

Kneizys, F.X. et al., 1996. The MODTRAN 2/3 Report and LOWTRAN 7 MODEL, Phillips Laboratory, Geophysics Directorate.

Kruse, F.A., 2003. Comparison of ATREM, ACORN and FLAASH atmospheric corrections using low-altitude AVIRIS data of boulder, Co.

Kruse, F.A., Boardman, J.W. and Huntington, J.F., 2003a. Comparison of airborne hyperspectral data and EO-1 Hyperion for mineral mapping. IEEE Transactions on Geoscience and Remote Sensing, 41(6): 1388-1400.

Kruse, F.A., Boardman, J.W. and Huntington, J.F., 2003b. Final Report: Evaluation and Geologic Validation of EO-1 Hyperion, NASA.

Kruse, F.A., Kiereinyoung, K.S. and Boardman, J.W., 1990. Mineral Mapping at Cuprite, Nevada with a 63-Channel Imaging Spectrometer. Photogrammetric Engineering and Remote Sensing, 56(1): 83-92.

Liang, S. and Fang, H., 2004. An Improved Atmospheric Correction Algorithm for Hyperspectral Remotely Sensed Imagery. IEEE Transactions on Geoscience and Remote Sensing, 1(2): 112-117.

Lillesand, T.M. and Kiefer, R.W., 1999. Remote Sensing and Image Interpretation. John Wiley & Sons, Inc, 9-10, 592-597 pp.

Marion, R., Michel, R. and Faye, C., 2006. Atmospheric correction of hyperspectral data over dark surfaces via simulated annealing. IEEE Transactions on Geoscience and Remote Sensing, 44(6): 1566-1574.

Matthew, M.W. et al., 2003. Atmospheric correction of spectral imagery: evaluation of the FLAASH algorithm with AVIRIS data, Algorithms and Technologies for Multispectral, Hyperspectral, and Ultraspectral Imagery IX. SPIE, Orlando, FL, USA, pp. 474-482.

Matthew, M.W. et al., 2000. Status of atmospheric correction using a MODTRAN4-based algorithm, Algorithms and Technologies for Multispectral, Hyperspectral, and Ultraspectral Imagery VI. SPIE, Orlando, FL, USA.

Pandey, R. and Vyas, B.M., 2004. Study of total column ozone, precipitable water content and aerosol optical depth at Udaipur, a tropical station. Currect Science, 86(2): 305-308.

Pandya, M.R. et al., 2002. Bandpass solar exoatmospheric irradiance and Rayleigh optical thickness of sensors on board Indian Remote Sensing Satellites-1B, -1C,-1D, and P4. IEEE Transactions on Geoscience and Remote Sensing, 40(3): 714 - 718.

Pantazis, M. et al., 1998. Trade Studies in Multi/hyperspectral Imaging Systems Final Report.

Parodi, G.N. and Prakash, A., 2004. Radiometric correction. In: N. Kerle, L.F.L. Janssen and G.C. Huurneman (Editors), Principles of remote sensing. ITC education text book series. The international institute for geo-information science and earth observation (ITC), Enschede, pp. 129-137.

Parvesh, D., 2006. Sampling scheme optimization from hyperspectral data. Doctorate Thesis, Wagenigen University, Enschade, 164 pp.

Pearlman, J.S. et al., 2003. Hyperion, a space-based imaging spectrometer. Ieee Transactions on Geoscience and Remote Sensing, 41(6): 1160-1173.

Qu, Z., Kindel, B.C. and Goetz, A.F.H., 2003. The High Accuracy Atmospheric Correction for Hyperspectral Data (HATCH) model. IEEE Transactions on Geoscience and Remote Sensing, 41(6): 1223-1231.

Ramsey, E. and Nelson, G., 2005. A whole image approach using field measurements for transforming EO1 Hyperion hyperspectral data into canopy reflectance spectra. International Journal of Remote Sensing, 26(8): 1589-1610.

Richter, R., 1997. Correction of atmospheric and topographic effects for high spatial resolution satellite imagery. International Journal of Remote Sensing, 18(5): 1099-1111.

Robila, S.A. and Gershman, A., 2005. Spectral matching accuracy in processing hyperspectral data. IEEE Transactions on Geoscience and Remote Sensing, 1(1): 163- 166

Rochford, P.A. et al., 2005. Validation and refinement of hyperspectral/multispectral atmospheric compensation using shadowband radiometers. IEEE Transactions on Geoscience and Remote Sensing, 43(12): 2898- 2907.

Roy, S.-S., Malhotra, G. and Mohanty, M., 1998. Geology of Rajasthan. Geological Society of India, Balgalore, 278 pp.

Smith, G.M. and Curran, J.P., 1998. Methods for estimating image signal-to-noise ratio (SNR). In: P.M. Atkinson and N.J. Tate (Editors), Advances in remote sensing and GIS. John Wiley and sons, Chichester, New York, Weinheim, Brisban, singapore, Toranto, pp. 61-73.

Staenz, K., Secker, J., Gao, B.C., Davis, C. and Nadeau, C., 2002. Radiative transfer codes applied to hyperspectral data for the retrieval of surface reflectance. ISPRS Journal of Photogrammetry and Remote Sensing, 57(3): 194-203.

Tanre, D. et al., 1990. Description of a Computer Code to Simulate the Satellite Signal in the Solar Spectrum - the 5S Code. International Journal of Remote Sensing, 11(4): 659-668.

Van der Meer, F., 2004. Analysis of spectral absorption features in hyperspectral imagery. International Journal of Applied Earth Observation and Geoinformation, 5(1): 55-68.

Van der Meer, F., 2006. The effectiveness of spectral similarity measures for the analysis of hyperspectral imagery. International Journal of Applied Earth Observation and Geoinformation, 8(3): 3-17.

Van der Meer, F. and De Jong, S., 2003. Imaging Spectrometery. Basic Principles and Prospective Applications, 4. Kluwer Achademic Publishers, Dordrecht/ Boston/ London, 35 pp.